

DISSERTATION ZUR ERLANGUNG DES DOKTORGRADES DER FAKULTÄT
FÜR CHEMIE UND PHARMAZIE DER
LUDWIG-MAXIMILIANS-UNIVERSITÄT MÜNCHEN

3D Orbital Tracking Microscopy: From Cells To Organisms

Fabian Wehnekamp

AUS DETMOLD, DEUTSCHLAND

2016

Erklärung

Diese Dissertation wurde im Sinne von § 7 der Promotionsordnung vom 28. November 2011 von Herrn Prof. Don C. Lamb, PhD betreut.

Eidesstattliche Versicherung

Diese Dissertation wurde eigenständig und ohne unerlaubte Hilfe erarbeitet.

München, den 02.11.2016

Fabian Wehnekamp

Dissertation eingereicht am: 03.11.2016

1. Gutachter: Prof. Don C. Lamb, Phd

2. Gutachter: Prof. Dr. Thomas Misgeld

Mündliche Prüfung am: 02.12.2016

Die Rechte, bereits veröffentlichte Texte oder Darstellungen zu verwenden, wurden via *Rightslink* erworben.



Once you know how to do it, it's pretty straightforward!
- Unknown technical support engineer...

Abstract

Single-particle tracking methods are able to localize individual particles with milli- or even microsecond temporal and nanometer spatial resolution. The knowledge about the spatiotemporal position of a particle offers the ability to monitor particle transport and to investigate parameters such as velocity, direction and processivity. In addition, the interaction of the tracked particle with the environment allows the construction of models, which can explain the underlying transport mechanisms.

In this work, I will first describe the hard- and software design for the combination of a feedback based single-particle tracking method, called 3D orbital tracking and a wide-field microscope. 3D orbital tracking performs particle localization by rotating the laser focus along a circular path around the particle of interest. The recorded fluorescent intensity signal during one full rotation of the focus allows to calculate the particle position relative to the center of the orbit. After each rotation, the orbit center is repositioned and thus, the laser focus is able to follow a single particle throughout the specimen. The additional wide-field microscope allows the simultaneous recording of environmental information. This allows one to put the acquired three dimensional tracking data into the context of cellular structures and other cargos.

Due to the high acquisition rates of up to 200 Hz, the 3D orbital tracking method produces long high-resolution trajectories, which are analyzed using a novel correlation based method. The method is able to discriminate three dimensional trajectory data into phases of active transport and phases of passive motion.

The first application in this thesis is the investigation of lysosomal transport at microtubule intersections inside BSC-1 monkey kidney cells. Apart from the ability to localize lysosomes inside the cell, the orbital tracking method can be used to resolve the cytoskeleton structure with nanometer precision and millisecond temporal resolution, which is not possible using

other super-resolution microscopy approaches like stochastic optical reconstruction microscopy (STORM) or stimulated emission depletion microscopy (STED). With the recorded structure, we can investigate the stability of individual microtubule strands by comparing the measured fluctuations with the count-rate dependent localization precision.

The second application I will present in this thesis is the first feedback based single-particle tracking experiment performed under *in vivo* conditions. Until now, technical limits have constraint these methods to single cells or tumor spheroids. The modifications presented in this thesis allow us to perform tracking experiments inside live zebrafish embryos with nanometer precision over distances of more than 100 μm . In detail, the orbital tracking approach is used to investigate the transport of mitochondria inside the stem axon of rohon-beard sensory neurons. A malfunction in this highly regulated process has been linked to several neurodegenerative diseases such as dementia or amyotrophic lateral sclerosis (ALS) and is thus of particular interest. The exceptional spatiotemporal resolution of the presented microscope enabled us to detect two previously unknown types of motion and to reveal their interactions with already known components of mitochondrial transport. In addition, the simultaneous recorded wide-field images enabled us to investigate the behavior of moving mitochondria in the presence of other stationary mitochondria.

The last project I performed during this PhD is a hard- and software upgrade of a commercial spinning disk confocal microscope. The addition of a new electron multiplying charge coupled-device (EMCCD) camera and four additional laser wavelengths (totaling 3 cameras and 8 laser lines) required the design of a new software, capable of operating all microscopy parts with a synchronization on the millisecond timescale. In addition to several imaging options, a perfect focus system was implemented into the microscopy software, which allows drift-free recordings of z-stacks over the course of several hours.

Contents

1	Introduction	1
2	Fluorescence Microscopy	5
2.1	Fluorescence	5
2.1.1	Einstein Coefficients	5
2.1.2	Jablonski Diagram	6
2.1.3	Absorption & Emission	7
2.1.4	Fluorescent Proteins	9
2.2	Confocal Microscopy	11
2.2.1	Optical Resolution Limit	12
2.2.2	Confocal Microscope	13
2.2.3	Resolution & Pinhole	15
3	Single-particle Tracking	17
3.1	Particle Tracking Methods	19
3.1.1	Post Measurement Techniques	19
3.1.2	Feedback Techniques	21
4	3D Orbital Tracking Microscopy	27

4.1	Orbital Tracking Theory	29
4.1.1	Lateral Localization	29
4.1.2	Axial Localization	33
4.2	Microscope Setup	34
4.2.1	Laser Excitation	34
4.2.2	Confocal Microscope	34
4.2.3	Wide-field Microscope	36
4.2.4	Microscope Body	36
4.3	Tracking Program	37
4.3.1	Program Functions	39
4.3.2	Code Structure	41
4.3.3	Confocal State Machine	46
4.3.4	Camera State Machine	62
4.3.5	Image State Machine	66
4.3.6	Calibration State Machine	68
4.4	Microscope Performance	69
4.4.1	Acquisition Speed	69
4.4.2	Particle Tracking Performance	69
4.5	Microscope Alignment	74
5	Correlation Analysis	79
5.1	Introduction	79
5.2	2-dimensional Correlation Analysis	82
5.3	3-dimensional Correlation Analysis	87

5.4	Correlation Parameter Determination For Mitochondrial Trafficking	89
5.5	Discussion & Outlook	91
6	Lysosome Trafficking In Monkey Kidney Cells (BSC-1)	93
6.1	Introduction	93
6.2	Microtubule Tracking	97
6.3	Lysosome Tracking	99
6.4	Discussion & Outlook	103
7	Studying Mitochondrial Dynamics In Vertebrate Axons In Vivo	107
7.1	Introduction	107
7.2	Results	109
7.2.1	3D Orbital Tracking Microscopy In Live Zebrafish Embryos	109
7.2.2	Characterization of Mitochondrial Motion	120
7.2.3	Pausing behavior of individual mitochondria	126
7.3	Discussion & Outlook	130
8	Spinning Disk Confocal Microscope Upgrade	133
8.1	Spinning Disk Principle	133
8.2	Spinning Disk Upgrade Requirements	135
8.3	Spinning Disk Confocal Microscope	136
8.4	Hardware Connections	139
8.5	Custom Spinning Disk Software	142

8.5.1	Andor Laser Combiner 401	144
8.5.2	Nikon Perfect Focus System	147
8.5.3	Camera, Laser & Z-piezo State Machine	153
8.6	Component List	158
9	Conclusion & Summary	161
10	Materials and methods	165
10.1	3D Orbital Tracking Microscope	165
10.1.1	Microscope Body	166
10.1.2	Widefield Path	167
10.1.3	Confocal Path	168
10.1.4	Laser Box	169
10.1.5	Electronics	170
10.2	Zebrafish Experiments	171
10.3	Tracking in BSC-1 Cells	174
	Bibliography	175
	Acknowledgments	191

List of Figures

2.1	Jablonski Diagram	6
2.2	Absorption and emission spectrum	7
2.3	GFP: spectra and structure	9
2.4	Schematic of a confocal microscope	13
2.5	Confocal scanning	14
3.1	Tracking microscope after <i>Berg et. al.</i>	18
3.2	Overview of post measurement tracking techniques	23
3.3	Feedback techniques using multiple detection volumes	24
4.1	Orbital tracking principle	27
4.2	Lateral tracking principle	30
4.3	Axial tracking principle	33
4.4	3D Orbital Tracking microscope schematic	35
4.5	User interface of the tracking software	37
4.6	Code structure of the orbital tracking software	41
4.7	Confocal state machine structure	46
4.8	Mapping procedure	50
4.9	Execution scheme of the tracking algorithm	56
4.10	Program flow of the localization algorithm	57
4.11	Camera state machine structure	62
4.12	Dual color image of a BSC-1 cell stably expressing GFP-Tubulin and Lamp2-mCherry	66
4.13	3D Orbital Tracking localization precision	70
4.14	Count rate dependent lateral localization precision	71
4.15	Count rate dependent axial localization precision	72
4.16	Localization precision depends on particle speed	73
4.17	3D Orbital Tracking microscope schematic	74
4.18	Auto- and crosscorrelation curves used for alignment	75
4.19	Detector pair alignment	76

5.1	Mean squared displacements of different motion types	80
5.2	Correlation amplitudes of active transport and diffusion	83
5.3	Simulated recovery rates for the 2D correlation analysis.	85
5.4	Simulated recovery rates for the 3D correlation analysis.	88
5.5	Parameter determination for the analysis of mitochondrial transport	89
6.1	Dual color confocal image of a BSC-1 cell	94
6.2	Microtubule tracking	98
6.3	Lysosome tracking	99
6.4	Mode I & II motion	100
6.5	Cargo behavior at microtubule intersections	101
6.6	Preliminary dual-color tracking results	104
7.1	Experimental Setup	109
7.2	Tracking mitochondrial motion in the context of the axonal structure	110
7.3	Transport of multiple mitochondria inside the stem axon	111
7.4	Antero- and retrograde trajectories of mitochondrial motion inside the stem axon	112
7.5	Classification of antero- and retrograde motion into two individual motion states	113
7.6	Mitochondrial motion is driven by five individual motion types	114
7.7	Influence of mitochondrial shape on localization precision	116
7.8	Zebrafish heartbeat	117
7.9	Nocodazole treatment affects mitochondrial transport	120
7.10	Transition probabilities and pause durations	123
7.11	Repetitive tracking of mitochondria over the same stretch of an axon	126
7.12	Analysis of environmental data	127
7.13	Influence of stationary mitochondria	128
8.1	Comparison between confocal and spinning disk confocal microscopy	134
8.2	Schematic of the spinning disk confocal microscope	138
8.3	User interface of the Spinning Disk software.	142
8.4	Software Structure of the Spinning Disk program	143
8.5	Perfect focus system state machine	150
8.6	State machines operating motion along the optical axis, camera and laser triggering	154
8.7	Camera acquisition modes	155

8.8 Hardware synchronization 156

10.1 3D Orbital Tracking microscope schematic 165

List of Tables

4.1	Fourier coefficient characteristics	31
4.2	Confocal State Machine Variable Cluster	42
4.3	Camera State Machine Variable Cluster	44
4.4	Camera State Machine Variable Cluster	45
4.5	Available tracking modes	53
4.6	Update Logic for different tracking settings	58
4.7	Output parameters of the tracking routine	59
4.8	Data structure of the output files	60
4.9	Camera properties	63
4.10	Acquisition settings subroutines	64
7.1	Data validation	118
7.2	Numerical values of motion parameters	119
7.3	Numerical values of motion parameters from nocodazole treated embryos	124
7.4	Numerical values of motion parameters from nocodazole treated embryos	125
8.1	Example fluorophores for spinning disk laser lines	136
8.2	Connection scheme and output values for each embedded module.	140
8.3	Pin connection of the 37 pin D-SUB connector attached to the Andor precision control unit.	141
8.4	Laser types, wavelengths and respective COM Ports inside the ALC 401	145
8.5	Start Up ASCII sequence for the Coherent Cube laser	145
8.6	Start Up ASCII sequence for the Coherent Sapphire laser	146
8.7	Start Up ASCII sequence for the Cobolt Jive laser	146
8.8	List of Property Node PFS commands	147
8.9	List of Invoke Node PFS commands	148
8.10	Communication variables between FPGA and Host Computer	153

8.11	Microscope body and detection path components	158
8.12	Laser Box Components	158
8.13	Andor Laser Combiner 401	159
8.14	Hardware Control Components	159
10.1	Microscope Body Components	166
10.2	Wide-field Microscope Components	167
10.3	Confocal Microscope Components	168
10.4	Laser Box Components	169
10.5	Electrical Components	170

Chapter 1

Introduction

In 1665, Robert Hooke published a set of drawings he created using a self developed optical microscope [1]. The book included drawings of fungi, the eyes of a fly, spider and mite and a piece of cork. Hooke observed regular cavities in the cork structure and referred to them as "cells" and coined this term for the smallest self-sustaining building blocks in all living organisms. The combination of physics and biology allowed Hooke to gain unprecedented insight into the microscopic world and he named his work *Micrographia*.

Although Hooke was an exceptional scientist, the optical resolution of his microscopes was not sufficient to resolve small structures on the sub cellular level. It took more than 200 years until Carl Zeiss and Ernst Abbe were able to build microscopes with a resolution that was limited by the diffraction limit of light and not by the quality of the lenses [2]. The next significant step was made by an associate of Carl Zeiss, August Köhler. In 1904 he presented the first fluorescence microscope, which used the fluorescent emission of the sample to create an image. Further improvements of optical microscopes were made in the last several decades with the invention of coherent light sources, the laser and improvements in detectors and cameras, which are able to detect individual photons (avalanche photo diodes, photo-multiplying tubes, CCD and CMOS cameras). The technical advancements made it possible to gain mechanistic insight into biological processes inside cells.

One subset of fluorescent microscopy techniques is called single particle tracking and allows one to probe the spatiotemporal location of a fluorescently labeled particle in its natural environment. Since the location of the particle is known throughout every point in time, this method allows one to probe interactions between the particle of interest and it's environment or another subset of particles. One particular technique, called *3D Orbital tracking*, is the main topic of this thesis. Orbital tracking allows one to track a single

particle with millisecond temporal and nanometer spatial resolution. As the name indicates, the laser focus of a confocal microscope is moved on a circular orbit around the particle of interest [3]. The particle location, in relation to the center of this orbit, is then derived from the recorded fluorescent data and the center of the orbit is moved to the new particle location. In addition, a second wide-field microscope is attached to the system and provides data about the surroundings of the particle.

In this thesis, the orbital tracking microscope is further improved by a self-written tracking software, which provides real-time capabilities, synchronization of all microscopy parts and simultaneous camera operation. The software is designed to run on a combination of a host computer and a deterministic processing unit (real-time CPU + Field programmable gate array, FPGA). A detailed description of this microscope and the technical advancements can be found in chapter 4.

The trajectory data acquired with the orbital tracking approach has to be analyzed to extract the required information. A novel analysis approach to classify motion into active and passive phases was developed and is presented in chapter 5.

Transport of vesicles in cells is a highly regulated but poorly understood process. Together with a combination of an astigmatism based tracking approach and stochastic optical reconstruction microscopy (STORM), the 3D Orbital tracking was used to study the transport of lysosomes along the cytoskeleton of the monkey kidney cell line BSC-1. In addition to lysosomal transport, the three dimensional structure of the microtubule network was probed on the nanometer scale to determine the amplitude of fluctuations along the cytoskeleton network. The results of this project are presented in chapter 6.

The orbital tracking approach was then applied to follow the motion of individual mitochondria in an *in vivo* model system, zebrafish embryos. The motion of mitochondria in the stem axon of rohon-beard sensory neurons is a highly complex process and not very well understood. The spatiotemporal resolution of the orbital tracking technique allowed us to study the complex motion pattern and revealed the presence of previously unknown motional states. Together with the wide-field environmental data, interactions between moving and stationary mitochondria could be observed. The results of this project are presented in chapter 7.

During the construction of the 3D Orbital tracking microscope it became apparent that FPGAs offer several advantages to operate microscope system and was used in the hard- and software upgrade of a commercial spinning disk microscope. The system was expanded by four additional laser lines and a third EMCCD camera system. The software previously used to operate the microscope was not able to operate the additional hardware and a self-written software was designed as a replacement. The new software allows to operate eight different laser lines together with three EMCCD cameras and is capable of controlling the perfect focus system present in the microscope body, which allows drift-free recordings of z-stacks over prolonged periods. The hard- and software design is described in chapter 8.

Chapter 2

Fluorescence Microscopy

2.1 Fluorescence

Fluorescence describes the interaction of light with matter in the for a human eye visible wavelength range of 400 to 700 nm. The term fluorescence was coined by Sir George Gabriel Stokes in 1852. He excited fluorite with ultraviolet radiation and observed the emission of visible light. The energy shift between the absorbed and emitted light is called Stokes shift and is discussed in the following sections.

2.1.1 Einstein Coefficients

In 1916, Albert Einstein described three possible types of interaction of electromagnetic waves with matter [4]. First, the absorption of a single photon from an electromagnetic field, which results in an excited state of the dye molecule or atom. Second, the spontaneous emission of a photon by a molecule or atom from an excited state. And last, the stimulated emission of a photon, which is triggered by an incoming second photon. The stimulated photon possesses the same frequency, direction and phase as the incoming photon. The behavior of a subset of molecules or atoms can then be described by the following differential equation:

$$\frac{dN_0}{dt} = -\frac{dN_1}{dt} = -N_0 \cdot B_{01} \cdot \rho(v) + N_1 \cdot B_{10} \cdot \rho(v) + N_{10} \cdot A_{10} \quad (2.1)$$

where N_0 and N_1 denote the number of molecules in the ground and first excited state of the molecule, B_{10} , B_{01} and A_{10} are the Einstein coefficients and $\rho(v)$ the spectral density. Equation 2.1 therefore describes the behavior of

a two level system upon irradiation with light. If no electromagnetic radiation is absorbed by the system ($\rho(v) = 0$), the system relaxes to the ground state N_0 through spontaneous emission ($N_{10} \cdot A_{10}$). Upon illumination, the system will end up in an equilibrium state given by the rates of stimulated emission ($N_1 \cdot B_{10} \cdot u$), absorption ($-N_0 \cdot B_{01} \cdot u$) and spontaneous emission. The simple model derived by Einstein was further improved by Jablonski in 1931 and offered a more complete approach to describe the interaction of light with molecules. While absorption and emission processes are commonly used in microscopy, stimulated emission is the main driving force for coherent light sources such as masers [5] and lasers [6].

2.1.2 Jablonski Diagram

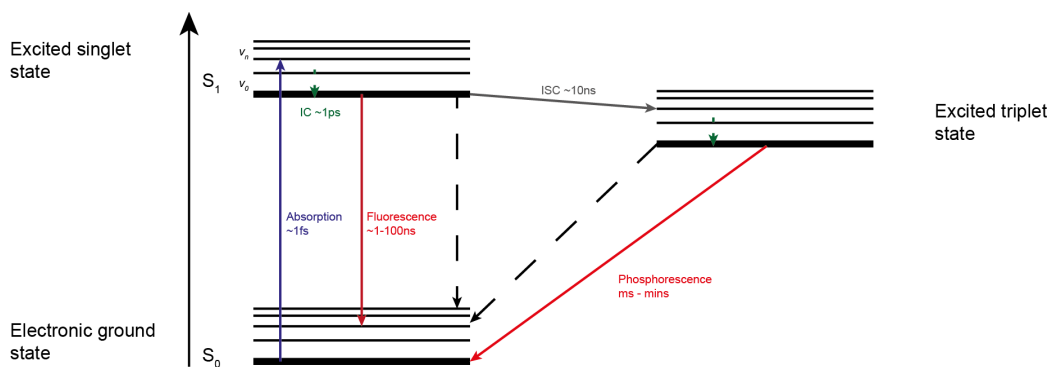


Figure 2.1 | Jablonski Diagram: Molecular energy pathways between the ground and excited state for absorption (blue), internal conversion (green) and fluorescence (red). Inter system crossing between the excited singlet and triplet states causes a phenomenon called phosphorescence, a spin forbidden transition between a triplet and a singlet state. Non-radiative pathways are indicated by dashed lines.

In 1931 Erwin Jablonski developed the Jablonski diagram, which describes the different internal energy pathways involved in fluorescence and phosphorescence [7]. A molecule in the electric ground state S_0 is excited to the first excited state by absorption of a photon, a process occurring on the femtosecond timescale. The nuclear motion of the molecule is negligible for this short time period (Born-Oppenheimer approximation [8]) and requires that the new excited state (S_1) has to match the nuclear positions of the originating vibrational state (v_0). This requirement is directly connected to the shape of the excitation and emission spectra as given by the Franck Codon factors, which will be treated in the next section. After the excitation pro-

cess, which usually ends in a higher vibrational state, the system undergoes a vibrational relaxation through intermolecular collisions with the solvent or other dye molecules in the vicinity [9]. If the molecule spontaneously emits a photon through fluorescence, the system depletes to the ground state and is ready for a new excitation cycle. The process of spontaneous emission is in direct competition to other processes such as inter system crossing. This normally forbidden process can occur in the presence of heavy atoms facilitating spin-orbit coupling, which allows the singlet-triplet transition. The resulting triplet state can be depleted to the ground state of the molecule through a spin-forbidden process called phosphorescence. Due to the kinetic hindrance of this process, the decay rates can stretch up to several minutes.

2.1.3 Absorption & Emission

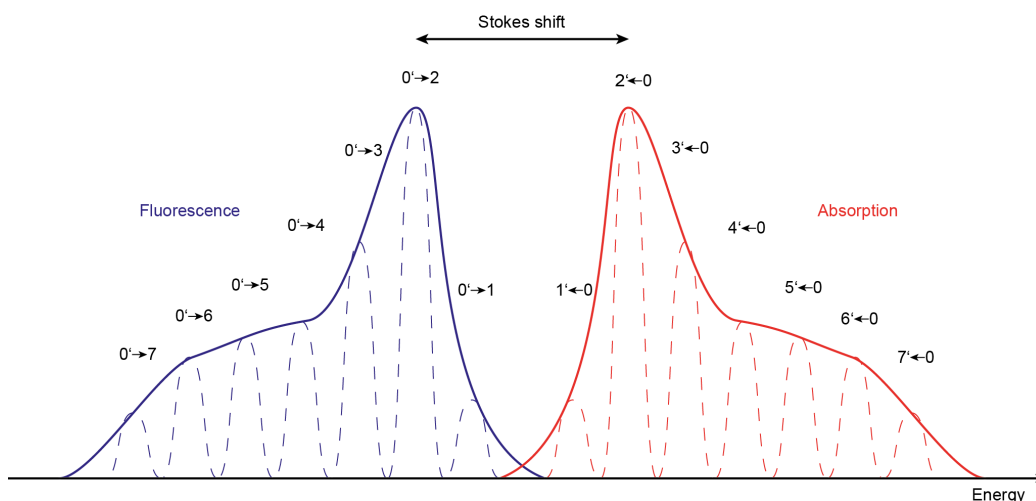


Figure 2.2 | Absorption and emission spectrum: Schematic absorption and emission spectrum of a single dye molecule. Transitions between vibrational states between the ground (n') and first electronic excited state (n) are indicated by the center of the Gauss curves (dashed lines). The width of each Gaussian represents homogeneous line broadening effects.

As already mentioned in the previous section, each fluorophore has a distinct excitation and emission spectra, which can be derived by the Franck-Condon principle. The probability for each electronic transition in a molecule can be described using the following equation:

$$P = \langle \Psi' | \mu | \Psi \rangle = \int \Psi' \mu \Psi d\tau \quad (2.2)$$

where $\mu = \mu_e + \mu_N$ is the dipole operator and Ψ is the product of the electronic, vibrational and spin wave functions $\Psi = \Psi_e \Psi_v \Psi_s$. Equation 2.2 can now be written as:

$$P = \int \Psi_e'^* \mu_e \Psi_e d\tau_e \int \Psi_v'^* \Psi_v d\tau_N \int \Psi_s'^* \Psi_s d\tau_s + \int \Psi_e'^* \Psi_e d\tau_e \int \Psi_v'^* \mu_N \Psi_v d\tau_N \int \Psi_s'^* \Psi_s d\tau_s \quad (2.3)$$

Due to the orthogonality of electronic wavefunctions, equation 2.3 can be reduced to:

$$P = \int \Psi_e'^* \mu_e \Psi_e d\tau_e \int \Psi_v'^* \Psi_v d\tau_N \int \Psi_s'^* \Psi_s d\tau_s \quad (2.4)$$

The probability P for a transition between electronic states is the product of the Franck-Condon factor (the overlap integral between two vibrational states, $\int \Psi_v'^* \Psi_v d\tau_N$) and the orbital ($\int \Psi_e'^* \mu_e \Psi_e d\tau_e$) and spin selection rules ($\int \Psi_s'^* \Psi_s d\tau_s$). During absorption or emission processes, neither the orbital nor the spin components of the wavefunctions change and thus the probability for an electronic transition between the ground and excited state is solely dependent on the Franck-Condon factors. The amplitude of each transition is proportional to the vibrational overlap integral and together with homogeneous line broadening effects (such as lifetime and thermal Doppler broadening), determines the shape of the excitation and emission spectra (Fig. 2.2). Since the Franck-Condon factors are valid for both emission and absorption, the respective spectra are mirrored and shifted by the energy loss caused during the internal conversion, called the Stokes Shift [10].

Fluorophores are usually excited using a narrow band light source such as lasers or LEDs or lamps in combination with excitation filters. Due to internal conversion, which happens on a much faster timescale (10^{-12} s) than the fluorescent decay to the ground state (10^{-9} s), the whole emission spectrum with lower energy than the excitation wavelength can be observed [9].

2.1.4 Fluorescent Proteins

For measurements in biological specimens, normal fluorophores possess several disadvantages. First, the insertion of dyes into living cells or even live animals is a complicated process. Dyes can be transferred using buffer solutions containing chemicals to facilitate the uptake (such as dimethyl sulfoxide, DMSO) or micro-injected using μm sized capillaries. These approaches can have an influence on the biochemical processes in the living cell or organisms, which can result in unknown experimental biases. Second, normal dyes show unspecific binding to various structures. To circumvent this unwanted behavior, the dyes have to be combined with target specific molecules such as antibodies. These constructs can easily be larger than the target molecule itself, which may alter or disrupt the natural function of the molecule of interest. Third, the dye itself can have a toxic effect on the cell or animal.

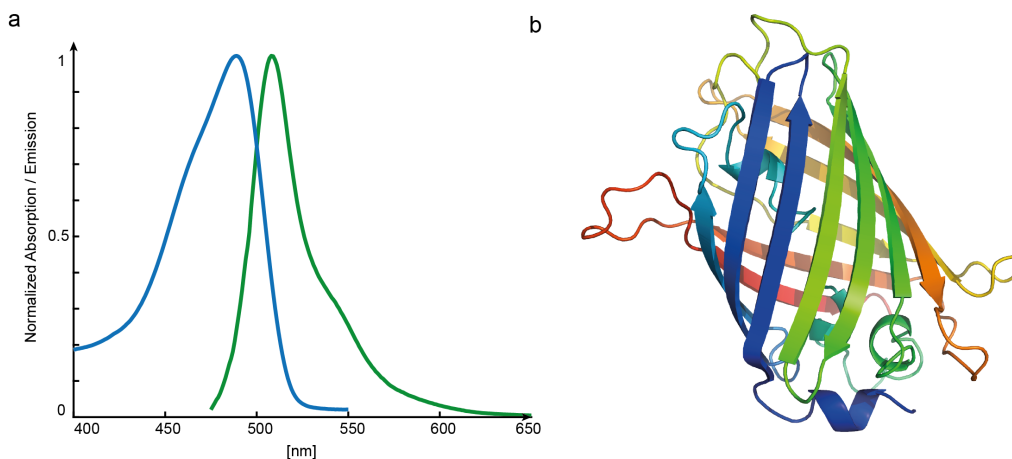


Figure 2.3 | GFP: spectra and structure: a) Excitation (blue) and emission (green) spectra from S65T GFP. b) The GFP protein structure consists of a beta barrel structure of 11 individual β -strands and an α -helix in the center containing the chromophore. From [11]. Reprinted with permission from AAAS.

Another method for labeling biological specimens is fluorescent proteins, which can be directly expressed inside the target specimen. In 1962, Osamu Shimomura extracted a fluorescent protein from the jellyfish *aequorea victoria*. The protein had excitation and emission maxima at 395 and 509nm respectively [12]. The nucleotide sequence of this wild-type green fluorescent protein (GFP) was cloned in 1992 [13] and led to the first expression in *E.coli* and *C.elegans*, which demonstrated the folding and fluorescence of this protein at room temperature without specific jellyfish cofactors [14].

Although the wild-type protein had several drawbacks such as poor quantum yield and poor photo-stability, its successful application lead to further research, which resulted in the first single-point mutated GFP derivate (S65T) developed by Roger Tsien in 1995 [15]. The single modification shifted the excitation maximum to 488nm while keeping the emission maximum at 509nm (Fig. 2.3 a)). The new spectral characteristics matched commercially available filter sets and lead to the application of fluorescent proteins in general research. Together with the crystal structures of wild-type [16] and S65T GFP (Fig. 2.3 b)) [17], it became possible to modify the protein through directed and random mutagenesis. Today, various fluorescent proteins are able to emit in the UV (Sirius [18]), Green (EGFP [19]), Yellow (Venus [20]), Red (TagRFP-T [21]) and infrared (mIFP [22]). Further modifications lead to photo-activalable (PAGFP [23]) and photo-switchable proteins (dendra2 [24]).

2.2 Confocal Microscopy

Conventional wide-field microscopy can be used to achieve good images from cells. When using modern optical components, even diffraction limited images can be obtained without great technical challenges. The quality of an image recorded using wide-field microscopy strongly depends on the contrast or, to be more specific, on the signal-to-noise ratio. In general, illumination in wide-field microscopy is performed using the so-called *Köhler* alignment [25], which in transparent samples excites the whole specimen and fluorescence from the whole sample will contribute to the image. Another factor decreasing the image quality is the Tyndall effect. If the specimen contains structures with the rough size of the excitation wavelength, light can be scattered and be redirected to the detector. These out of focus contributions blur the image and significantly decrease the contrast of the recorded image.

In 1961, Marvin Minsky developed a microscopy approach that only illuminated and detected a small section of the specimen [26]. This could be achieved by overlaying the excitation volumes, the detection volume and the detector. The alignment of all three elements in focus was used to name this new approach - confocal microscopy. The confocality was achieved by adding pinholes in the excitation and detection path, which remove out of focus contributions to the image. A detailed description of confocal theory is discussed in the following sections.

2.2.1 Optical Resolution Limit

In 1846, Ernst Abbe improved the work of George Biddell Airy [27] and described the diffraction of light, which, apart from the low quality optics at that time, is the main factor limiting the resolution of optical microscopes [2]. He derived that the diffraction of light depends on the angular aperture α of the incident beam multiplied with the refractive index n of the medium between specimen and lens, the so called numerical aperture NA :

$$NA = \sin \alpha \cdot n \quad (2.5)$$

Using the numerical aperture and the Rayleigh criterion [28], the smallest distance at which two emitters can be resolved is given as:

$$\Delta x = \frac{0.61 \cdot \lambda}{NA} \quad (2.6)$$

where λ denotes the excitation wavelength. Conventional microscope are not able to resolve two objects that are closer distanced than this limit. However, several approaches exist that are able to decrease the optical diffraction limit to less than a few nanometers. These include Stochastic Optical Reconstruction Microscopy (STORM) [29]. This technique uses the induced blinking of single emitters and a fitting routine to localize the maximum of the Gaussian point spread function with a precision of a few nm. The possible resolution enhancement depends on the number of recorded photons n :

$$\Delta x' = \frac{\Delta x}{\sqrt{N}} \quad (2.7)$$

Another approach, Super-Resolution Optical Fluctuation Imaging (SOFI), uses the temporal correlations of the fluorescent signal of blinking emitters and can achieve a resolution improvement, which depends on the order of auto- and cross cumulants used for calculation of the new image [30]. The last example is called Stimulated Emission Depletion (STED) microscopy, which uses a second laser to induce stimulated emission around the excitation spot at longer wavelengths than the detection window [31]. The resolution gain can be described with the following equation:

$$\Delta x' = \frac{\Delta x}{\sqrt{1 + I_{Max}/I_s}} \quad (2.8)$$

where I_s denotes the threshold intensity necessary to achieve depletion and I_{Max} the peak intensity of the depletion laser.

2.2.2 Confocal Microscope

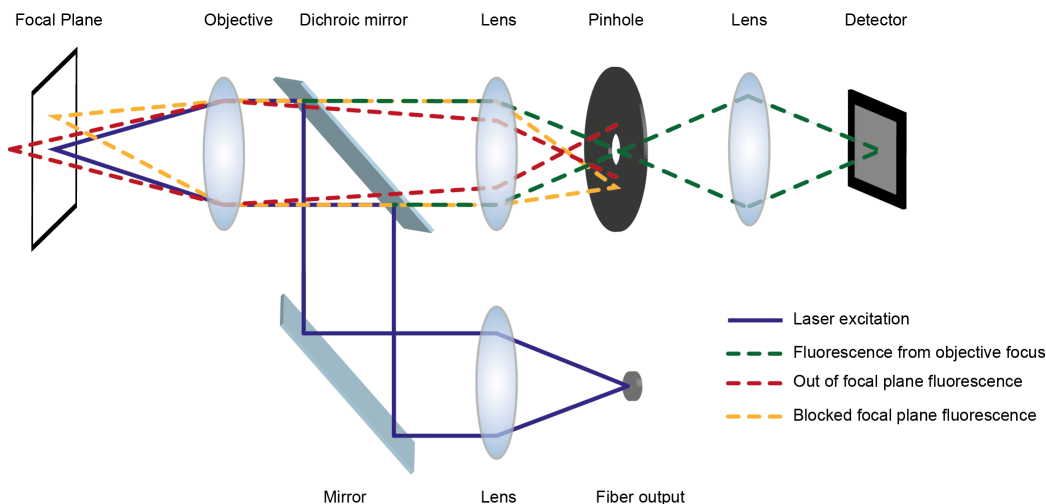


Figure 2.4 | Schematic of a confocal microscope: To achieve confocal conditions, the focal plane and the pinhole to be in focus of their respective lenses. The specimen is illuminated by a laser guided through a single-mode fiber, which acts as a confocal excitation pinhole (blue). Fluorescence from the objective focus can pass the pinhole (green), out of focus fluorescence (red and yellow) is blocked by the pinhole.

Figure 2.4 shows the schematic of a confocal microscope. Laser light for sample illumination is customarily guided through a single-mode fiber, which outputs a near Gaussian laser mode (TEM_{00}). The fiber output, which has a diameter of just a few μm acts as confocal pinhole and thus no additional pinhole is required for the excitation pathway. The excitation light is guided over a dichroic mirror, which acts as a longpass filter and only transmits the fluorescent signal. The specimen is placed into the focal plane of the objective and illuminated by a diffraction limited spot. The resulting fluorescence is collected by the objective and passes the dichroic mirror. Fluorescence from the focal spot of the objective is able to pass the pinhole, whereas out of focus light (from positions shifted axially or laterally away from the objective focus) is blocked by the pinhole. The fluorescence passes another lens and is registered by the detector (photomultiplier tube - PMT or avalanche photo diodes - APD). The basic design of a confocal microscope can only be used for point measurements, which can be used to measure intra- or intermolecular interactions using fluorescence correlation spectroscopy (FCS) [32, 33] or Förster resonance energy transfer (FRET) [34, 35]. Confocal images can

be created either by moving the specimen using a piezo stage on top of the microscope or through beam steering, which can be done through piezo or galvano mirrors [36] (Fig. 2.5). The piezo scanners have a response time on

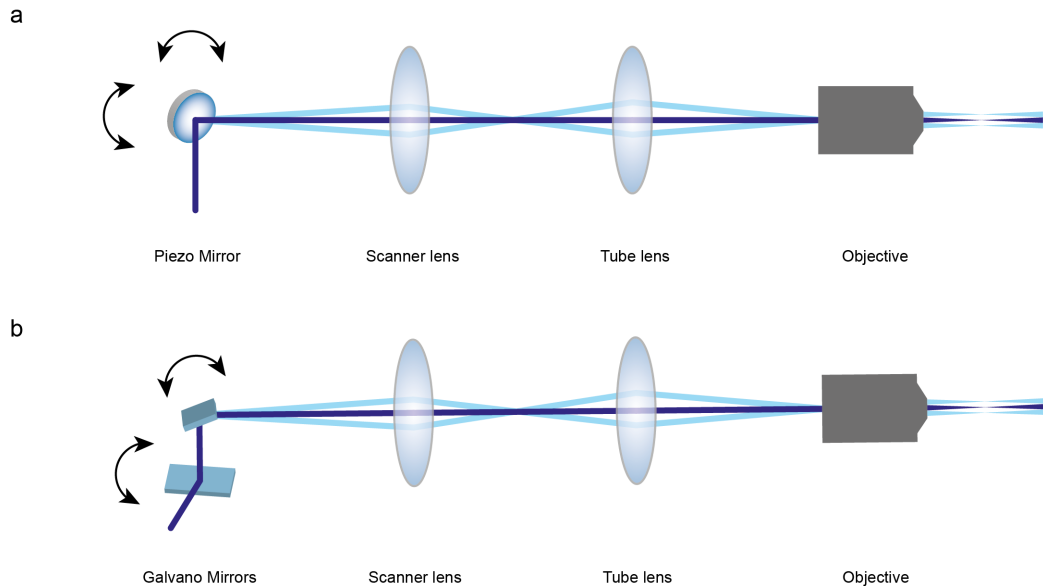


Figure 2.5 | Confocal scanning: Lateral beam steering can be performed using a piezo mirror (a) or a set of two galvano mirrors (b). The combination of a scanner and a tube lens ensures that only the angle of incidence at the back aperture of the objective changes while deflecting the beam along the x- and y-axis. The changing angle of incidence results in a lateral shift of the laser focus in the image plane of the objective.

the order of ~ 10 ms. Since piezo mirrors only utilize a single mirror for both axes, they can be placed into the focal position of the scanner lens causing no optical aberrations. Galvano mirror systems have response times of less than a millisecond, but consist of two independent axes and the focus position of the first lens has to be placed either on top of one mirror or in between the mirror pair. If necessary, a second telescope can be added between the mirror pair to minimize optical aberrations. Modern galvano scanner system can be operated in a resonant scanning mode, where two sine waves with frequencies up to several kHz are applied as input voltages. Depending on the image size, this operation mode can achieve pixel dwell times of a few μs [37].

2.2.3 Resolution & Pinhole

The insertion of a pinhole into the optical path of a microscope mainly improves the optical sectioning capabilities and has only a minor effect on the lateral resolution. The resolution enhancement in lateral and axial direction depends on the pinhole diameter, which is conventionally described in Airy units (AU) to account for the microscope specific optical elements. One Airy unit describes the distance between the first minima of the Airy disk pattern [27] multiplied by the total magnification of the microscope. For pinhole diameters larger than 1 Airy unit, the resolution for a confocal microscope in lateral and axial direction are given as:

$$\Delta xy = \frac{0.51\lambda}{NA} \quad (2.9)$$

and

$$\Delta z = \frac{0.88\lambda}{n - \sqrt{n^2 - NA^2}} \quad (2.10)$$

The resolution enhancement prefactors decreases with pinhole sizes smaller than 1 Airy unit and converges for diameters smaller than 0.25 AU to:

$$\Delta x = \frac{0.37\lambda}{NA} \quad (2.11)$$

and

$$\Delta z = \frac{0.64\lambda}{n - \sqrt{n^2 - NA^2}} \quad (2.12)$$

It has to be noted that the detection yield of a confocal microscope significantly decreases for pinhole diameters smaller than 1 AU. For the optimal balance between resolution enhancement and detection yield, the pinhole size should be adjusted to ~ 0.85 Airy units.

Chapter 3

Single-particle Tracking

Technical advances over the past decades have made it possible to detect single particles. This makes it possible to investigate subpopulations and to study interactions between individual particles, which would be otherwise hidden beneath other processes in bulk measurements. There are two possible sets of experiments for single particle detection. First, burst measurements can be performed where a particle is diffusing through the detection volume of a confocal microscope [38]. Single molecules can also be immobilized on the surface of a cover slip [39,40]. The first approach has the drawback, that the observation time is very short and possible dynamic changes might not happen during the transition through the focus. The second approach offers the option for prolonged imaging, but the modifications for surface attachment may alter the natural function of the particle. Both problems can be overcome by tracking the particles of interest in their natural environment and record their trajectories through the specimen. Knowledge about the particles spatiotemporal position at any given time point can be used to derive certain characteristics, such as the motion type, velocity, confinement and possible interactions with other components of the specimen and thus provides a detailed insight into cellular processes.

In 1971 the first single-particle tracking experiment was performed by Berg *et. al.*, who measured the motion of individual *E.coli* bacteria inside a small sample chamber [41] (Fig. 3.1 a). The motion of single bacteria was detected using 3 pairs of fibers (Fig. 3.1 b). The signal from each fiber was recorded by photomultiplier tubes and fed into an analogue feedback system, which repositioned the sample chamber to keep the bacteria in focus. In the following years, improved single-particle tracking (SPT) techniques allow more sophisticated experiments. These include studies about molecular motors [42], the

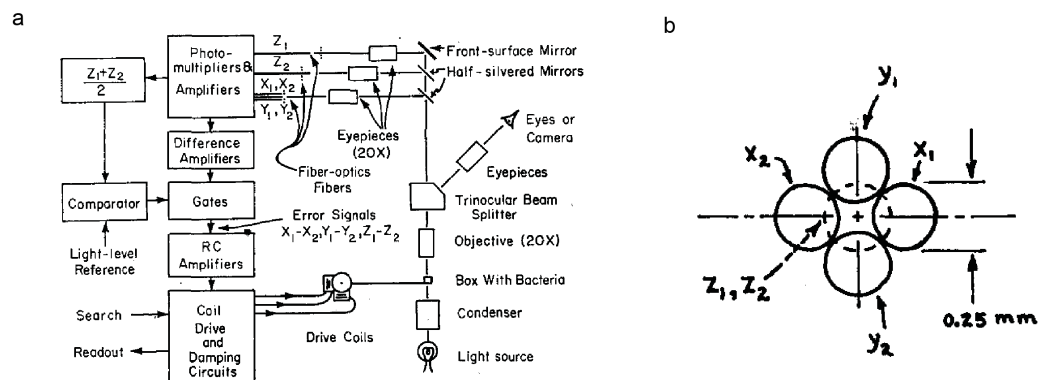


Figure 3.1 | Tracking microscope after *Berg et. al.*: a) Schematic of the microscope used to track bacteria inside a sample chamber. The signal was split between 3 pairs of optical fibers (b) and fed into an analogue feedback system that kept the tracked bacteria in focus. b) Alignment and dimensions of the six optical fibers. The motion along each dimension was determined through the intensity between a fiber pair. Reprinted from [41], with the permission of AIP Publishing.

motion of lipids [43,44] in bilayers or plasma membranes [45,46], the motion of gold nanoparticles [47] and virus entry processes in live cells [48] and even to track single GFP molecules in solution [49].

3.1 Particle Tracking Methods

Several two-dimensional (2D) and three-dimensional (3D) SPT techniques are available, which are specialized for specific experimental requirements. 2D tracking approaches are applicable to particles in specimens with a limited elongation ($\sim 1\mu m$) along the z -axis, for example membranes or flat cell lines like human HuH7 cells [50]. The more sophisticated 3D SPT techniques are required in specimens with z elongation exceeding $1\mu m$. Regardless of the dimensionality, all tracking techniques can be divided into feedback and post measurement techniques. Post measurement techniques extract the position of one or multiple particles after the experiment is over from the recorded data. Feedback approaches lock the objective focus onto a single particle by moving the sample or the laser focus in two or three dimensions inside the specimen with the help of a milli- or microsecond feedback loop. In this approach, the trajectory data is recorded while the experiment is running. In addition, feedback approaches allow the targeted manipulation of the particle of interest (e.g. manipulation through ultra-violet light). An overview of SPT methods is given in the following sections.

3.1.1 Post Measurement Techniques

In general, post measurement techniques analyze images recorded with EM-CCD or CMOS cameras. The most straightforward approach for lateral localization is fitting the point spread functions of all particles contained in the image (particle density has to be small to avoid the overlap of particles) individually with a simple Gaussian model. Given a high enough signal-to-noise ratio, the center of the Gaussian can be determined with an accuracy of a few nm. Without further modifications, only two dimensional motion inside the thin focal plane can be observed. Observation of three dimensional motion can be achieved through several methods such as astigmatism, point spread function shaping, off-focus imaging and z -stacks. The addition of a weak cylindrical lens into the imaging path leads to optical astigmatism and alters the shape of the recorded point spread function depending on the z position of the particle [51]. This method can locate particles within a $2\mu m$ thick slice along the z -axis with a precision of 12 nm (Fig. 3.2 a). Further modification of the point spread function using a spatial light modulator lead to the development of double-helix and more complex point spread functions, which allow tracking along the z -axis over distances of several μm [52, 53] (Fig. 3.2 b). Another possibility to localize particles along the z -axis is to determine the size of the diffraction pattern emerging from a particle outside of the microscope focus, called off-focus imaging [54]. This

technique allows the localization of particles over $4 \mu m$ along the z-axis and can be further improved through the simultaneous observation of two image planes separated by $1 \mu m$ [55] (Fig. 3.2 c). Finally, the recording of several images along the z-axis, called a z-stack, allows the localization of a particle along all three dimensions by a fitting approach using a three dimensional Gaussian model, but is highly restrictive in time resolution.

Camera-based post measurement techniques offer the advantage that, depending on the available field of view, several dozen particles can be tracked simultaneously without the loss of temporal or spatial resolution. However, since the available field of view is limited and stationary during the experiment, particles that leave the field of view in either dimension are permanently lost. Another drawback is the acquisition speed of the electron multiplying charged coupled device (EMCCD) cameras conventionally used for imaging, which limits the temporal resolution to a few dozen Hz or less in the case of z-stacks. However, the recent technical advancements in the photon detection efficiency in complementary metal-oxide-semiconductor (CMOS) cameras offer the possibility for frame rates beyond several dozen Hz.

A notable exception from fluorescent based SPT methods is a recently published method called interferometric scattering microscopy (iSCAT) [56]. Instead of exciting a dye molecule and recording the fluorescent signal, iSCAT uses the scattering of photons from the target molecules to determine their localization and a subsequent analysis of the interference between the molecule and the glass/water interface. This technique is capable to resolve individual steps of a myosin motor [57], but is not applicable in highly scattering specimens like cells.

3.1.2 Feedback Techniques

Feedback based SPT techniques offer the possibility of following a single particle through the whole specimen without the restriction of a preselected region of interest. Regardless of the technical implementation, the main principle of the feedback loop is always the same. The recorded fluorescence is used to determine the position of the particle in relation to the current laser focus and in each feedback iteration, the position of the laser focus is readjusted in two or three dimensions onto the current position of the particle. As long as the particle does not move faster than the reaction speed of the feedback loop, the length and precision of a trajectory is only limited by the number of detected photons, the photo-stability of the fluorophore and the available tracking area. In addition to the excellent spatiotemporal resolution of a few nanometer in all dimensions with millisecond temporal resolution, the constant lock-in of the laser focus on top of the particle allows a manipulation with additional laser lines. Although providing exceptional tracking performance, feedback methods generate less data (only a single particle vs. up to several dozens in post measurement techniques) and require a sophisticated technical implementation of the varying feedback algorithms on real-time computers, which provide accurate μs timing. In addition, only trajectory data is recorded and a second microscope or wavelength is needed to provide the environmental context. The huge advantage compared to post measurement approaches is the fact that the trajectory is generated during the experiment and no post-processing of the acquired data is necessary.

In 1998, *Peters et. al.* presented the first feedback based approach, which utilized an analogue feedback system providing nanometer accuracy with acquisition rates of 1 kHz [58]. Their approach used a combination of a position sensor responsible for lateral localization and a photo diode for axial detection. In the last two decades several other feedback methods have been presented and are briefly discussed in the following paragraphs.

Multiple detection volumes

To locate a particle in 3 dimensions, several points around the objective focus have to be probed. The fluorescent signal from each of these detection volumes is recorded and fed into the tracking feedback system. The most straightforward approach is a tetrahedral arrangement, where two pairs of detection volumes are oriented along the x and y axis. A minimal offset between the two detection pairs along the optical axis of the microscope provides the z position of the particle. The fluorescent intensity ratio between the detection volumes of each pair is proportional to the particle position along the corresponding axis. The detection volumes can be created in several ways. *Lessard et al.* used four slightly misaligned multi-mode fibers coupled to avalanche photodiodes, where each fiber entrance acted as confocal pinhole [59] (Fig. 3.3 a). The intensity data from all four channels were analyzed and the particle of interest was kept in focus by moving a three dimensional piezo stage. *Perillo et al.* further improved this approach using temporal multiplexing and two-photon excitation (TSUNAMI) [60]. The excitation pulses for each detection volume were shifted by 0, 3.3, 6.6 and 9.9ns through a combination of laser delay lines and slightly misaligned to create a tetrahedral geometry through the insertion of optical elements (Fig. 3.3 b). The fluorescent intensity was detected using a single detector in combination with time-correlated single-photon-counting (TCSPC) cards. By separating the arrival-time histogram into 4 equidistant bins, each incoming photon could be assigned to a detection volume and the four channels are processed using the same positioning algorithm introduced by *Lessard*. In addition to the lifetime information of the tracked particle, two photon excitation offers the possibility for deep tissue imaging.

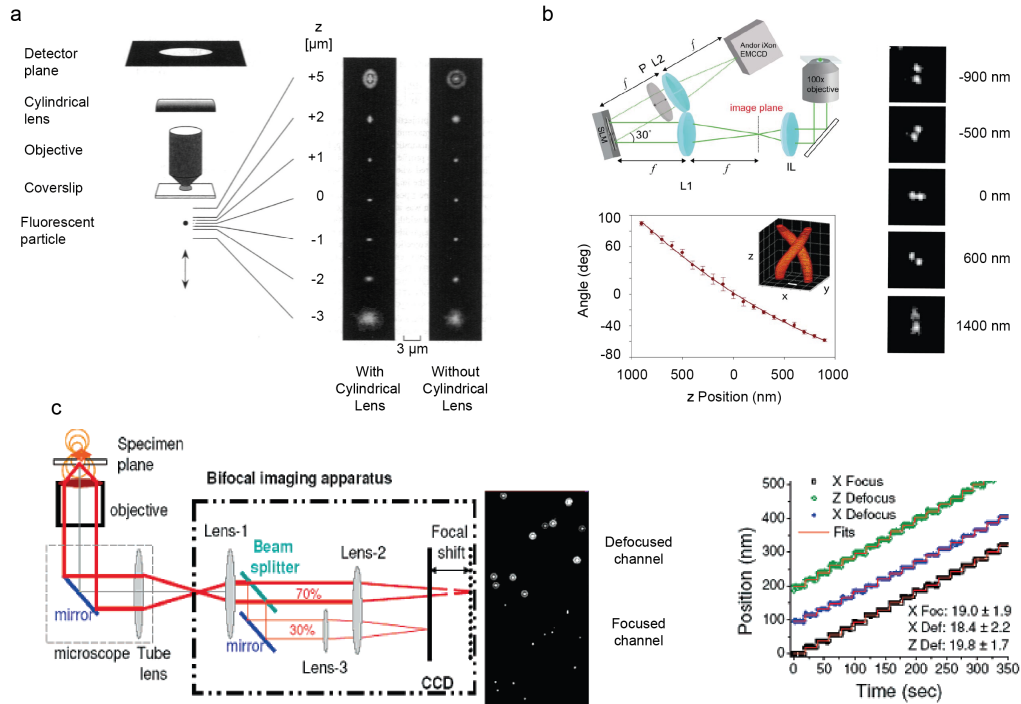


Figure 3.2 | Overview of post measurement tracking techniques: a) Astigmatism based SPT: The insertion of a cylindrical lens into the imaging pathway leads to an elliptical deformation of the point spread function, depending on the axial position of the fluorescent particle. b) SPT using a double helix point spread function: The addition of a spatial light modulator (SLM) into the Fourier plane of the imaging pathway and subsequent addition of a phase mask creates a double-helix point spread functions. Depending on the axial position of the particle, the two lobes show different orientations. c) Bifocal SPT: This approach uses the combination of a focused and a second slight defocused image. The lateral position can be calculated from the focused image and the axial position is extracted from the size of the diffraction pattern in the out of focus plane. Reprinted from [51] with permission from Elsevier, [52] copyright (2009) National Academy of Sciences and [55] copyright (2007) American Chemical Society.

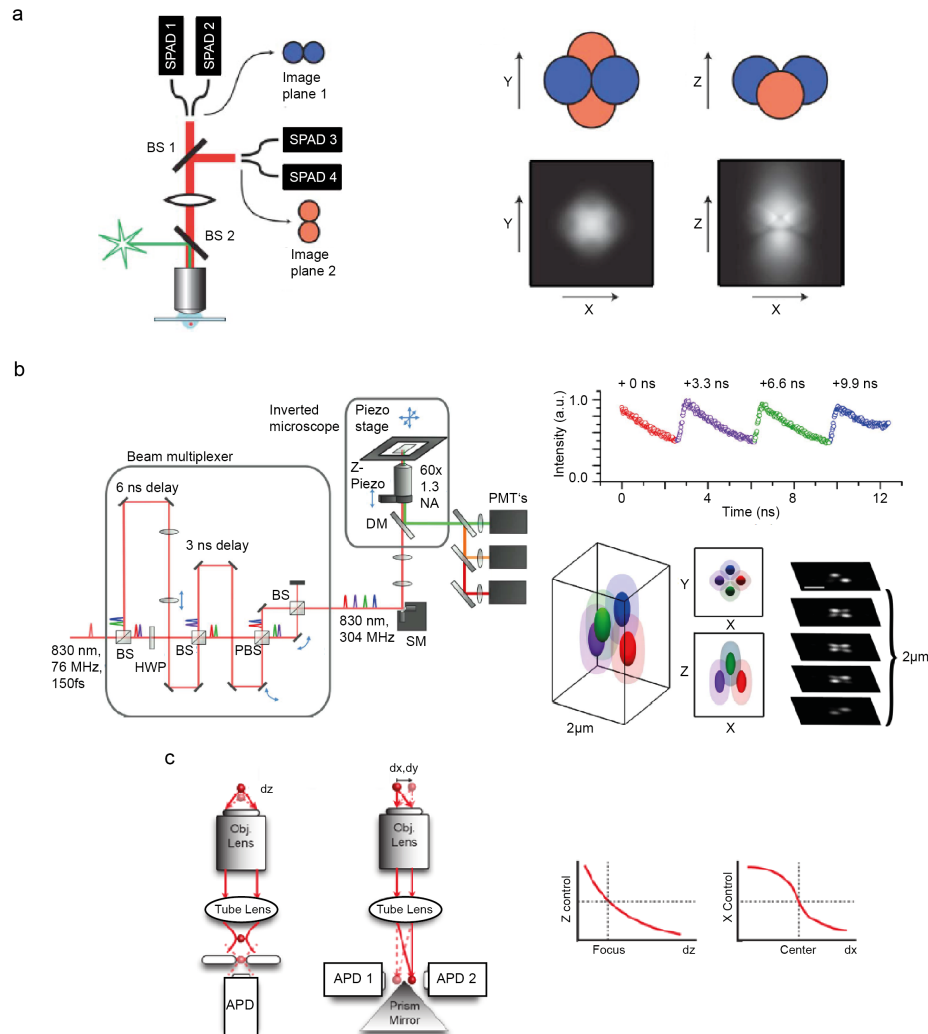


Figure 3.3 | Feedback techniques using multiple detection volumes:
 a) Tetrahedral detection: Implemented by *Lessard et. al.*. The detection volumes of 4 detectors are arranged in a tetrahedron. b) Tsunami design: Tetrahedral arrangement is created through spatiotemporal multiplexing. A femtosecond laser with a repetition rate of 76 MHz is passed through a nanosecond delay line, which outputs laser pulses with a frequency of 304 MHz. Each shifted laser pulse is aligned into one corner of a tetrahedron. BS: beam splitter, HWP: half-wave plate, PBS: polarizing beam splitter, SM: scanning mirror, PMT: photomultiplier tube, DC: dichroic mirror. c) Tracking approach presented by *Welsher et. al.*. Lateral localization is performed using two detector pairs for x and y detection. A fifth detector determines the particle localization along the z-axis. Reprinted from [59], with the permission of AIP Publishing, [60] and [61] Macmillan Publishers Ltd: Nature Nanotechnology, copyright (2014).

Another approach using a combination of four lateral detection volumes and an additional detector for axial localization was presented by *Welscher et. al.* (Fig. 3.3 c) [61]. In addition to excellent spatial and temporal localization precision, they included a two-photon scanning microscope for environmental observation. They were able to create three-dimensional confocal images parallel to the tracking process by synchronizing the axial position of the particle with the lateral position of the confocal scanner. Since the tracking algorithm is moving the image plane along the optical axis of the microscope while tracking a particle, only a mosaic image is reconstructed using this approach. Using a sophisticated image reconstruction algorithm, they filled in the missing voxels and were able to create a three dimensional projection of the particle environment.

Beam steering

Single particle tracking approaches using beam steering only use a single detection volume, which probes the fluorescent signal along a circular path around the tracked particle. The theory for particle localization using circular confocal scanning was proposed by Jörg Enderlein in 2000 [3] and was first applied by the group of Enrico Gratton [62]. Several options for lateral beam displacements are available. Piezo mirrors (Hz), galvano mirrors (kHz) (see Fig. 2.5) and acousto optical beam deflectors (AOBD, MHz). Piezo and galvano mirrors can be utilized in one- and two-photon microscopy, are able to deflect laser beams over wide optical angles and have a high positioning accuracy at very small angles in the μrad range. Faster beam steering can be achieved using acousto optical beam deflectors. These devices provide operating frequencies up to several hundred MHz. However two problems arise when using acousto optical beam deflectors. First, AOBDs operate in a very small wavelength range, thus only the laser excitation is deflected, confocal descanning cannot be performed. Therefore, only two-photon excitation, which does not require a confocal pinhole can be used for tracking approaches using AOBDs. Second, due to the small angle provided by AOBDs, an additional piezo stage on top of the microscope has to be added to relocate the sample. Axial particle localization is performed by probing two detection planes located slightly above and below the objective focus. These planes can be implemented using two detectors or through a sinusoidal oscillation along the optical path of the microscope, which is synchronized with the frequency of the rotating laser focus. [63, 64]. Focus displacement along the z-axis can be achieved by z-objective piezos or deformable lenses, which can change their focal length and are able to shift the laser focus along the optical axis [65].

Since only the laser beam is displaced, beam steering approaches offer higher acquisition speeds than multi-volume detection approaches, which use a sample stage to relocate the objective focus. In addition, due to the higher number of data points during the circular scan, more information about the tracked particle becomes available (e.g. surface information, shape and orientation) [66]. The circular shape of the orbit also allows to operate the galvano mirrors at their resonant frequencies (2-3 kHz) and gives the possibility to perform lateral localization with sub millisecond temporal resolution. Circular beam steering for particle localization is usually called "orbital tracking" and is the technical approach utilized in this thesis. A detailed discussion about orbital tracking theory and applications is given in the following chapters.

Chapter 4

3D Orbital Tracking Microscopy

The first step in the development of orbital tracking microscopy was done by Jörg Enderlein in 2000 when he proposed a theory to determine the location of a particle diffusing in a membrane by using a circular scan [3]. The varying intensity distribution during a full rotation encodes the particles location in relation to the center of the orbit:

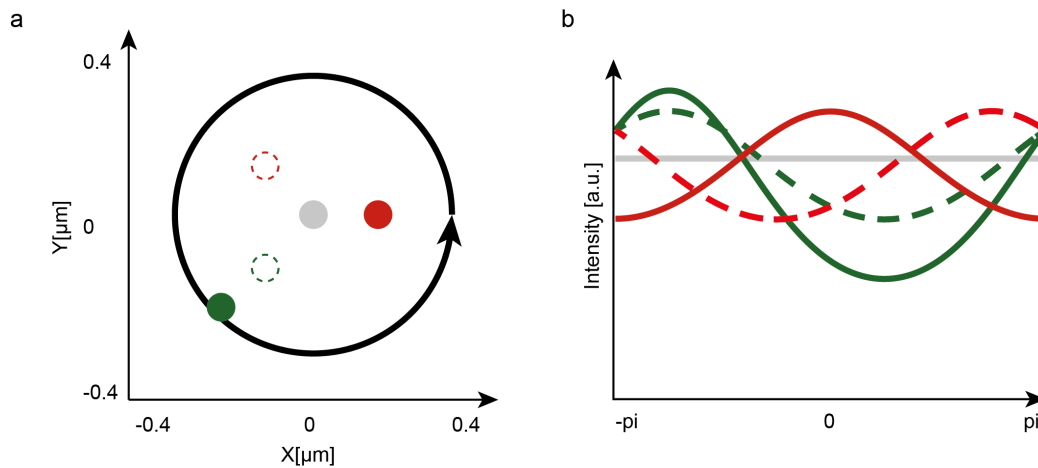


Figure 4.1 | Orbital tracking principle: a) Schematic of the center of the laser-scanning orbit (black) and 5 different particle locations (gray, red, dashed red, green and dashed green). b) Simulated orbit intensities for different orbit positions. The peak position of the intensity signal encodes the angular position with respect to the starting point of the orbit. The distance to the center is encoded in the modulation of the intensity orbit.

The first experimental proof of this lateral localization technique was shown by Kis-Petikova *et al.* in 2003 [62]. They achieved a count-rate dependent lateral localization precision of less than 10nm with a maximum acquisition speed of 500 Hz. In 2005, Levi *et al.* added the capability to follow a particle in the third dimension by oscillating the objective focus between two planes above and below the particle position [63]. A calibration curve of the intensity ratio between these two planes makes it possible to perform an axial localization of the particle. Although allowing the tracking of particles in all 3 dimensions, this oscillating approach had several disadvantages.

The objective motion is transferred into the sample and ultimately cause oscillations of the sample and will decrease the localization precision. Second, the delay time of the piezo crystals used to move the objective limits the acquisition speed. Fast piezo crystals have a response time of several milliseconds and together with the time for a minimum of two orbits (top and bottom position) decreases the tracking speed down to 15-30 Hz, depending on the signal-to-noise ratio.

To circumvent these problems, Katayama *et al.* used a different approach to axially localize the particle [64]. Instead of using temporary detection planes through sinusoidal oscillations, they added a second detector to the microscope, which allows the detection of photons at two different locations. By slightly misaligning the confocal pinholes of both detectors, it is possible to shift the confocal detection volumes slightly above and below the objective focus. This approach increases the acquisition speed due to the parallel detection of both planes.

4.1 Orbital Tracking Theory

The 3D orbital tracking method is a feedback based approach where the laser focus follows the particle of interest in a 3D specimen. The 3D positioning system is a combination of two algorithms, which perform a lateral and an axial localization of a particle of interest.

4.1.1 Lateral Localization

Fitting Based Localization

Consider a freely diffusing particle smaller than the diffraction limit and a displacement between localizations $v_{Instant}$, which is way smaller than the quotient of orbit radius r_{Orbit} and orbit time t_{Orbit} . In such a case, the position of the particle can be assumed as constant during a full rotation of the orbit and the fluorescent signal depends on the position of the particle in relation to the center of the orbit (Figure 4.2). The fluorescent signal for a single point can be approximated using a two dimensional Gaussian model:

$$I(x_1, y_1) = I_0 \cdot \exp\left[-\frac{2d^2}{\omega_0^2}\right] \quad (4.1)$$

where I_0 denotes the maximum fluorescent intensity, ω_0 the beam waist and d the distance between the Gaussian center and the particle. The equation can be expanded to describe all points along the circular rotation. Hence the center of the Gaussian beam moves is moved along a circle, it is convenient to change the coordinate system and use polar coordinates.

The distance between the beam center and particle

$$d(x_1, y_1) = \sqrt{(x_2 - x_1)^2 + (y_2 - y_1)^2} \quad (4.2)$$

can thus be described as:

$$d(\varphi_1) = \sqrt{r_1^2 + r_2^2 - 2 \cdot r_1 \cdot r_2 \cos(\varphi_1 - \varphi_2)} \quad (4.3)$$

where φ_1 includes the time information of the rotating focus given as $\varphi_1 = 2\pi ft$. Inserting Eq. 4.3 in Eq. 4.1 yields the theoretical background free fluorescent signal during the circular scan:

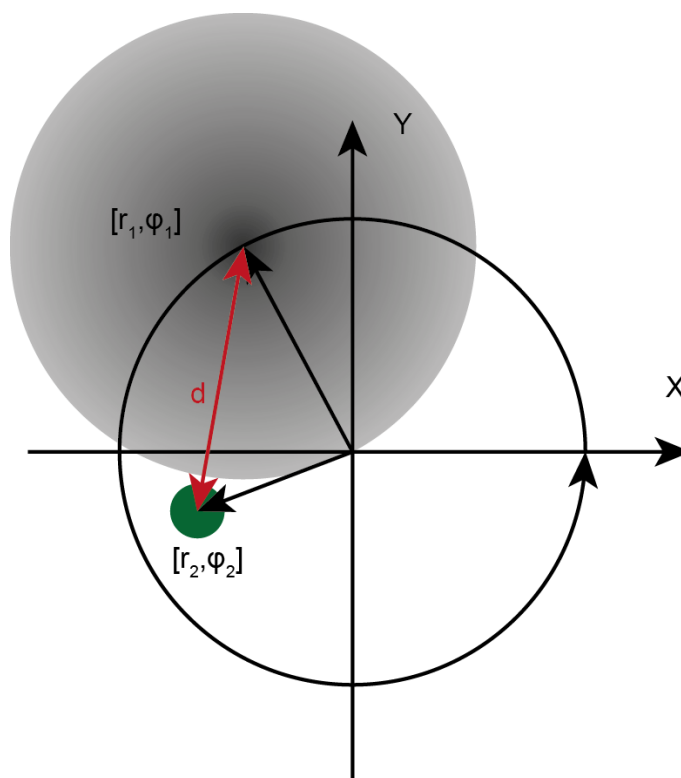


Figure 4.2 | Lateral tracking principle: The fluorescent signal at each point on the orbit depends on the position of the particle (green) in relation to the laser focus (gray) [62].

$$I(\varphi_1) = I_0 \cdot \exp \left[-\frac{2}{\omega_0^2} (r_1^2 + r_2^2 - 2 \cdot r_1 \cdot r_2 \cos(\varphi_1 - \varphi_2)) \right] \quad (4.4)$$

As the orbit radius r_1 and beam waist ω_0 are known, the position of the particle can then be extracted by fitting the recorded fluorescent signal with Eq. 4.4. This fitting process is ideal for post processing methods, e.g. distance measurements between two stationary particles [63]. However, due to the iterative routine, fitting is neither a fast nor a deterministic approach and thus not suitable to follow a particle with a feedback approach on the millisecond timescale.

Fourier Transformation Based Localization

One possible way to reduce the calculation time is to analyze the frequency spectrum of the fluorescent signal. The Fourier transformation can be used to convert every time-dependent signal $f(t)$ to the frequency domain $F(\omega)$:

$$F(\omega) = \frac{1}{\sqrt{2\pi}} \int_{-\infty}^{\infty} f(t)e^{-i\omega t} dt \quad (4.5)$$

Vice versa every periodic signal, for example the recorded fluorescent intensity during one orbit $I(\varphi_1, r_1)$, can be described by a Fourier series [67]:

$$I(\varphi_1, r_1) = \frac{a_0(r)}{2} + \sum_{k=1}^{\infty} (a_k(r) \cos(k\varphi) + b_k(r) \sin(k\varphi)) \quad (4.6)$$

where a_k and b_k denote Fourier coefficients. The transformation of a discrete intensity signal from the time domain to the frequency domain is a computationally inexpensive process when using the fast Fourier transformation algorithm [68]. Each pair of Fourier coefficients encode different properties of the particle of interest:

Coefficients	Amplitude	Phase
a_0	Average countrate of the intensity signal	-
a_1 & b_1	Distance to orbit center	Angular position of the particle
a_2 & b_2	Particle ellipticity	Particle rotation
a_3 & b_3	Particle triangularity	Particle rotation

Table 4.1 | Fourier coefficient characteristics: The lateral localization algorithm only uses the zero and first order Fourier coefficients

Fourier coefficients are defined as the overlap integral between the sine or cosine of a specific frequency and the signal from the time domain. The magnitude of each Fourier coefficient is therefore influenced by the average amplitude of the time-domain signal. To normalize all Fourier coefficients, the modulation values are divided by the zero order Fourier coefficient a_0 :

$$Modulation_k = \frac{\sqrt{(a_k^2 + b_k^2)}}{0.5a_0} \quad (4.7)$$

The position of the particle in relation to the center of the orbit is then given

through the amplitude of the first and zero order Fourier coefficients and the phase of the first order coefficients.

$$r_2 = f(r_1, \omega_0) \cdot \frac{\sqrt{(a_1^2 + b_1^2)}}{0.5a_0} \quad \varphi_2 = \text{atan} \left(\frac{b_1}{a_1} \right) \quad (4.8)$$

To convert modulation values to actual distances, it is necessary to introduce another scaling function $f(r_1, \omega_0)$ to convert modulations to real distances. The shape of the scaling function depends on the orbit radius r_1 and the beam waist size ω_0 of the point spread function. This scaling function is usually implemented as a combination of a look-up table and a binary search inside the tracking software to avoid a computational expensive analytical calculation during the localization process.

4.1.2 Axial Localization

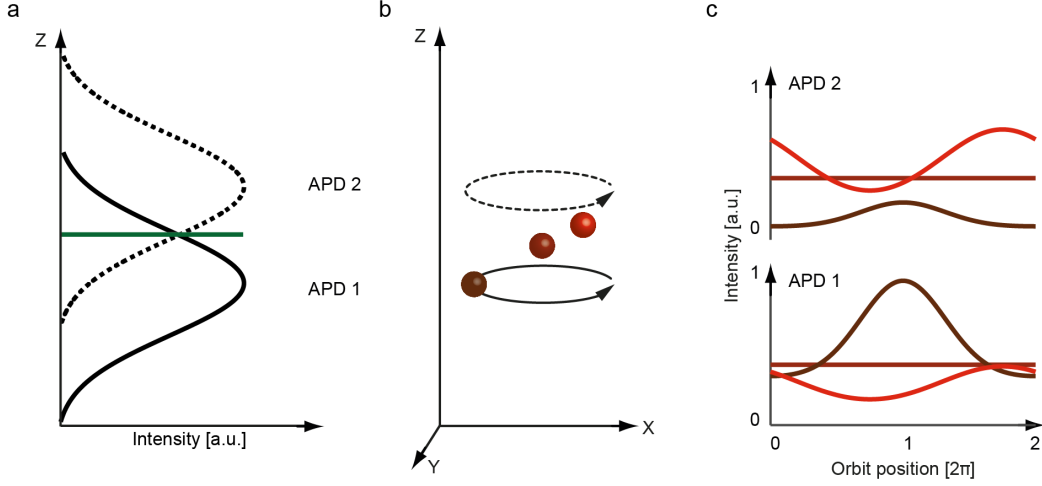


Figure 4.3 | Axial tracking principle: a) Point spread function of the two purposely misaligned detector channels (black and dashed Gaussians) with respect to the focal plane of the objective (green). b) Three dimensional representation of the orbits (black and dashed lines) and particles with different lateral and axial positions. c) Detected signals for all three particles, depending on the axial position, the count rate of each particle is distributed between the two detectors.

Axial localization is achieved through the misalignment of two confocal pinholes, which creates two detection planes, one above and one below the objective focus (Fig. 4.3). This alignment shifts both detection volumes away from the focus of the objective and splits the fluorescent signal from each particle between the two detectors. The resulting intensity distribution, normalized by the total intensity can be directly related to the z -distance from the particle to the focal plane of the objective through the introduction of a scaling function. Similar to the lateral scaling function $f(r_1, \omega_0)$,

$$d_z = g(d_{Planes}, \omega_z) \cdot \frac{I_1 - I_2}{I_1 + I_2} \quad (4.9)$$

The axial scaling function $g(d_{Planes}, \omega_z)$ depends on the ratio of the distance between the confocal detection volumes d_{Planes} and the beam waist along the z axis ω_z . The axial scaling function is implemented in the same way as the lateral scaling function.

4.2 Microscope Setup

The tracking microscope is a combination of a modified laser scanning confocal microscope for 3D single particle tracking and a standard wide-field microscope, which is used for environmental observation (Figure 4.4). A detailed list of components can be found in section 10.1.

4.2.1 Laser Excitation

All laser sources (405nm - Cobolt, 488nm - Coherent, 561nm - Cobolt and 633nm - Melles Griot) are located inside a box, which prevents the leakage of radiation. Several mirrors (M - Thorlabs) and dichroics (D5-D7 - AHF) are used to combine the lasers. A beam-splitter (BS - AHF, 70R/30T) is used to separate the laser lines between the confocal and wide-field microscope. Two acousto-optical tunable filters (Gooch & Housego) are used to modulate individual laser lines, which are guided to both microscopes using single mode fibers (Oz Optics).

4.2.2 Confocal Microscope

The laser emission is transferred from the laser box via a single mode fiber, collimated by an RGB corrected collimator (Schäfter & Kirchhoff) and guided over a quad-band dichroic (D3, zt405/488/561/640rpc - AHF), two galvano mirrors (Cambridge Technologies) and a telescope (L1, 80mm; L2, 250mm - Thorlabs) into the microscope body. Two silver mirrors (M1 & M2) are used to align the galvo scanner with the back entrance of the microscope body and the cage system, which contains the optical elements of the detection pathway. The fluorescence is first separated by color (D4, H 560 LPXR superflat - AHF) into a green and red channel and emission filters (EF2, 593/40 Brightline HC or 685/70 ET Bandpass ; EF3, 525/50 Brightline HC - AHF) remove residual laser reflections. The fluorescence in each channel is separated equally by using a 50:50 beam-splitter (BS - AHF) and coupled into multimode fibers (Thorlabs), which act as pinholes. All "pinholes" are slightly misaligned to create the detection planes for axial localization. Individual photons are recorded by avalanche photo diodes (Perkin Elmer and Laser Components).

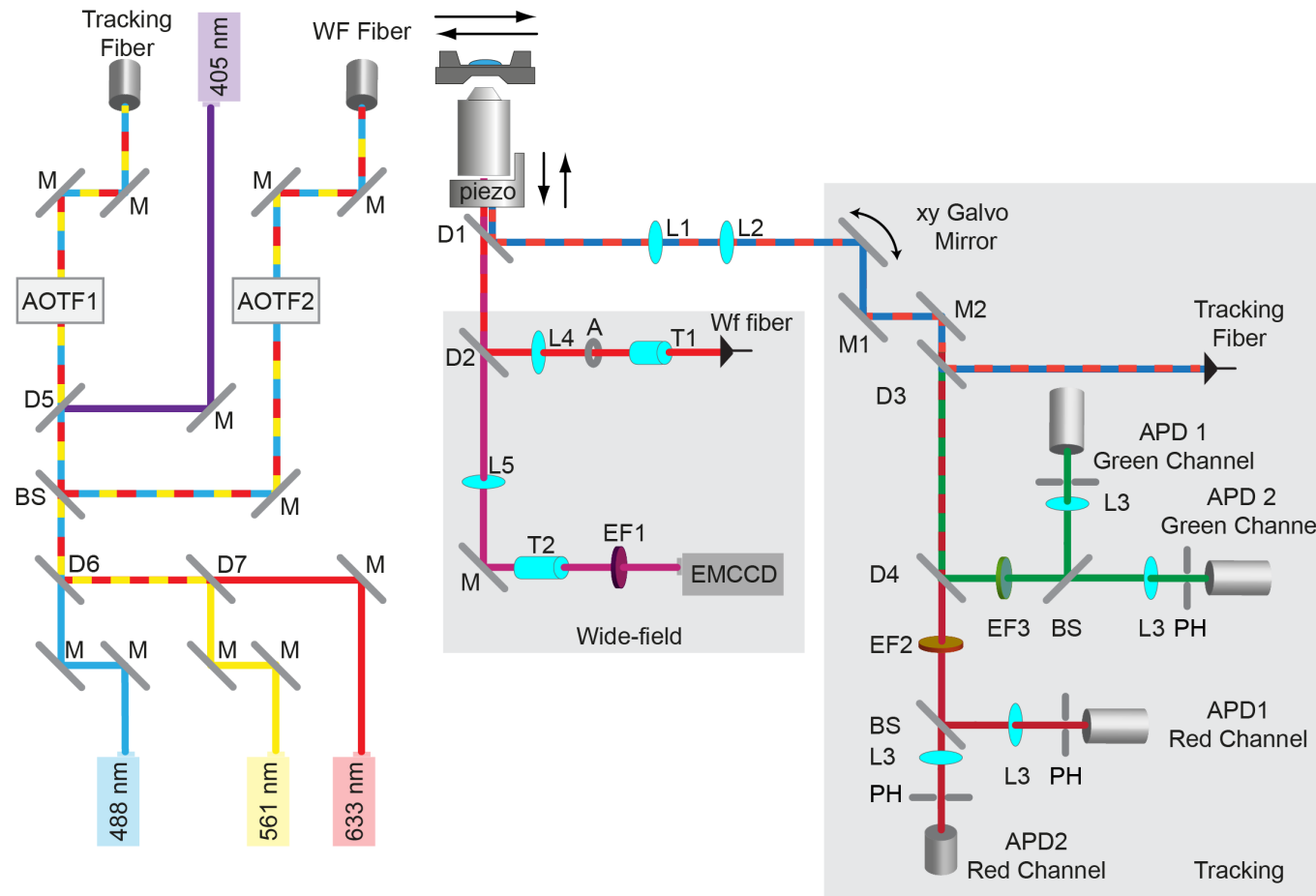


Figure 4.4 | 3D Orbital Tracking microscope schematic: D: Dichroic mirror, M: silver mirror, EF: emission filter, BS: 50/50 beam-splitter, PH: pinhole, L: lens, T: telescope, APD: avalanche photo diode

4.2.3 Wide-field Microscope

The emission of the single mode fiber from the laser box is collimated by an RGB corrected collimator (Schäfter & Kirchhoff) and expanded by a telescope (T1, 50mm & 150mm - Thorlabs). An aperture removes laser excitation from outside the cameras field of view and a 400mm achromatic lens focuses the rectangular beam over a quad-band dichroic (D2 - AHF) onto the back aperture of the objective. The tube lens (L5, 200mm - Thorlabs) can be shifted along the optical axis to couple the focus plane to the image plane of the EMCCD camera (iXon Ultra - Andor). A second telescope (T2, 50mm & 150mm - Thorlabs) magnifies the image and residual laser reflections are removed through an exchangeable emission filter (EF1 - AHF).

4.2.4 Microscope Body

The microscope body (Axiovert 200 - Zeiss) combines the confocal and wide-field microscope through different dichroics (D1 - AHF) located in the revolver below the objective. A z-objective piezo is used to change the axial focus position during the tracking feedback. The sample can be repositioned through a scanning stage, which in addition holds a XYZ piezo for calibration or a heating stage.

4.3 Tracking Program

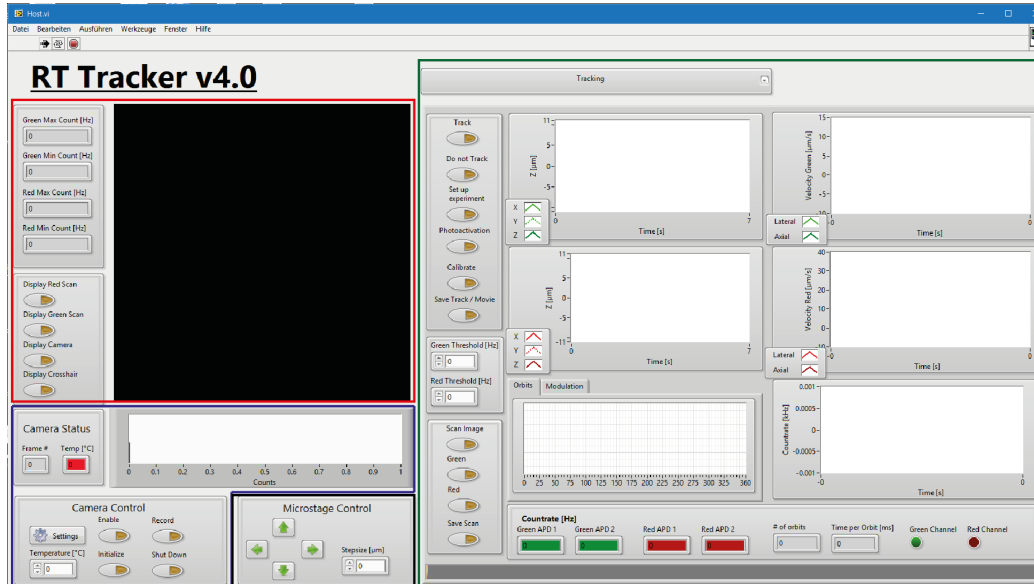


Figure 4.5 | User interface of the tracking software: Red: Displays confocal and wide-field images. Blue: Andor camera control. Black: Microscopy stage control. Green: Confocal microscope control.

The tracking software is a custom program written in LabVIEW (2012-2015), that synchronizes and controls the whole hardware of the microscope. To achieve a millisecond temporal resolution, it is necessary to perform the localization algorithm and other functionalities within less than $400\text{-}500\mu\text{s}$. A normal personal computer with a Windows operating system is not suitable for this task, since every thread running on the CPU (e.g. the tracking algorithm) can be interrupted by user interactions or other programs (e.g. Anti Virus Software). Solutions to this problem are real-time operating systems running a specialized hardware, micro-controllers or field programmable gate arrays (FPGA). Real-time operating systems and FPGA's offer the possibility to redesign or add functionalities, which is not possible for micro-controllers and thus a combination of a real-time computer and a FPGA was chosen to perform time-critical calculations. The tracking software is therefore distributed between a normal Windows operated computer and an embedded real-time computer, which contains a FPGA (compact RIO 9082, National Instruments). The FPGA provides a master clock source, which is used to synchronize the real-time and host computer and handles all analogue and digital communication. Due to the limited space on the FPGA,

the real-time computer performs the localization algorithm and additional functions of the tracking microscope. The host computer is used to process user inputs, to display and save the tracking data and operates the Andor EMCCD camera (Fig. 4.5).

All functionalities are implemented using the programming concept of state machines. A state machine consists of a while loop, which is permanently running during the execution of the program. Several cases inside this loop can be accessed and provide the ability to sequentially execute different code blocks. The selection of different cases is performed through user interactions, or through commands from other parts of the tracking software. The complexity of the tracking software requires the implementation of several state machines on the host computer, the real-time computer and the FPGA. A detailed description of all state machines can be found in the following sections.

4.3.1 Program Functions

To be able to track individual particles, the tracking software has to provide several features, which can be divided into three blocks: alignment, particle tracking and camera operation.

Alignment Functions

To perform an optimal alignment of the system, several functions are needed. A general alignment procedure is described in section 4.5. First, the software has to provide the ability to perform point intensity measurements to align the detectors using the fluorescent signal of a micro-molar dye solution. The second part during the alignment procedure requires a hard- or software based correlation unit to measure the auto- and crosscorrelation curves for each detector pairs. Up to now, an external FPGA based hardware correlator has been used for this alignment step [69], which will be replaced in the near future by software for the FPGA, developed by Frank Mieskes during his research internship. The last required function for the alignment process is a linear point scan to measure the position and width of the point spread function for each detector along the x, y and z-axis.

Tracking Functions

After the alignment of the tracking microscope, the confocal image area has to be aligned with the field of view of the wide-field microscope. After an initial manual alignment of the laser focus to the center of the camera field of view, an automated mapping procedure determines and saves the required parameters inside the tracking software.

After this last calibration step, single-particle tracking experiments can be performed. The first step is a two-dimensional confocal scan to localize the positions of particles inside the specimen. In a second step, the background intensity level is measured at various locations inside the confocal image. If the cumulated intensity value along all points along the orbit is higher than the threshold, the tracking algorithm is enabled. Intensity values smaller than the threshold enable a search mode, where the orbit is moved along a spiral path and screens for a particles in the vicinity of the start point. The tracking function is activated upon clicking on the location of a particle on the confocal image and is again stopped manually by the user. Two more functions provide the ability to save confocal image and trajectory data. Another type of tracking mode allows to measure the modulation of the recorded

intensity signal for each orbit and gives access to experimentally determined look-up tables.

Camera Functions

The last set of functions operate the EMCCD camera. Several functions are used to start the EMCCD camera, display the image data and to save the tif stacks to the harddisk.

4.3.2 Code Structure

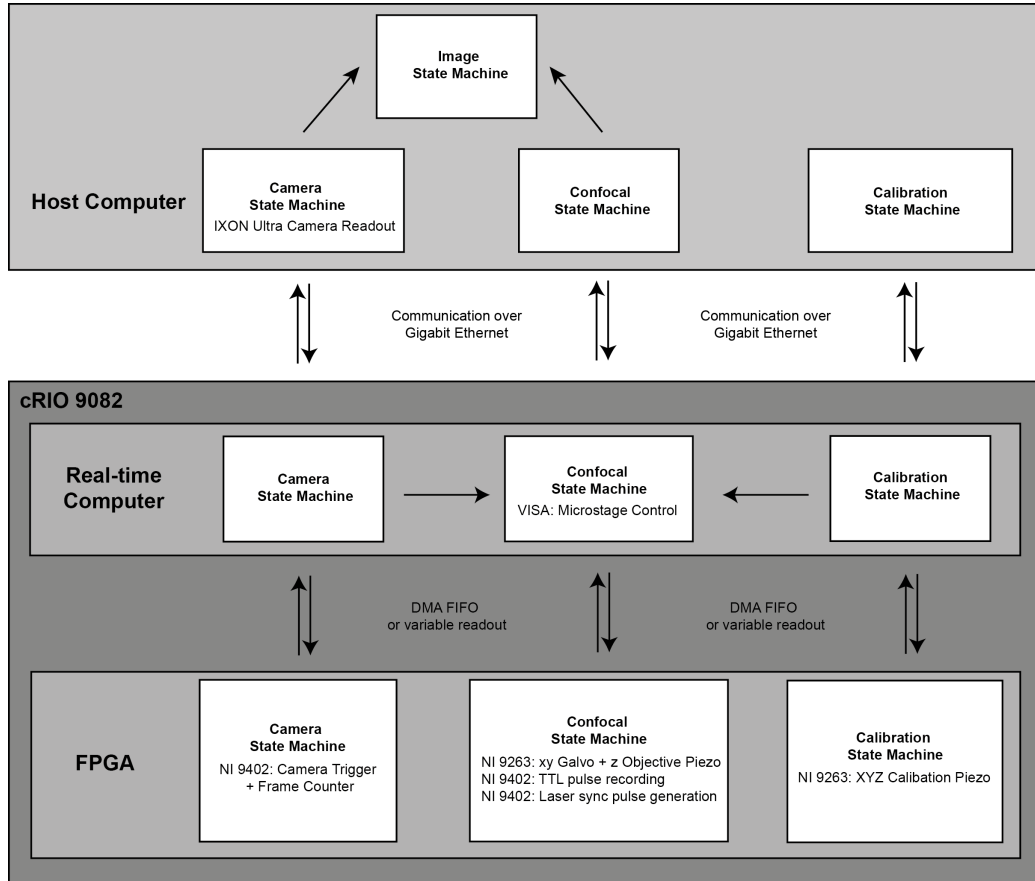


Figure 4.6 | Code structure of the orbital tracking software: Rectangular boxes represent state machines, black arrows indicate communication interfaces between state machines.

Figure 4.6 shows the internal code structure of the orbital tracking program. The host computer as the least deterministic part of the system is used to process user interactions and to display data in real-time. Time critical parts of the code are either processed on the real-time computer or, for highest time accuracy on the FPGA (which is used as a master clock for the software and to synchronize the microscope).

Three state machines operate the microscope. The confocal state machine controls the confocal microscope (including the orbital tracking feedback, Section 4.3.3). The camera state machine triggers the Andor camera and records the starting point of each frame and the calibration state machine controls an external xyz piezo stage, which is used to measure the perfor-

mance of the tracking feedback.

Communication between the host computer and the real-time system is achieved over a gigabit ethernet connection that can be interrupted by other network operations of the operating system and thus is a non-deterministic link between host and compact RIO system. Communication between real-time computer and FPGA happens on the same mainboard and is thus not biased through any other process. Each state machine uses a variable cluster and an enumeration constant for downstream communication and to submit the current state from the host state machine to the real-time and FPGA state machines. Upstream communication is achieved through direct memory access (DMA) first-in-first-out (FIFO) buffers or variable readouts (FPGA to real-time computer) and through a network stream FIFO (real-time computer to host). Three different variable clusters (one for each state machine) are used to transfer the control parameters between host and real-time computer and between real-time computer and the FPGA:

Variable Name	Data Type	Description
Bin Time [40 MHz Ticks]	U32	Bin Time per pixel or per orbit bin
Photoactivation Trigger	Boolean	Trigger for photoactivation
Green Channel Trigger	Boolean	Trigger for green laser
Red Channel Trigger	Boolean	Trigger for red laser
Rotation Angle	FXP 25,1	Rotation angle between camera and confocal coordinate system
Scaling Factor X Axis	FXP 20,5	Scaling factor between between camera and confocal coordinate system
Scaling Factor Y Axis	FXP 20,5	Scaling factor between between camera and confocal coordinate system
Translation X Axis	FXP 20,5	Shift between between camera and confocal coordinate system
Translation Y Axis	FXP 20,5	Shift between between camera and confocal coordinate system
Confocal Scan Pixels	Enum	Defines the amount of pixels for the confocal scan

Table 4.2 | Confocal State Machine Variable Cluster: Variables to control the state machine, which operates the tracking microscope.

Variable Name	Data Type	Description
X Green [V]	FXP 20,5	Particle x position in the green channel
Y Green [V]	FXP 20,5	Particle y position in the green channel
Z Green [V]	FXP 20,5	Particle z position in the green channel
X Red [V]	FXP 20,5	Particle x position in the red channel
Y Red [V]	FXP 20,5	Particle y position in the red channel
Z Red [V]	FXP 20,5	Particle z position in the red channel
X Offset [V]	FXP 20,5	X offset position to start the PSF scan
Y Offset [V]	FXP 20,5	Y offset position to start the PSF scan
Z Offset [V]	FXP 20,5	Z offset position to start the PSF scan
Orbit Radius [V]	20,5	Orbit radius for the tracking feedback
Dark Orbits	U32	# of dark orbits
Photoactivation every n^{th} orbit	U32	Activate 405nm laser every n^{th} orbit
Tracking Mode	Enum	Sequential or parallel tracking mode
Leading Channel	Enum	Green, red or both channels
# of channels	Enum	Single or dual color tracking
X Shift Lstep [μm]	I16	X stepsize for microstage
Y Shift Lstep [μm]	I16	Y stepsize for microstage
G-Factor Green 1	single	γ correction APD green 1
G-Factor Green 2	single	γ correction APD green 2

Table 4.2 continued: | Confocal State Machine Variable Cluster: Variables to control the state machine, which operates the tracking microscope.

Variable Name	Data Type	Description
G-Factor Red 1	single	γ correction APD red 1
G-Factor Red 2	single	γ correction APD red 2
Orbit Plane Distance [V]	FXP 20,5	Distance between the z psf maxima
Invert APD	Enum	Changes the order of APP's
Intensity Threshold Green [Counts/Orbit]	U32	Tracking threshold green
Intensity Threshold Red [Counts/Orbit]	U32	Tracking threshold red
Long Range Tracking	Enum	Long range tracking ON/OFF
Long Range Tracking Threshold [V]	single	Activation threshold long range tracking
Long Range Stage Treshold [μm]	I16	Stage travel distance for long range tracking
Measure LUT	Enum	Enables/disabled tracking feedback to measure LUT

Table 4.2 continued: | Confocal State Machine Variable Cluster: Variables to control the state machine, which operates the tracking microscope.

Variable Name	Data Type	Description
Exposure Time [ms]	U32	Exposure Time of the camera chip
Frame Transfer Time [ms]	U32	Image readout/shift time
Camera Frame	I32	Current Camera Frame

Table 4.3 | Confocal State Machine Variable Cluster: Variables to control the state machine, which operates the EMCCD camera.

Variable Name	Data Type	Description
Amplitude [V]	FXP 20,5	Sinus amplitude
Frequency [Hz]	single	Sinus frequency
Stepsize [V]	FXP 20,5	Distance between steps
Step Start [V]	FXP 20,5	Startposition for steps
# of Steps	U32	Total number of steps
Axis selection	Enum	X, Y, Z, X+Y, X+Y+Z
Movement Type	Enum	Sinus or Steps

Table 4.4 | Confocal State Machine Variable Cluster: Variables to control the state machine, which operates the calibration routine.

4.3.3 Confocal State Machine

As explained in the previous section, the confocal state machine operates the tracking microscope through the sequential execution of different functions. The structure of the state machine is depicted in Fig. 4.7. Upon initialization, the state machine resides in the "Idle" state and waits for a user interaction. If a certain function is activated by the user, the state machines of the real-time computer and the FPGA change to the same case and execute their subroutines. After the calling of each function, all state machines change back to the "Idle" case. Each case depicted in Fig. 4.7 is described in the following section.

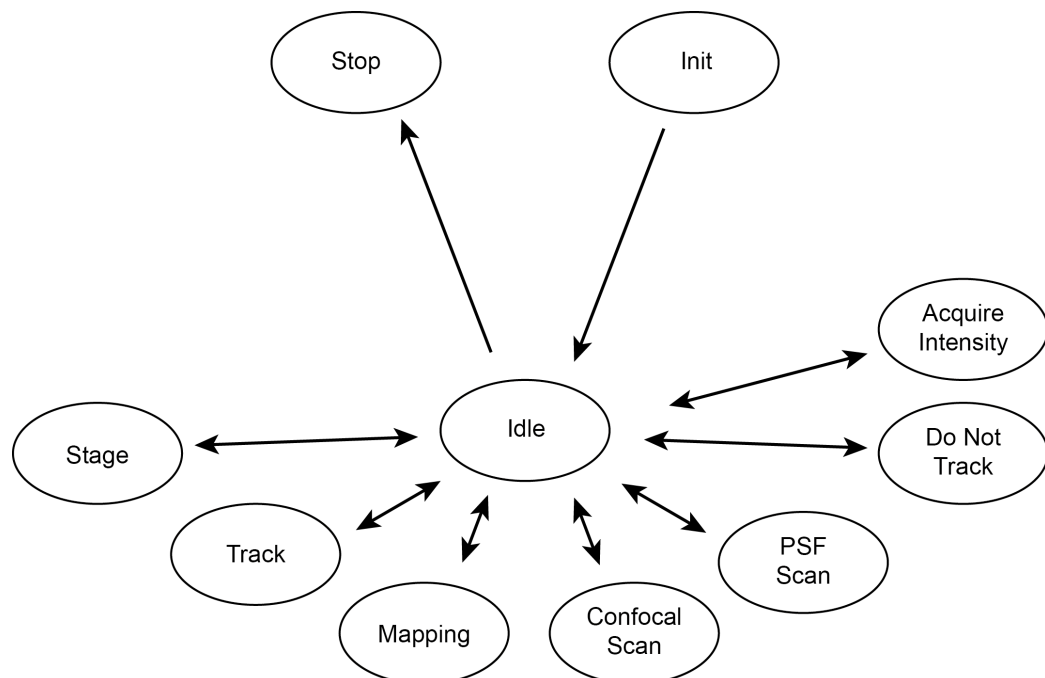


Figure 4.7 | Confocal state machine structure: Circles represent the individual cases of the confocal state machine. Arrows indicate possible transitions between cases.

Init

Host: Resets user interface, loads user data from a user profile, which is stored in the user home folder of the operating system and connects a network stream to the compact RIO embedded controller.

Real-time Computer: Loads and initializes the FPGA bitfile before entering the default state machine. Connects network stream to the host computer and opens a connection over the COM port to the microstage controller for sample repositioning.

Idle

Host Contains an event structure, which processes user interactions (e.g. entering other state machines, saving data and changing display settings).

Real-time Computer Continuously reads the status of the "Confocal State Machine" network variable.

FPGA Continuously reads the status of the "Confocal State Machine" FPGA variable.

Acquire Intensity

Performs a continuous intensity measurement at a fixed location.

Host Transfers acquire intensity settings (bin time and γ factors) to the real-time computer and enters a while loop that continuously reads out data from the network stream and updates the acquire intensity waveform chart on the user interface.

Real-time Computer Reads out intensity data from the FPGA DMA-FIFO buffer and transfers it via the network stream to the host computer.

FPGA Collect incoming TTL pulses from all four detectors and writes intensity bin data to the DMA-FIFO.

Do Not Track

Performs a single intensity measurement at a user specified location.

Host Records the cursor coordinates of the mouse, sends them to the real-time computer, performs an intensity point measurement at this location and updates the user interface with the countrate. In addition, the current position is transferred to the image handling state machine for image processing.

Real-time Computer Reads out intensity data from the FPGA DMA-FIFO buffer and transfers it via the network stream to the host computer.

FPGA Executes coordinate transformation and moves the laser focus to the requested position. Performs a point intensity measurement and writes intensity bin data to the DMA-FIFO.

Point Spread Function Scan

Performs a linear intensity scan along the x,y or z axis. The initial position is set through the "Do Not Track" function or the last known tracking position.

Host Perform a linear scan by repeatedly calling the "Do Not Track" subroutine. The full width at half maximum and peak position are acquired by fitting a one dimensional Gaussian to the data signal.

Real-time Computer Reads out intensity data from the FPGA DMA-FIFO buffer and transfers it via the network stream to the host computer.

FPGA Executes coordinate transformation and moves the laser focus to the requested position. Performs a point intensity measurement and writes intensity bin data to the DMA-FIFO.

Confocal Scan

Performs a lateral confocal scan with an area defined by the mapping function and the field of view of the camera. The number of pixels per axis and the total image time can be adjusted by the user.

Host Sends confocal scan settings (# of pixels, bin time per pixel, and coordinate transformation parameters to convert camera in confocal coordinates) to the real-time computer, reads out linewise data from the network stream and updates the user interface. The confocal scan data is written into a two dimensional array, which is processed into an image through the image handling state machine.

Real-time Computer Reads out pixel intensity data from the FPGA DMA-FIFO buffer and transfers it via the network stream to the host computer.

FPGA Executes coordinate transformation and moves laser focus along the specified two dimensional grid. The intensity data from all four detectors are measured in parallel and transferred over the DMA-FIFO to the real-time computer.

Mapping

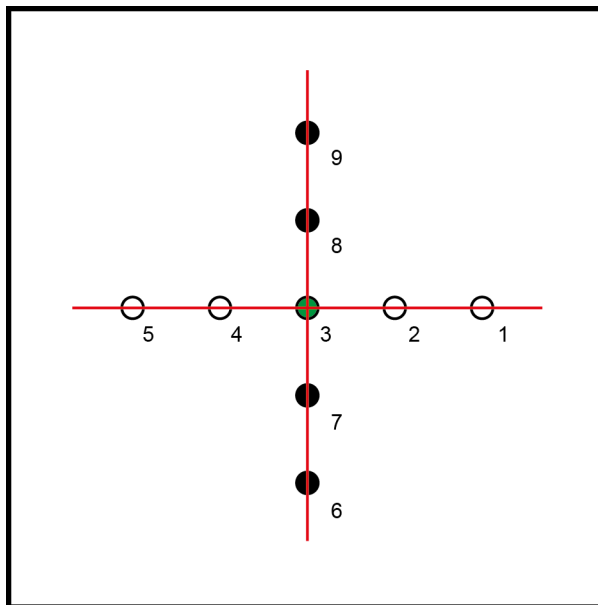


Figure 4.8 | Mapping procedure: Different back reflections of the laser on the coverslip surface (1-9), camera field of view is shown in black. Empty and black filled positions are used to calculate the scaling factors for the x and y axis. The x and y translation is derived from the center position. The rotation angle is calculated from the fit of each cross axis (red lines).

The mapping function is used to align the confocal image onto the camera field of view. To acquire the required coordinate pairs to calculate the transformation parameters, the back reflection of the laser from the coverslip surface is imaged on the EMCCD camera (emission filters are removed from the optical path). The laser focus is moved to nine positions using the galvano mirrors and the corresponding coordinates are extracted from each frame using a center of mass analysis around the maximum intensity value (Fig. 4.8). The transformation parameters are extracted using the following equations:

$$Scaling_x = \frac{((Pos_{x,5} - Pos_{x,1}) + (Pos_{x,4} - Pos_{x,2})) \cdot M}{2} \quad (4.10)$$

$$Scaling_y = \frac{((Pos_{y,5} - Pos_{y,1}) + (Pos_{y,4} - Pos_{y,2})) \cdot M}{2} \quad (4.11)$$

To avoid that the laser focus is moved outside the camera field of view, the magnification factor M can be adjusted to decrease or increase the size of the cross shown in Fig. 4.8.

$$Trans_x = -Pos_{x,3} \cdot Scal_x \quad (4.12)$$

$$Trans_y = -Pos_{y,3} \cdot Scal_y \quad (4.13)$$

$$\theta = \frac{(\tanh(\text{fit}(Pos_{x,1-5})) + \tanh(\text{fit}(Pos_{y,3,6-9})))}{2} \quad (4.14)$$

The coordinate transformation from camera to confocal coordinates is performed through the following equations:

$$x_{Confocal} = (x_{Camera} \cdot \cos(\theta) - y_{Camera} \cdot \sin(\theta)) \cdot Scaling_x + Trans_x \quad (4.15)$$

$$y_{Confocal} = (x_{Camera} \cdot \sin(\theta) + y_{Camera} \cdot \cos(\theta)) \cdot Scaling_y + Trans_y \quad (4.16)$$

The corresponding reverse transformation is given as:

$$\begin{aligned} x_{Camera} = & \cos \theta \cdot \left(\frac{x_{Confocal} - Trans_x}{Scaling_x} \right) \\ & + \sin \theta \cdot \left(\frac{y_{Confocal} - Trans_y}{Scaling_y} \right) \end{aligned} \quad (4.17)$$

$$\begin{aligned} y_{Camera} = & \cos \theta \cdot \left(\frac{y_{Confocal} - Trans_y}{Scaling_y} \right) \\ & - \sin \theta \cdot \left(\frac{x_{Confocal} - Trans_x}{Scaling_x} \right) \end{aligned} \quad (4.18)$$

The rotation angle of the mapping procedure is determined by a fitting routine and therefore, the output can slightly vary due to the low number of data points. To compensate for this inaccuracy several iterations of the mapping process are performed. The angle θ is used as an optimization threshold until the difference between two iterations is smaller than 0.3° . After a suc-

Successful calibration the transformation between the two coordinate system is performed in several other program functions.

Host The mapping subroutine uses the "Do Not Track" function for the 9 individual spots used for the coordinate transformation. Calculates the transformation variables and stops the subroutine when the threshold is reached. The photon counts from the point measurement are discarded.

Real-time Computer The real-time computer switches the Andor camera to single frame acquisition (using external triggering) and simultaneously uses the "Do not Track" function to move the laser focus.

FPGA Executes coordinate transformation and moves the laser focus to the requested position. Performs a point intensity measurement and writes intensity bin data to the DMA-FIFO.

Track:

The tracking subroutine performs the tracking feedback, which follows particles in a 3D environment. The modular software can be used to perform different tasks depending on the tracking settings:

Tracking Settings	Description
1 / Green /	Tracks a single particle using the green detector pair
1 / Red /	Tracks a single particle using the red detector pair
2 / Green / Sequential	Tracks a single particle using the green detector pair. Sequentially probes the environment using the red detector pair
2 / Green / Parallel	Tracks a single particle using the green detector pair. Simultaneously probes the environment using the red detector pair
2 / Red / Sequential	Tracks a single particle using the red detector pair. Sequentially probes the environment using the green detector pair
2 / Red / Parallel	Tracks a single particle using the red detector pair. Simultaneously probes the environment using the green detector pair
2 / None / Sequential	Tracks two particles sequentially
2 / None / Parallel	Tracks two particles in parallel

Table 4.5 | Available tracking modes: Depending on the experimental requirements, the tracking software offers several options to modify the single-particle tracking algorithm. The tracking settings include the number of channels, the leading channel and the option to execute the orbits sequentially or in parallel.

Table 4.5 shows the available tracking modes. The simplest approach uses only a single detector pair (green or red) and can track a single particle. The second group of tracking options offers the ability to track a single particle and to simultaneously probe the environment using the second detector pair. After every iteration, the laser focus is moved to the position calculated from the intensity data acquired by the leading channel. The second channel can be used to screen for interactions with other particles and also offers the ability to resolve the structure of the underlying cytoskeleton (see chapter 6 for details). In case of a significant spectral overlap between the green and red dyes used for tracking, it may be necessary to sequentially determine

the position of the green and red channel using alternating laser excitation. Otherwise, the fluorescent signal from the green channel will leak into the red channel and bias the calculated location of the red particle. In case of no or very small spectral overlap, it is recommended to perform a parallel dual-color tracking approach. The last group of tracking settings are designed to track two independent particles, one labeled with green and one with red fluorophores. Since the distance between the two particles can be on the order of a few micrometer, it is necessary to introduce several dark orbits to account for the time to move the laser focus between the two particle locations.

Additional tracking settings are used to design the execution scheme of the experiment. This includes the orbit time and special functions, such as dark orbits to reduce photobleaching in favor of measuring speed, long range tracking to prevent particles from leaving the camera field of view and interleaved photoactivation.

Implementation Of The Tracking Algorithm

The tracking algorithm can be divided into four sequential steps, orbit execution, position calculation, position update and data transfer, which are executed on different parts of the compact RIO system (Fig. 4.9). First, the FPGA performs the circular scan around the current three dimensional orbit offset. The intensity data of each orbit bin is sent over a direct memory access first in first out buffer (DMA-FIFO) to the real-time computer.

Once all 16 points per orbit are transferred, the FIFO is read out on the real-time target. Depending on the chosen tracking settings, only the orbit data of the used channel is forwarded. The orbit bin data from the unused channel (e.g. a disabled channel or for "dark orbits") is overwritten with a -1. In succession, a subroutine checks whether the total number of photons per orbit exceeds the user defined background threshold and uses a boolean value for each channel to indicate if a particle is in the vicinity of the orbit. Afterwards the software proceeds to calculate the new position of the particle and thereby the orbit offset from the intensity data (Fig. 4.10). In the first step of the lateral localization, the time dependent intensity signal, is Fourier transformed to the frequency spectrum using the fast Fourier transformation algorithm [68]. The amplitude value of the first order Fourier coefficients and the corresponding angle are calculated using eq. 4.7 and 4.8. The intensity ratio for the axial localization is calculated using eq. 4.9. Both distance values are then transformed through their respective scaling functions, which are implemented as look-up tables. Each look-up table contains 1024 data points and is scanned for the proper value pair. Instead of a linear search, where the search position determines the time needed to find the right value, a binary search is implemented. Both look-up tables are strictly monotonic functions and thus fulfill the requirements for a binary search. This approach ensures that the search time is constant and does not contribute to the calculation time jitter.

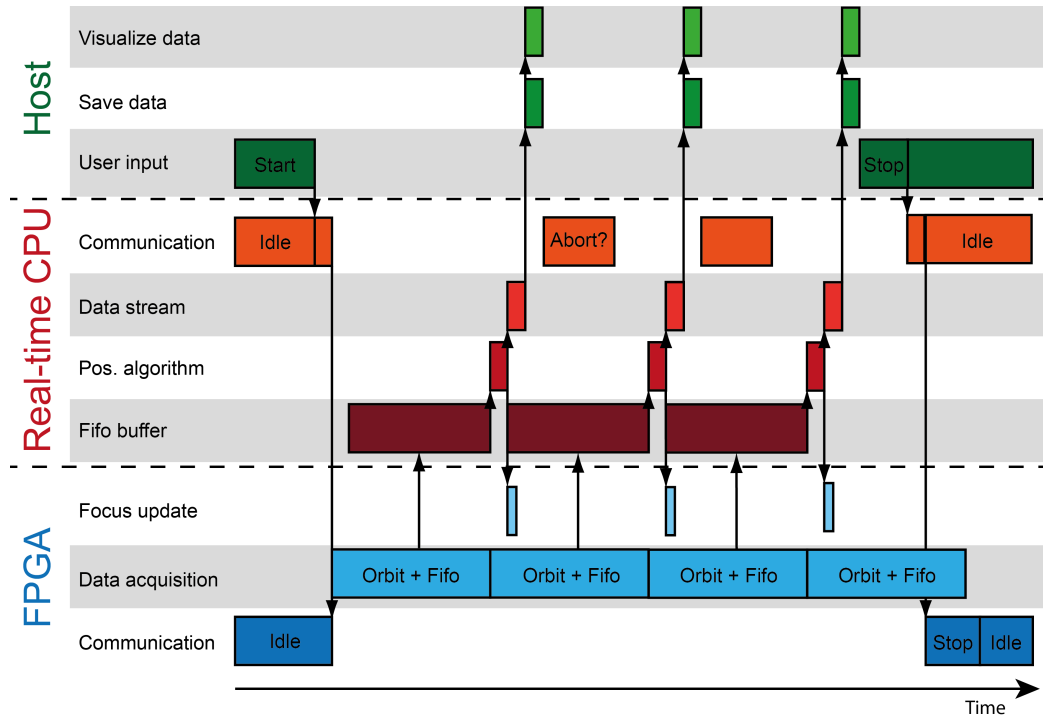


Figure 4.9 | Execution scheme of the tracking algorithm: After the user has enabled to tracking function of the software, the host computer send the start command to the real-time CPU and the FPGA. The FPGA starts the continuous rotation of the laser orbit. During the orbit, each data point is transferred to the real-time CPU using a FIFO buffer. Every 16 data points, the tracking algorithm calculates the new location of the particle and updates the position of the orbit on the FPGA. During the next orbit rotation, the position data along with other parameters is transferred to the host computer and visualized on the user interface. After every data transfer, the real-time CPU checks if the user stopped the tracking of the particle and if a stop signal is received, aborts the tracking process on the real-time CPU and the FPGA. The communication between the FPGA, real-time CPU and Host is indicated through black arrows.

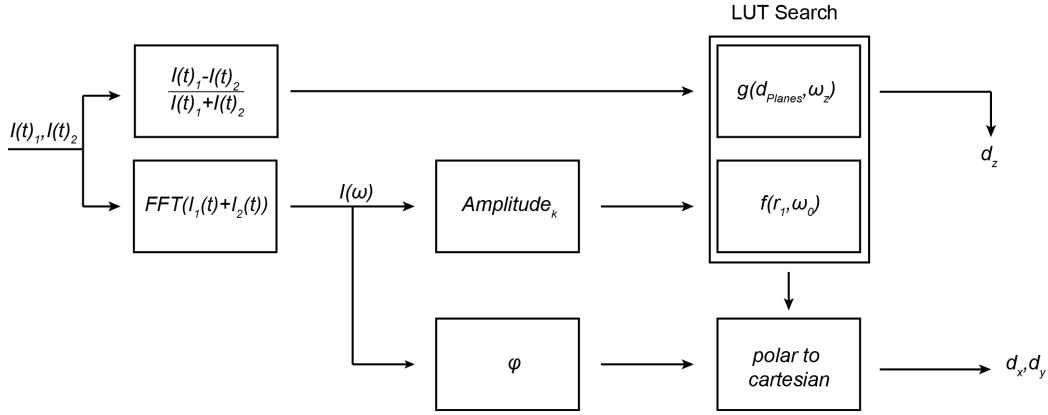


Figure 4.10 | Program flow of the localization algorithm: Square boxes represent subroutines and arrows indicate data flow.

Regardless of the chosen tracking mode (Table 4.5), the tracking software always performs the localization for both channels (first the green and afterwards the red channel). The position update for both channels inside the variable cluster follows the logic depicted in table 4.6. For channels with a negative total intensity, the position is not updated. If the countrate of a channel does not exceed the user defined threshold level, a search routine is performed until the counts have risen above the threshold. The search routine moves the center of the orbit with each iteration in a spiral pattern and tries to find the particle in the area around the starting point. In the last step of the position calculation, the subroutine for long-range tracking is executed. If the long range tracking is enabled, the subroutine checks whether the particle has moved outside a user defined area. If this condition is true, the real-time computer moves the microstage on top of the microscope in the opposite direction of the particle motion (see section 4.3.3 for details). In addition, a new tracking origin is saved in a second "Confocal State Machine Variable Cluster", which is then further used as a starting point to relocate the particle with the tracking algorithm after the microstage motion is completed. Due to the time it takes to move the stage (35-70ms) only a one long range event can be processed per subroutine call.

The maximal execution time of the whole localization process varies between $\sim 700 \mu s$ for dual color tracking with enabled long-range tracking and $\sim 100 \mu s$ for tracking of a single particle with disabled long-range tracking. Hence $t_{Orbit} \gg t_{Calc}$ and it is possible to update the offset during the execution of the next orbit. This "on the fly" update does not interrupt the movement of the scanner and is thus preferred over a sequential approach, which would perturb the continuous motion of the galvo mirror. Although the first 1-2

Tracking Settings	Update Logic
1 / Green /	$Pos_{Green} = Pos_{Green} + Pos_{Loc}$
1 / Red /	$Pos_{Red} = Pos_{Red} + Pos_{Loc}$
2 / Green / Green channel	$Pos_{Green} = Pos_{Green} + Pos_{Loc}$
2 / Green / Red channel	$Pos_{Red} = Pos_{Green} + Pos_{Loc}$
2 / Red / Green channel	$Pos_{Green} = Pos_{Red} + Pos_{Loc}$
2 / Red / Red channel	$Pos_{Red} = Pos_{Red} + Pos_{Loc}$
2 / None / Green channel	$Pos_{Green} = Pos_{Green} + Pos_{Loc}$
2 / None / Red channel	$Pos_{Red} = Pos_{Red} + Pos_{Loc}$

Table 4.6 | Update Logic for different tracking settings: Tracking settings contain the # of channels and the leading channel. The third parameter indicates the channel that is updated.

points of the orbit are executed with the old offset parameter, the ”on the fly” method does not significantly impair the particle localization accuracy (Fig. 4.14).

In the last step, the algorithm on the real-time CPU reads out the current camera frame and calibration position data from the FPGA and converts all orbit data for both channels into an array. To decrease the data transmission overhead between the real-time CPU and the host computer, the data from both tracking channels is transferred together as an unsigned 64-bit integer (U64). This is done by converting the single data type of each channel into a boolean array. The two arrays are combined and converted to an U64 number, which contains the data from both channels. If the total intensity from either the green or red channel contains no photons, the data is discarded instead of being transferred to the host computer.

The tracking software will continuously try to follow a single particle until the fluorescent signal of the particle drops below the user defined threshold or the tracking operation is canceled. If the algorithm encounters a second, brighter particle during the tracking process, the orbit intensity data is the sum of the fluorescent signals from both particles. Since the tracking algorithm calculates the center of mass of the fluorescent signal inside the orbit, the tracking algorithm will move the laser focus towards the brighter particle and with every iteration of the orbit, the contribution of the dimmer particle will become smaller. After a few iterations, the recorded intensity during one orbit originates to 100 percent from the brighter particle.

Host Several subroutines are required to control the tracking algorithm. The first routine is used to select the tracking parameters, e.g. orbit time and leading channel. Afterwards, the tracking is started by selecting a point in the overlay of the wide-field and a previously acquired confocal image. The camera coordinates (the user interface displays all position data in camera coordinates) are transformed to confocal coordinates on the host computer and the tracking parameters are transferred to the real-time computer and the subroutine starts to read out tracking data from the network stream. If the Andor camera is enabled, the software simultaneously acquires the images from the wide-field microscope. The orbit data is then processed to provide a real-time update of the following parameters:

Display parameters	Unit	Description
Position Green	$[\mu m]$	X,Y,Z position of the green channel
Position Red	$[\mu m]$	X,Y,Z position of the red channel
Velocity Green	$[\mu m/s]$	Instantaneous velocity of the green channel
Velocity Red	$[\mu m/s]$	Instantaneous velocity of the red channel
Countrate	[Hz]	Average countrate along the orbit
Orbit Shape	[a.u.]	Displays orbit intensity from all four detectors
Modulation	[a.u.]	Displays amplitude value
# of Orbits	-	Number of executed orbits
Time per Orbit	[ms]	Execution time per orbit
Boolean Indicators	-	Indicates if a particle is tracked
Camera Frame	-	Current camera frame

Table 4.7 | Output parameters of the tracking routine: All parameters are displayed in real-time in different panels on the user interface.

In addition, the current position of the particle is transformed back into camera coordinates and handed over to the image handling state machine to plot the position of the tracked particle onto the the RGB image, which displays both confocal channels and the wide-field image. To avoid a processor overload, the tracking data is only processed every 50ms. To avoid an excessive use of the computer RAM, the tracking data is written every 1000 orbits into temporary text files on a solid state disk. All data can be saved after the experiment via an additional subroutine. Each data file contains a header with the selected acquisition settings and the tracking data:

Columns	Description	Unit
1-3	Position of the particle in confocal coordinates	$[\mu m/s]$
4-6	Position of the particle in camera coordinates	[Pixel]
7	Orbit number	-
8	Orbit Time	$[\mu s]$
9	Camera Frame	-
10	Indicates if a particles was tracked	0/1
11,12	Stage movement during a long range tracking event	$[\mu m]$
13,14	Countrate of detector 1 & 2	[Hz]
15-31	Orbit bin data detector 1	[Counts]
32-46	Orbit bin data detector 2	[Counts]
47-49	Position of the external calibration piezo stage	$[\mu m]$

Table 4.8 | Data structure of the output files: After each tracking experiment, the acquired data can be saved as separate text files for each channel.

Real-time Computer In a first step, the real-time computer loads the look-up table into the random access memory and writes the tracking settings to the FPGA. In succession, the tracking algorithm is executed as described above until the user aborts the process.

FPGA The FPGA performs two functions. The FPGA controls the circular motion of the orbit in a multi step process. In a first step, the orbit for the x and y axis is calculated. In a second step, a "orbit activation logic" subroutine controls the status for each excitation channel over the AOTF for the chosen tracking settings. During the third step, the orbit is executed using the offset of the leading channel. The intensity values, which are measured during each orbit bin, are transferred via the DMA-FIFO to the real-time CPU. During the optional fourth step, the photo activation laser is enabled. Steps two to four are repeated until the tracking operation is aborted. In parallel, rising edges of incoming TTL pulses from the Andor camera are counted and used to synchronize frames with individual orbits.

Stage

A motorized microstage on top of the microscope allows the repositioning of the sample prior to and during the experiment. Data communication is performed via a set of ASCII commands over a RS232 connection between the real-time computer and the microstage controller. Depending on the

chosen axis, a move command for small distances ($\sim 1 - 20\mu s$) requires a processing time between 35 (x-axis) and 70 ms (y-axis).

Host Processes the user input and travel distance and transfers the data to the real-time computer.

Real-time Computer During the initialization process of the real-time routine, the communication between real-time computer and microstage controller is initialized with a baud rate of 57600, 8 data bits, no parity and two stop bits. In a second step, the input units of the controller are set to μm using the "!dim 1 1 1" command. After the initialization, each movement of the microstage is performed using the "!mor dimx dimy dimz" command. Both commands require a carriage return after the last input value.

Stop

Host Writes program settings into user profile and disables the real-time routine via the "Start Realtime" network variable.

Real-time Computer Closes the communication to the microstage controller and unloads the bitfile from the FPGA.

4.3.4 Camera State Machine

The camera state machine of the tracking software has to perform several function to operate and synchronize the Andor EMCCD camera with the other parts of the microscope. First, the tracking software has to be able to operate the camera in various acquisition modes (internal or external triggering, exposure and frame transfer times, frame transfer, EM gain, pixel readout speed and line shift speed). Regardless of the camera settings, each frame has to be synchronized with the tracking data (synchronization can be achieved by reading out the fire pulses of the camera). To avoid unnecessary bleaching during the frame transfer period of the camera, the laser excitation of the wide-field microscope should be synchronized with the exposure time of the CCD chip. The last function is the possibility to save the image data as a tif-stack on the hard disk.

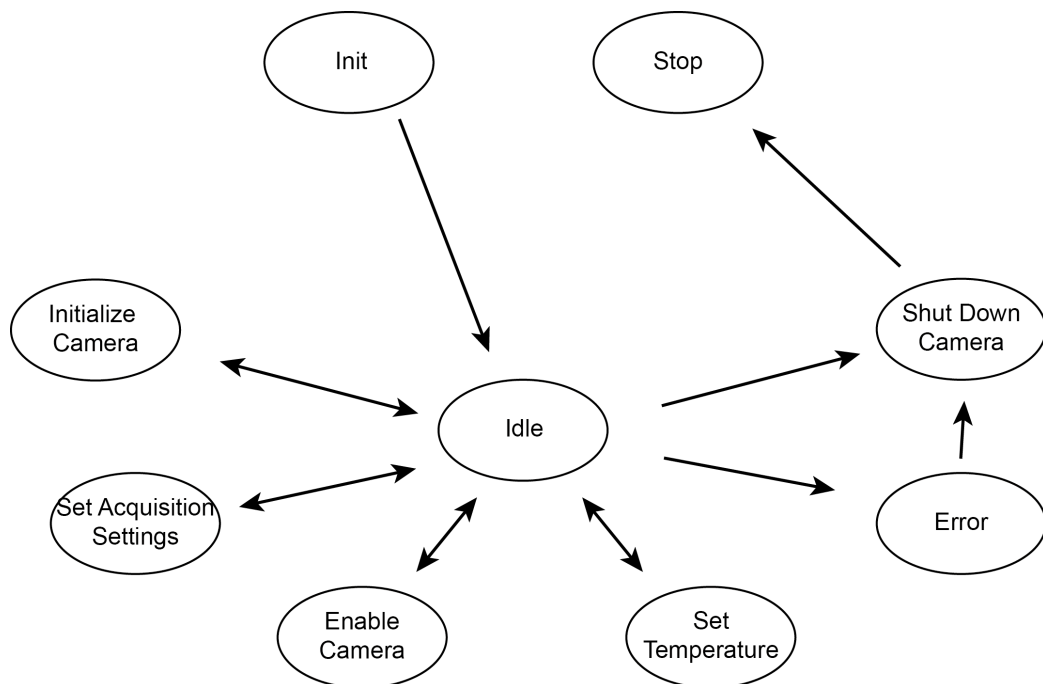


Figure 4.11 | Camera state machine structure: Black arrows indicate transitions between states.

The camera state machine (Fig. 4.11) controls the Andor IXON Ultra camera, which is used to record environmental information. Communication between the camera and the tracking software is performed via 28 subroutines, which use a dll library provided through the Andor Software Development Kit.

Init

Resets the properties of the camera settings control cluster.

Idle

Host Contains an event structure, which processes user inputs from the camera settings control cluster. If the camera is initialized, the idle case reads out the current chip temperature and displays the value on the user interface. In addition, the real-time camera state machine case is changed to the idle state via the "Camera State Machine" network variable.

Real-Time Computer Forwards the camera trigger options to the FPGA.

Initialize Camera

This case enters the initialization process of the camera. The software opens a handle to the camera and proceeds to read out the camera properties with the following subroutines:

Subroutine Name	Output
Get Detector Pixel Size	Pixel size of the camera chip
Get Line Shift Speeds	Line shift speed values
Get Recommended Line Shift Speed	Optimal line shift speed
Get Pixel Readout Speeds	Pixel readout speed values
Get Temperature Range	Temperature range of the thermoelectric cooling system of the camera chip
Get EMCCD Gain Range	EMCCD gain range
Get Pre Amp Gain Values	Preamplifier values

Table 4.9 | Camera properties: The available camera settings are read out from the camera during the initialization process.

The camera property values define the allowed input values for the "Set Acquisition Settings" state. In the end the thermoelectric cooling system is enabled with the default value from the user profile, the camera shutter is opened and the air cooler is switched on to remove excess heat from the thermoelectric cooling system.

Set Temperature

Uses the "Set Temperature" subroutine to change the target temperature of the camera chip.

Set Acquisition Settings

Opens a user interface panel showing the available camera properties. The camera modus is selected by choosing a combination of the settings displayed in table 4.10. To guarantee the normal operation of the camera, several pa-

Subroutine Name	Description
Set Acquisition Mode	Default parameter: "Run till abort"
Set Frame Transfer Mode	0 = Off, 1 = On
Set Readout Mode	Default parameter: "Image"
Set Image	Pixel binning parameter, default parameters: no binning
Set Exposure Time	Frame exposure time
Set AD Converter Channel	Default parameter: 0
Set Pixel Readout Speed	Pixel readout rate
Set Line Shift Speed	Line Shift Speed
Set Trigger Mode	Selects the camera trigger mode
Set EMCCD Gain	Sets the EM Gain value
Set Pre Amp Gain	Sets the pre amp gain value

Table 4.10 | Acquisition settings subroutines: The functions are called from the dll in the order of appearance.

rameters can not be selected by the user. This includes the camera acquisition mode. The only acquisition mode of that utilizes the FIFO buffer inside the camera is the "Run till abort" mode. Hence the host routine of the tracking software can be interrupted by other processes of the operating system a FIFO buffer prevents data loss for fast acquisition rates. The "Set Readout Mode" and "Set Image" functions are used to crop or bin the available area on the camera chip. As the software is designed to process the full area of the camera, both options can not be changed through a user interaction. The last default parameter, "Set AD Converter Channel", has to be called before starting the camera, although only a single analogue to digital converter is present.

Enable Camera

The enable camera state uses three subroutines (Start Acquisition, Get Image and Abort Acquisition) to control the camera readout. The image acquisition is started by calling the "Start Acquisition" subroutine. If the external trigger mode was selected, the FPGA starts to create TTL pulses, triggering individual frames on the camera. The camera is operated in the "Run till abort" mode, which uses a FIFO buffer to store recorded images in the camera RAM until the data is read out. Images are read out using the "Get Image" function and the 2 dimensional array is sent to the Image State Machine for further processing. The displayed images can be saved as TIFF stack using the open source CamTIFF library, developed by Ryan Orendorff and published under the GNU General Public License [70]. The CamTIFF functions are implemented as a nested state machine and writes the two dimensional image data to a temporary TIFF stack on the solid state disk. While the camera is enabled, the chip temperature is read out every 1000th iteration of the readout loop. As the "Get Temperature" subroutine has an execution time of approx. 35ms, this approach allows to update the temperature while providing a quasi uninterrupted display of the image data. The image acquisition is stopped using the "Abort Acquisition" function and the state machine returns to the idle state.

Error

The error state contains an error handler that switches off the camera and displays a message if an error occurs during the camera operation (for example if the user tries to initialize a camera that is not powered on).

Shut Down Camera

Closes the camera shutter and releases the handle to the camera and the dll.

Stop

Upon exiting the compiled application, the state machine first shuts down the camera and closes the user interface of the tracking software.

4.3.5 Image State Machine

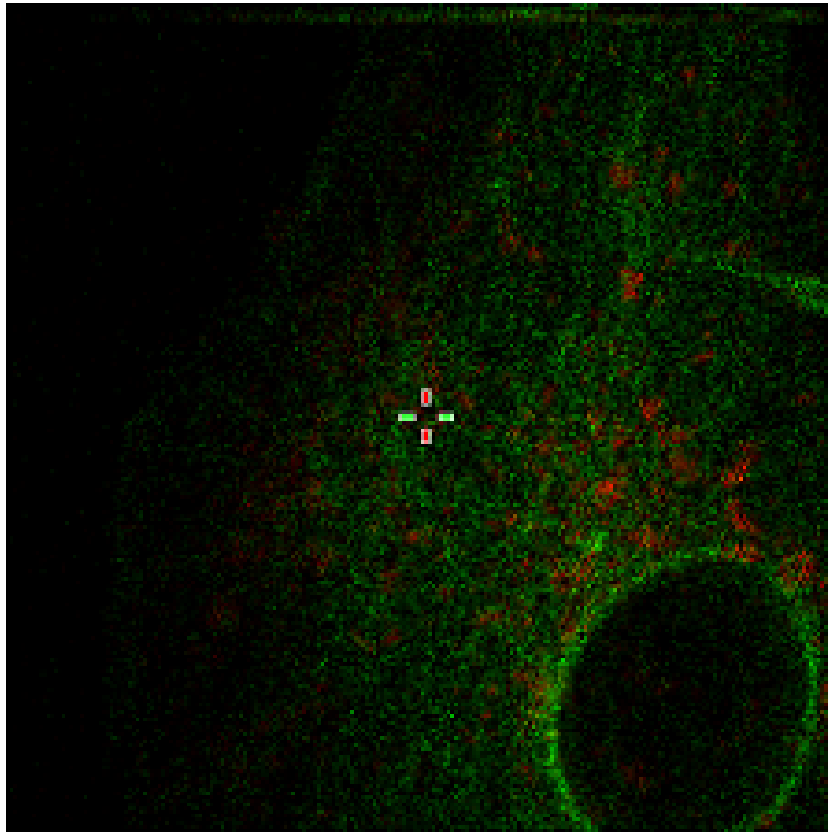


Figure 4.12 | Dual color image of a BSC-1 cell stably expressing GFP-Tubulin (green) and Lamp2-mCherry (red): The position of the tracked lysosome is indicated by the green/red crosshair. The original confocal image contains 256x256 pixels and is extrapolated to 512x512 pixel to match the pixel number of the camera chip.

The image state machine provides a real-time display of the wide-field images, the two confocal images and the current position of the tracked particle. All 3 images are combined into a single RGB image (red image data: red confocal scan, green image data: green confocal scan, blue: wide-field image). The state machine contains three states: "Init", "Active" and "Stop".

The "**Init**" state creates an image handle with 16bit color depth and 512x512 pixels during the initialization process of the tracking software. In addition, the local variables, which are used to transfer data to the image state machine, are reset.

The ”**Active**” state contains an event structure to process user inputs from the count rate histogram of the wide-field image. During the timeout case, the RGB image is updated with the data stored in the local variables used to transfer data between the confocal, camera and image state machine.

Confocal image data can consist of a variable number of pixels (2^n pixels with $n = 5 - 9$). To create an overlay of the wide-field and confocal image, the number of pixels in both image have to be identical. Depending on the number of pixels in the confocal image, each confocal pixel is repeated m times ($m = 9 - n$) along the x- and y-axis to create m^2 new pixels that are used to replace the single pixel from the original image. Both confocal images are rotated and inverted to match the image orientation of the Andor camera. In addition, the maximum pixel count rate of each channel is displayed in the user interface.

The intensity values from all pixels in the wide-field image are transformed into a histogram plot and displayed in the user interface to provide a feedback about the intensity range inside the wide-field image. The standard option autoscales the intensity values inside the image to provide the best contrast. It is also possible to adjust the contrast of the image via the histogram plot on the user interface.

The ”**Stop**” state stops the operation of the image state machine when closing the tracking software.

4.3.6 Calibration State Machine

The calibration state machine controls an external xyz piezo stage, which is used to measure the performance and calibrate the system. This state machine contains three states, "Idle", "Calibrate" and "Stop". The "Idle" state contains an event structure to process user interactions. The "**Calibrate**" state opens a new user interface window with two calibration options. The first function generates a sine wave, which is used to move a sample that usually contains multi-fluorescent beads to measure the localization precision. The second function generates a step motion along different axes. This function is used to measure conversion factors ($\mu m/V$) to transform the analogue voltages for each axis (galvo mirrors and z-objective piezo) to distances. Upon activation, the calibration settings are transferred to the real-time computer and forwarded to the FPGA subroutine. This process is handled by the "Idle" state of the Camera State Machine loop. The FPGA generates the analogue voltages for the xyz piezo stage and in addition, the current step number is read from the FPGA subroutine and transferred to the host computer. To monitor the motion of the external piezo stage along with the position of the tracked particle, the current position of the stage is read out during each orbit and recorded along with the other tracking data in the data file.

4.4 Microscope Performance

4.4.1 Acquisition Speed

The tracking software allows the modification of the acquisition speed with several parameters. First, the time per orbit can be as small as 2ms for very bright particles ($\sim 500 - 1000$ photons per orbit). However, this acquisition interval drives the z-objective piezo beyond its recommended resonant frequency and thus is highly susceptible to alignment errors and the chosen look-up table. If the parameters are not perfect, over- and underestimation of the z position leads to strong periodic fluctuations along the z axis. Orbit times of 3 ms and higher usually can provide proper localization precision. The maximal orbit time depends on the speed of particle motion. As long as the particle does not significantly move during one full orbit rotation, the acquisition time can be increased to seconds. The acquisition time can be further decreased by adding dark orbits. In general, a compromise between acquisition speed and the count rate per orbit has to be found to provide optimal experimental conditions for the target specimen.

4.4.2 Particle Tracking Performance

Localization Precision

The localization precision of a single particle depends on the signal-to-noise of the fluorescent signal, the grid size of the implemented lookup table, the noise on the generated analogue signals, the noise of the chosen hardware (galvo mirrors & objective piezo) and on the stability of the microscope.

The localization precision can be measured using a specimen containing beads in a polymer (refractive index $n=1.333$), which is externally moved with a xyz piezo stage (Fig. 4.13). In a first step, a stationary particle is localized over a certain time. The localization precision for a stationary particle is then given as the standard deviation of the recorded position signal. To determine the localization precision for a moving particle, the sample is moved in a sinusoidal pattern along each axis. The signal is fitted with a sine function and the localization precision for a moving particle is then determined through the standard deviation of the fitting residuals. The localization precisions for a stationary and a moving particle yield identical results. Unless noted otherwise, the localization precision is given as the mean between the two measurement conditions.

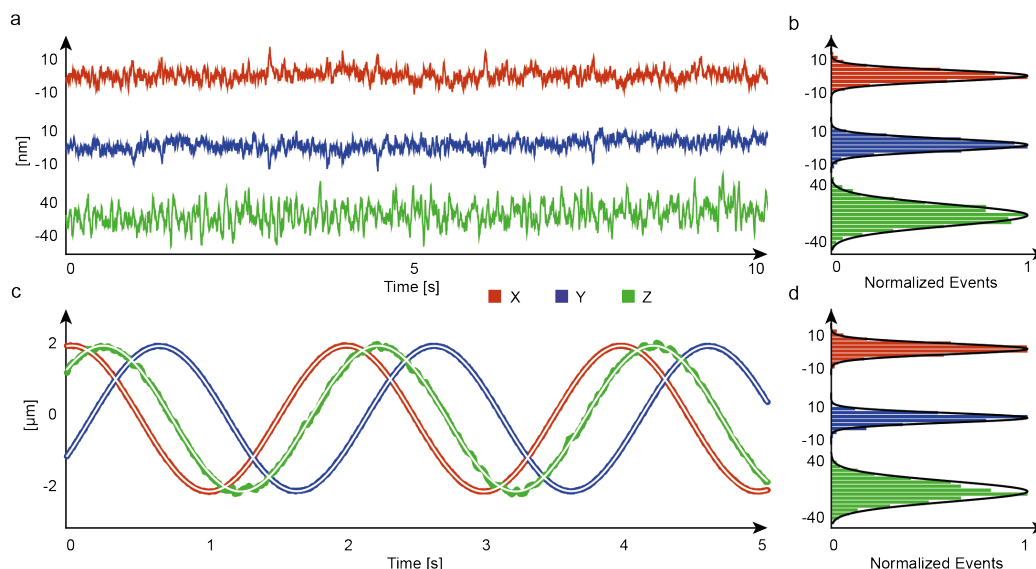


Figure 4.13 | 3D Orbital Tracking localization precision: a) Localization signal of a stationary multi fluorescent bead embedded in a polymer (acquisition rate 200 Hz) b) Localization precision, determined from the standard deviation was $< 3\text{nm}$ laterally and $< 21\text{ nm}$ axially. c) Localization signal of the same bead as in a) moved with a maximum velocity of $6.2\ \mu\text{m/s}$ by the external xyz piezo stage. Sinusoidal fits are indicated as white lines. d) Localization precision determined from the standard deviation of the fitting residuals. The results were the same as for the stationary particle.

The theoretical localization precision of a shot-noise limited particle localization is given as:

$$\sigma_{min} = \frac{0.425\omega_o}{\sqrt{I_{Orbit}}} \quad (4.19)$$

where ω_o denotes the beam waist and I_{Orbit} the total intensity per orbit [62]. Fig. 4.13 shows the measured countrate dependant localization precision for the x and y axis assuming a lateral beam waist of 203nm calculated by:

$$\omega_0 = \frac{0.51\lambda}{NA\sqrt{2\ln 2}} \quad (4.20)$$

using a wavelength of $\lambda = 561\text{nm}$ and a numerical aperture of $NA = 1.2$. It is notable that the measured localization precision is very close to the theoretical limit and therefore shot-noise limited. The small difference between the x- and y-axis can be explained by the fact that the orbit rotation starts

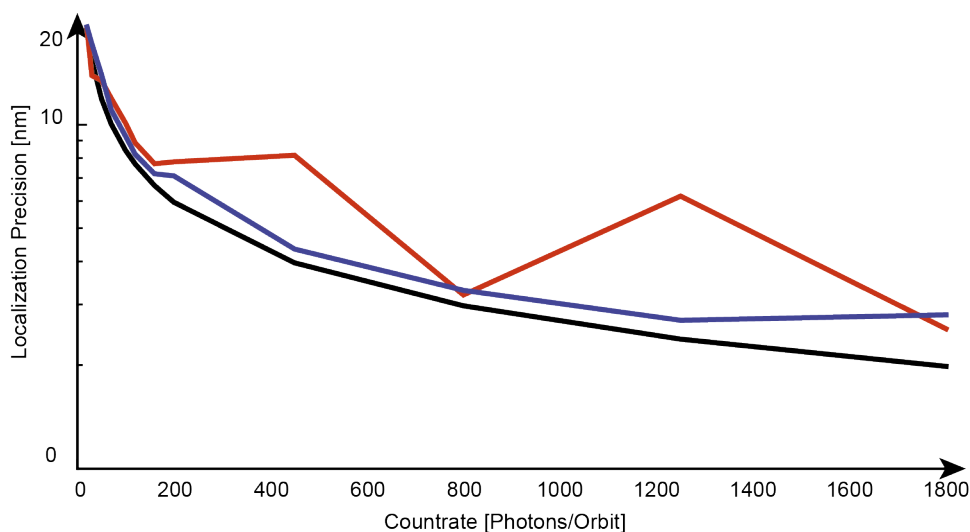


Figure 4.14 | Countrate dependent lateral localization precision: Comparison between the theoretical (black) and experimental (x-axis red, y-axis blue) count rate dependent localization precision.

at the x-axis and the on-the-fly update mechanism of the tracking algorithm slightly decreases the localization precision. Other error sources, e.g. errors in the look-up table and the analogue voltage generation do not deteriorate the localization precision, showing the exceptional stability of the system, the hardware components and the microscope.

The axial localization precision can be calculated using eq. 4.19 and depends on the axial beam waist. If the pinhole diameter is in the range of one airy unit, the axial beam waist is given as:

$$\omega_z = \frac{0.75\lambda}{n - \sqrt{n^2 - NA^2}} \quad (4.21)$$

where n describes the refractive index of the immersion fluid. For $\lambda = 561\text{nm}$, $n = 1.333$ and $NA = 1.2$ the minimal axial beam waist is 557nm . Fig. 4.15 shows the measured countrate dependent axial localization precision, which in comparison is worse than the lateral precision. This difference is caused by the utilization of a pinhole of ~ 4.5 airy units ($50\mu\text{m}$), which significantly increases the axial beam waist. A smaller pinhole would increase the localization precision in the axial direction through the smaller width of the point spread function along the z-axis, but decrease the precision due to the lower number of emitted photons. However, most biological particles have a

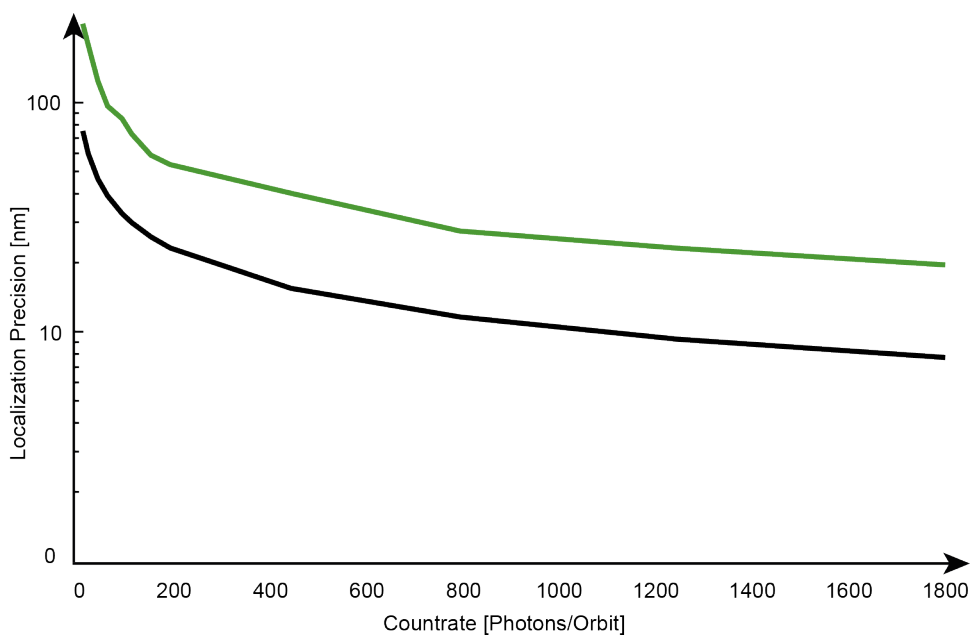


Figure 4.15 | Countrate dependent axial localization precision: Comparison between the theoretical (black) and experimental (z-axis green) count rate dependent localization precision.

diameter in the range of the point spread function and through their convolution create a significant larger spot, which emits photons. Thus, a smaller pinhole would not necessarily improve the axial localization precision (# of detected photon decreased vs. smaller axial beam waist) but significantly worsen the lateral localization precision. In addition, the z-objective piezo has a response time of $\sim 10ms$, which leads to additional inaccuracies due to the movement of the focus in the z direction while an orbit is acquired. To decrease the response time of the system along the z-direction, the objective piezo can be replaced with a deformable lens. The stability and therefore the precision will be increased due to the slightly lower response time.

Tracking Speed

To achieve a reasonable localization precision, one makes the assumption of a quasi stationary particle during a full rotation of the laser focus. In reality, the particle is moving and the fluorescent signal is expanded and covers more (particle moves along the orbit rotation) or less bins (particle moves in the opposite direction of the orbit). Depending on the particle speed, the localization accuracy can be significantly decreased. Although the tracking accuracy is diminished, the tracking algorithm will still be able to follow

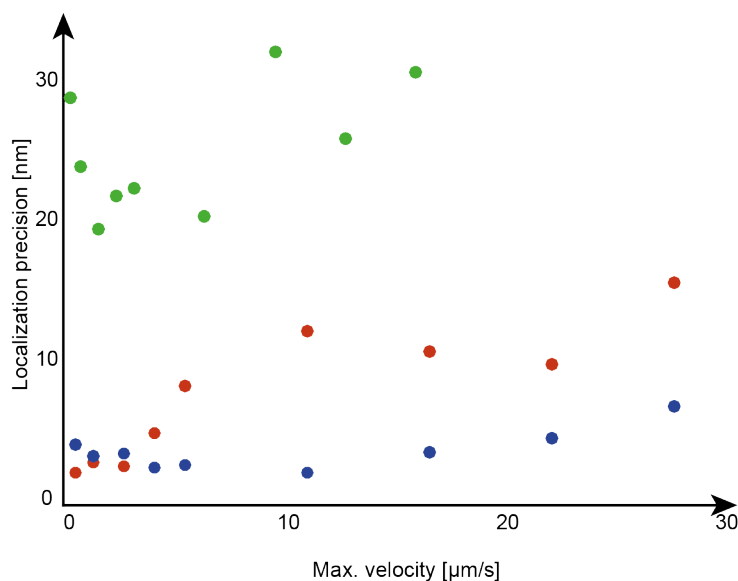


Figure 4.16 | Localization precision depends on particle speed: Localization precision values for the x-axis (red), y-axis (blue) and z-axis (green) as a function of particle velocity. The steeper rise of the x-axis is an effect of the orbit start point located on the x-axis.

such particles. The lateral velocity and diffusion constant thresholds until a particle is no longer trackable can be estimated using the following equations:

$$v_{max,xy} = \frac{d_{Orbit}}{t_{Orbit}} \quad D_{max,xy} = \frac{\langle d_{Orbit}^2 \rangle}{2nt_{Orbit}} \quad (4.22)$$

Assuming an orbit diameter of $d_{Orbit} = 520nm$, three dimensional diffusion $n = 3$ and an orbit time of $t_{Orbit} = 0.005s$ the maximum linear velocity trackable is $104\mu m/s$. The same parameters yield a maximum lateral diffusion coefficient of $9.0\mu m^2/s$. Considering the finite delay times of the galvo scanners and z-objective piezo, the velocity and diffusion threshold for particle loss are smaller and normally limited by the significantly greater delay times of the piezo. Fig. 4.16 shows the velocity dependent localization precision, which decreases for higher velocities and the maximal velocity for each axis. The maximal experimental diffusion coefficient for the above parameters was $1.7\mu m^2/s$, which corresponds to a bead with a hydrodynamic radius of $150nm$ diffusing in water at $25^\circ C$. Although the experimental threshold values are significant smaller than theory, they still exceed the requirements for live cell and in vivo experiments where cargo is transported by motor proteins or diffusing in a highly viscous environment such as the cytoplasm.

4.5 Microscope Alignment

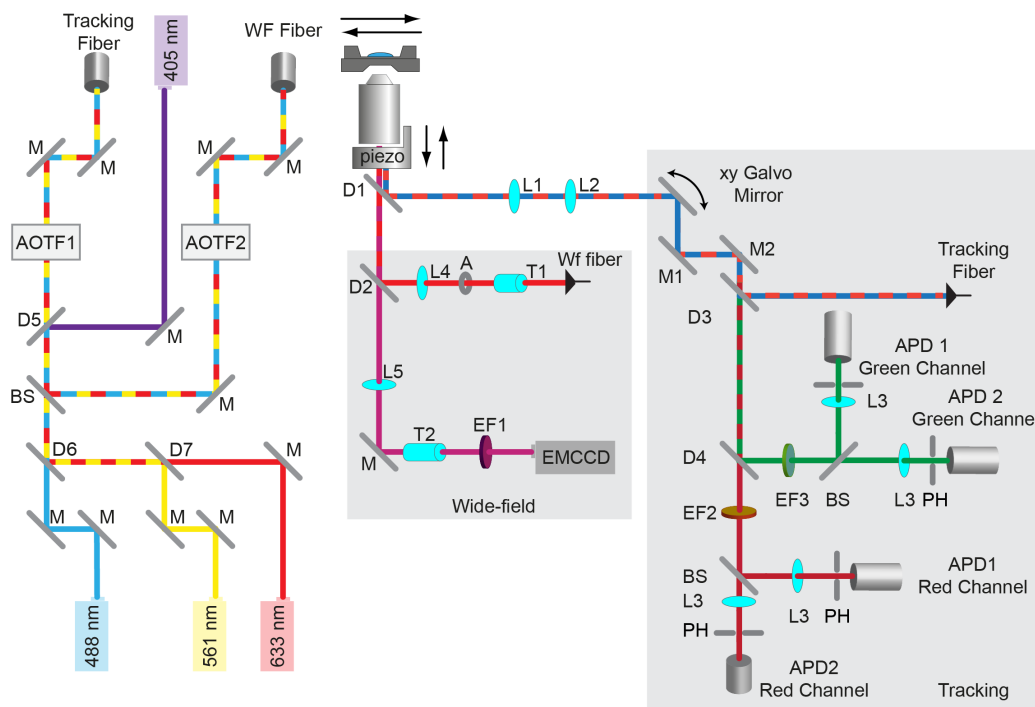


Figure 4.17 | 3D Orbital Tracking microscope schematic: D: Dichroic mirror, M: silver mirror, EF: emission filter, BS: 50/50 beam-splitter, PH: pinhole, L: lens, T: telescope, APD: avalanche photo diode

Excitation Path

The alignment of the excitation path starts with the alignment of the scanner unit. The two galvo mirrors have to be aligned in 5 dimensions (x, y, z and the rotation angles for each mirror θ_x and θ_y). Due to the design of the mirror mount, these parameters are not orthogonal to each other and the adjustment of one axis results in a change of the laser beam path, which has to be compensated with another axis. An normal iterative approach for the positioning of the two mirrors is thus not optimal. The solution is to use two laser beams, one going backwards through the microscope body and a second beam going forwards. The backwards beam is used to align the x -, y - and z -position of the galvo until the laser beam directly hits the center of the first galvo mirror. The next step is to align the rotation angles θ_x and θ_y of both galvo mirrors until the laser beam hits the second galvo mirror and the center of the first alignment mirror (M1, Fig. 4.17). The forward

and backwards laser beams are overlapped using the alignment mirror pair (M1 & M2). The backward laser is removed and the fine adjustment of the excitation laser can be performed using the alignment mirrors. The laser beam is then expanded through the installation of the tube lens (L1) and scanner lens (L2). To achieve an optimal alignment, the laser beam must only change the angle of incidence at the back aperture of the objective when the beam is deflected by the galvano mirrors. This can be achieved by connecting a sine and cosine signal to the galvano mirrors and observing the behavior of the beam spot at the back aperture. Usually the z-position of the scanner lens (L2) is not optimal in the beginning and the beam spot at the back aperture is exhibiting a circular motion. This motion can be minimized by moving the scanner lens along the optical axis to the optimal position.

Detection Path

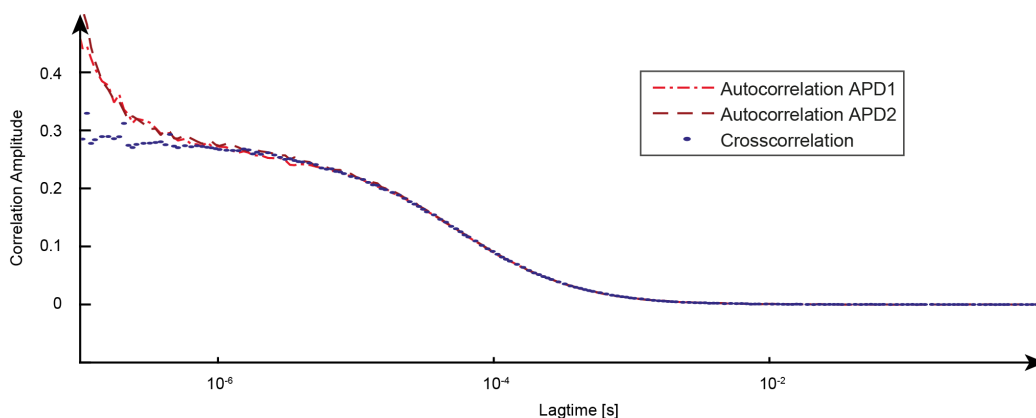


Figure 4.18 | Auto- and crosscorrelation curves used for alignment: Optimized autocorrelation (dashed red lines) and crosscorrelation (blue dots) signals from the red detector pair using a 1nM solution of atto 565.

After the excitation path, the detection path is aligned by optimizing the countrate on each detector using a 1 μM dye solution. The alignment of each detector is further refined using a hardware correlator to record the autocorrelation for each detector and the cross-correlation for each detector pair (using a 1 nM dye solution, Fig. 4.18). If the fiber position, which transmits the maximum countrate does not show an autocorrelation signal, the positions of the tube and scanner lenses are not optimal and cause a slight focusing of the laser beam that can be corrected by changing the position of the collimation lens inside RGB collimator. It has to be noted that due to optical aberrations, the excitation volumes for different colors are not located

at the same position and are slightly shifted with respect to each other. To create the two detection volumes above and below the objective focus, the fiber entrances of each detector pair are separated using the μm translation stages. The autocorrelation amplitude of each detector is maximized after each shift to account for off-axis movement of the fiber entrance. To probe the 3D positions of each detection volume, the tracking software is used to perform a line scan over a fixed diffraction limited particle. The optimal distance between the two detectors along the z direction is $\sim 200 - 250\text{nm}$. This distance is the optimal compromise between a proper channel separation, which is necessary for the tracking algorithm and the number of detected photons. Once the optimal distance has been found, linear scans along the x and y axis over a diffractions limited particle are used to overlap the lateral position of the two detection volumes. The optimal alignment for a detector pair is shown in Fig 4.19.

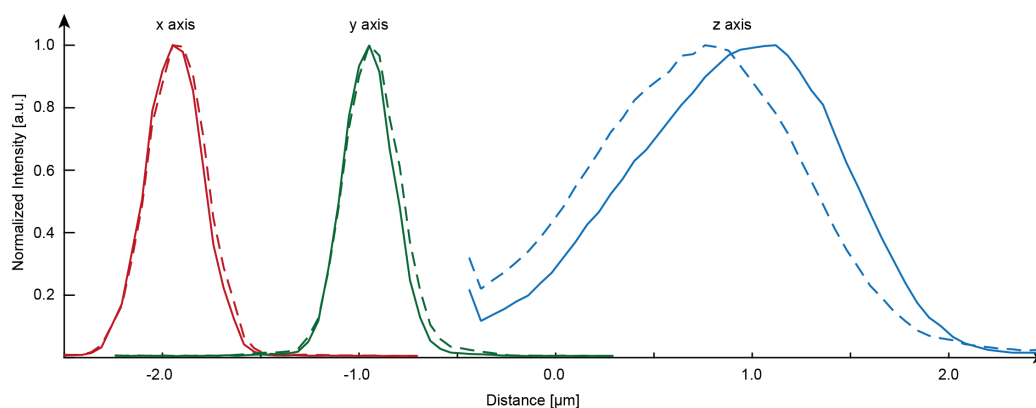


Figure 4.19 | Detector pair alignment: Optimal spatial alignment for a detector pair. Point spread function were acquired through linear scans along the x, y and z axis of a stationary particle embedded in a clear polymer using 50 equidistant points with 100ms bin time along the corresponding axis.

Widefield Microscope

The wide-field microscope is aligned through a standard alignment procedure for Köhler Illumination [25]. The collimated beam from the single-mode fiber for the wide-field microscope is expanded using a telescope (T1) with a 3 fold magnification. A square aperture (A) transmits only the mostly homogeneous tip of the Gaussian excitation profile. Another lens (L4) focuses the collimated beam on the back aperture of the objective to generate again a collimated beam after the objective. After the alignment of the excitation is completed, the image plane of the camera has to be coupled to the focal

plane of the objective. A raw alignment is achieved through imaging a "USAF Resolution Test Chart" and the translation of the tube lens (L5) along the optical axis. This raw alignment is then refined by using a test sample containing multifluorescent beads inside a polymer matrix.

Chapter 5

Correlation Analysis

5.1 Introduction

Regardless of the chosen single particle tracking approach, the resulting data set always consists of coordinates, which represent the position of the particle at any given point in time. This dataset is usually biased through the method dependent localization noise, a combination of photon shot-noise and other influences, which are inherent to the different particle tracking techniques. Other factors include temperature dependent drift of the microscope system and mechanical oscillations.

The main challenge when analyzing particle tracking data is to discriminate between active and passive motion in the presence of localization noise, which for high acquisition rates can have the same magnitude as the particle displacement per localization step. A very common analysis method is the mean squared displacement (MSD) analysis, which is derived from Albert Einstein's theoretical paper from 1905 [71]. Particle motion can be classified into Brownian diffusion, active transport, subdiffusion and confined diffusion through an analysis of the MSD (Figure 5.1). For data sets containing several thousand data points, the MSD approach is a powerful tool to determine the overall properties of the whole ensemble. However, several practical hurdles exist when using the MSD approach to determine local variances in the data set. The first problem arises from the algorithm, which calculates the MSD curve. For a finite time interval $[t, t + t_{max}]$ containing n time points, each data value in the MSD curve is calculated using $n - \tau_i$ (i denotes time indexing) data points from the trajectory data. This statistical reduction along the MSD curve leads to the recommendation to limit the analysis to $\frac{1}{8}$ to $\frac{1}{4}$ of the total data points [72]. Depending on the analysis window size, noise can

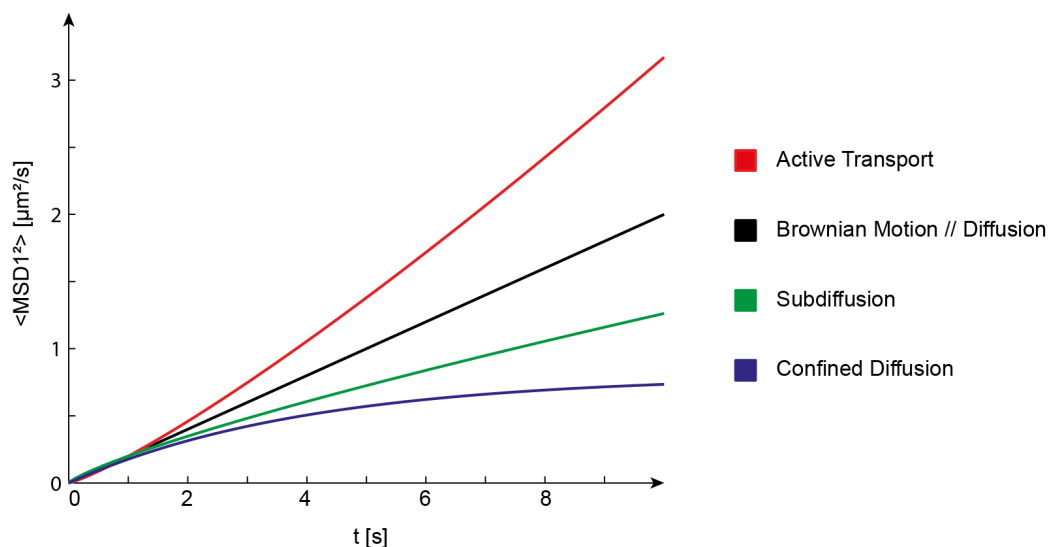


Figure 5.1 | Mean squared displacements of different motion types: MSD plots of active transport (red), brownian motion (black), subdiffusion (green) and confined diffusion (blue).

significantly contribute to the curve calculation and impact the data quality.

The second issue is related to the classification of the different transport processes (Fig. 5.1). As mentioned above, MSD calculation can be significantly influenced by the signal-to-noise (S/N) ratio of the trajectory data. Local MSD curves can be fitted to the following equation:

$$\langle MSD^2 \rangle = 2nDt^\alpha \quad (5.1)$$

where n the number of dimensions, D denotes the diffusion coefficient, t the time and lastly α , which is an indicator for the type of transport. The quality of the fitting process is directly related to the number of data points and, for data sets containing only a few data points, the above variables show a significant variance. Usually the α coefficient is used to classify motion into transport, diffusion and subdiffusion. Due to the variance of this variable, no universal threshold can be used or derived from the experimental data. In the end, all used thresholds are based on assumptions, which are made prior to the experiment or during the analysis process and thus, these thresholds are very susceptible to misinterpretations.

The last complication is related to the calculation time of MSD approaches.

The calculation of such curves is computational not very expensive, but each data point requires a fitting step to classify the data. Although the fitting speed can be increased by using a linear model:

$$\log(\langle MSD^2 \rangle) = \alpha \log(t) + \log(2nD) \quad (5.2)$$

each data point requires a significant amount of time, which becomes unhandy for trajectories containing tens of thousands of data points (a number that is easily achieved with modern methods such as 3D orbital tracking).

These difficulties made it necessary to develop an analysis algorithm providing the following features:

- Improved computational efficiency to reduce analysis time
- Small analysis window to probe for local changes in the particle behavior
- User independent threshold levels derived directly from the trajectory data

5.2 2-dimensional Correlation Analysis

For the study of intracellular dynamics, the recorded trajectory data needs to be separated into phases of active transport and passive states. During active transport, motor proteins relocate the particle along the cytoskeleton of the cell and thus, the trajectory data is a convolution of transport, diffusion and the method dependent noise. During passive states, the particle undergoes confined diffusion due to the highly crowded and viscous environment inside the cell. The trajectory data in these time intervals is a convolution of the method dependent noise, and the subdiffusive motion of the particle.

These two populations can be separated using a correlative approach. For active transport, the lateral angle ϕ and axial angle θ will show a directional bias between two consecutive localizations, which is not the case for passive states. The magnitude of this directional bias depends on the 3D orientation of the underlying cytoskeleton. Eq. 5.3 describes the calculation of a correlation carpet $Cor(t, \tau)$ along a two dimensional trajectory using a sliding correlation window:

$$Cor(t, \tau) = \frac{1}{n - \tau} \sum_t^{t+\tau_{max}-\tau} (\phi_t)(\phi_{t-\tau}) \quad (5.3)$$

where τ denotes the correlation lag time, τ_{max} the correlation window size and ϕ the lateral angle between two consecutive localizations. Eq. 5.3 can be calculated using the Wiener-Khinchin theorem, which calculates correlation amplitudes through a combination of fast Fourier Transformations (FFT) and it's inverse counterpart (iFFT) [73]. Unlike fitting a model to a set of data points, this approach requires no iterative steps and thus significantly increases the calculation speed. To account for the size of the correlation window, the data points are shifted by half the correlation window size. Figure 5.2 shows the correlation carpet for pure diffusion and active transport (including localization noise). As the variance in correlation amplitudes depends on the signal-to-noise ratio, it is necessary to derive a threshold level to separate between active and passive phases. Unlike thresholds for MSD calculations, correlation thresholds can be derived directly from the trajectory data. In a first step, the angle ϕ is randomized and the resulting array is expanded by its negative values to remove any directionality, which may be included in the trajectory data. The randomized array is then analyzed with Eq. 5.3 to calculate the corresponding correlation amplitude. The average value of this amplitude plus the standard deviation multiplied with a threshold factor can then be used for all trajectories from a specific specimen.

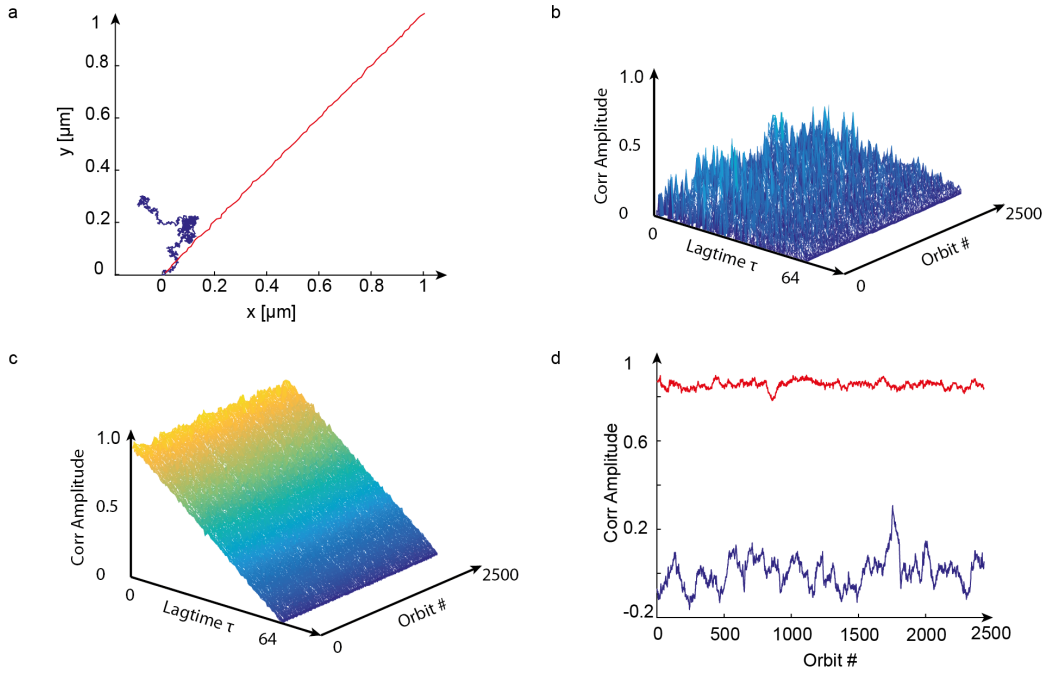


Figure 5.2 | Correlation amplitudes of active transport and diffusion: a) Simulated trajectory of a particle undergoing Brownian motion (blue) and active transport (red). b,c) Correlation carpets calculated using Eq. 5.3. The correlation amplitudes differ significantly between Brownian motion b) and active transport c). For convenience, the correlation carpets are reduced to two dimensions by calculating the average along the lag time interval $[0.05\tau_{max}, 0.10\tau_{max}]$. The correlation amplitude for transport (red) is close to unity whereas the amplitude for diffusion is oscillating around 0 (blue).

Correlation amplitude values above the threshold level are classified as active and values below as passive. To test for optimal parameters regarding window size and threshold level for each type of experiment, several simulations have to be performed.

Influence of Correlation Parameters

To determine the effects of different correlation window sizes and threshold factors, several simulations were performed using the following assumptions:

- The simulation should represent particle transport inside a cell.
- Localization precision is constant and independent of the spatiotemporal coordinates.
- Passive phases represent particles, which are not actively transported by motor proteins.
- Diffusion of particles is negligible over the pause duration for passive phases due to the viscosity of the intracellular medium and the size of the tracked particle.
- The length distribution of passive and active phases follow an exponential distribution.
- The orientation of the cytoskeleton is not obstructed laterally, but is restricted in the third dimension to account for the comparable smaller size of a cell in the z direction.

Fig. 5.3 a) shows a trajectory, which was simulated using the above assumptions. To study the influence of the signal-to-noise ratio (orbit displacement during active phases divided by the standard deviation of the localization noise) on the recovery rate along the trajectory, each trajectory was analyzed using different window sizes (16, 32, 64 and 128 points) and threshold values (sigma ranging between 1 and 5 in 0.5 intervals). With an increasing signal-to-noise ratio, the overall recovery rate (defined as the percentage of data points correctly identified by the algorithm) approached values around 95% (Fig. 5.3 b). Due to the design of the correlation algorithm, which searches for active phases within the trajectory, the recovery rate of passive phases was constant for all S/N values and showed nearly perfect recovery (> 99%). The active phase recovery was strongly influenced by the S/N ratio. Trajectories containing a significant amount of noise ($S/N \sim 1$) showed a decreased recovery rate ($\sim 80\%$). For these trajectories, the optimal window size (128 points) was higher than for trajectories containing less noise (64/32 points, Fig. 5.3 c). The increased correlation window size "smoothes" the trajectory data and reduces the influence of noise and thus produces more accurate results. However in cases where trajectories contain a great number of very short pauses, longer correlation windows will average out the presence of these short pauses and thus decrease the algorithm accuracy.

Correlation Analysis

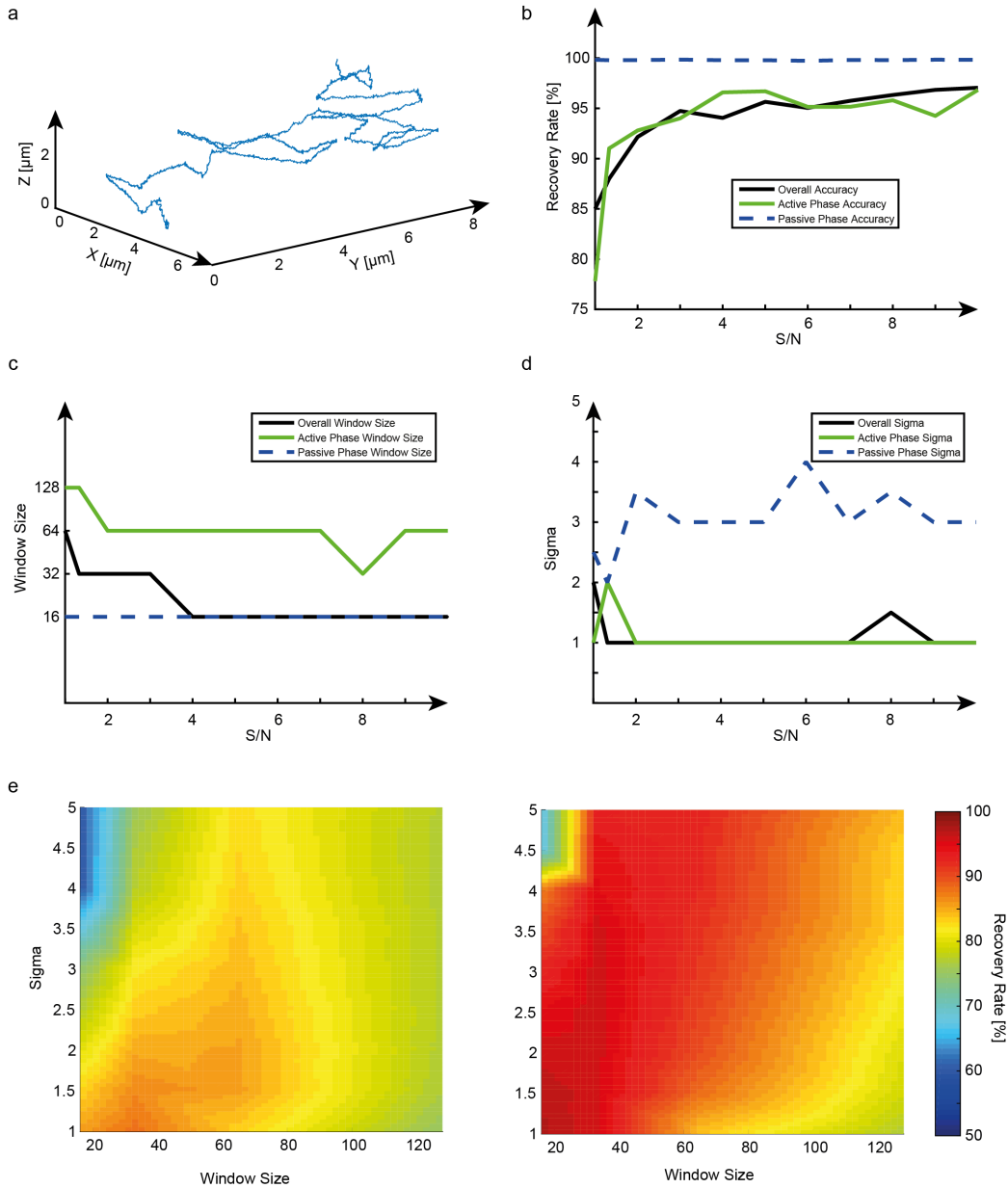


Figure 5.3 | Simulated recovery rates for the 2D correlation analysis: a) Simulated trajectory containing 12549 data points and 40 active and passive phases. b) Recovery rate for varying S/N ratios. c,d) Optimal values of correlation window size and σ for varying S/N ratios. e) Recovery values for different window sizes and σ values. Left panel: S/N = 2, Right panel: S/N=10.

The σ values for optimal recovery for active and passive phases were constant for S/N ratios greater than one (Fig. 5.3 d). Passive detection was optimal for σ values > 3 whereas active recovery was optimal for small σ values. This behavior is explained by the fact that high threshold levels prevent the wrong assignment of passive localizations into active ones and vice versa. Fig. 5.3 e) shows the interpolated recovery values for all combinations of correlation window size and σ for S/N values of 2 (left panel) and 10 (right panel). For small S/N values, the recovery carpet varies significantly and shows distinct optimal settings for a maximum recovery rate of approximately 85%. Recovery carpets from trajectories with a significant better S/N ratio, show a more uniform distribution of recovery rates (right panel).

Since the accuracy of the autocorrelation approach significantly depends on the signal-to-noise ratio, the experimental settings have to be adjusted if the S/N ratio is smaller than one. Smaller acquisition speeds lead to a noise reduction due to an increased number of photons detected during the acquisition period. Reducing the acquisition speed by a factor of R leads to a noise reduction of \sqrt{R} . In addition, the decreased acquisition speed increases the signal (transport along the cytoskeleton) by the same factor, which leads to a total increase of the S/N ratio by a factor of $R\sqrt{R}$.

5.3 3-dimensional Correlation Analysis

Until now, only the lateral angle ϕ was used to discriminate between active and passive states within a single trajectory. Most specimen exhibit 3 dimensional motion, which cannot be described using only a lateral correlation approach. The 2-dimensional correlation analysis can be expanded by applying Eq. 5.3 to the remaining angle along the z-axis, θ . The correlation amplitude of ϕ covers lateral motion and the amplitude of θ covers axial motion. The output arrays of both angles are then connected via a logical "or" operator to combine the 1D and 2D informations to an array which contains the full 3D information of the algorithm.

To determine the recovery gain, which can be achieved through the combination of the two correlation amplitudes, the simulation was modified. To maximize the influence of motion along the z-axis, the axial obstruction for the cytoskeleton was removed, all other simulation parameters were unchanged. This modification of the simulation algorithm generates trajectories that show a uniform distribution of active phase directions in 3 dimensions (Fig. 5.4 a). When comparing the recovery rate for θ , ϕ and their combination by using a binary pattern, only the combination of both angles is able to recover most of the input data (Fig. 5.4 b). Several simulations with different S/N ratios were performed to determine the recovery gain of the 3D-dimensional approach compared to the 2-dimensional approach. Depending on the overall S/N ratio of the trajectory, the addition of the second angle to the analysis significantly improves the recovery rate, especially for low lateral S/N ratios and can exceed 95% (Fig. 5.4 c, left panels). The same behavior is observable for the average recovery rates for all simulated parameter combinations (Fig. 5.4 c, right panels).

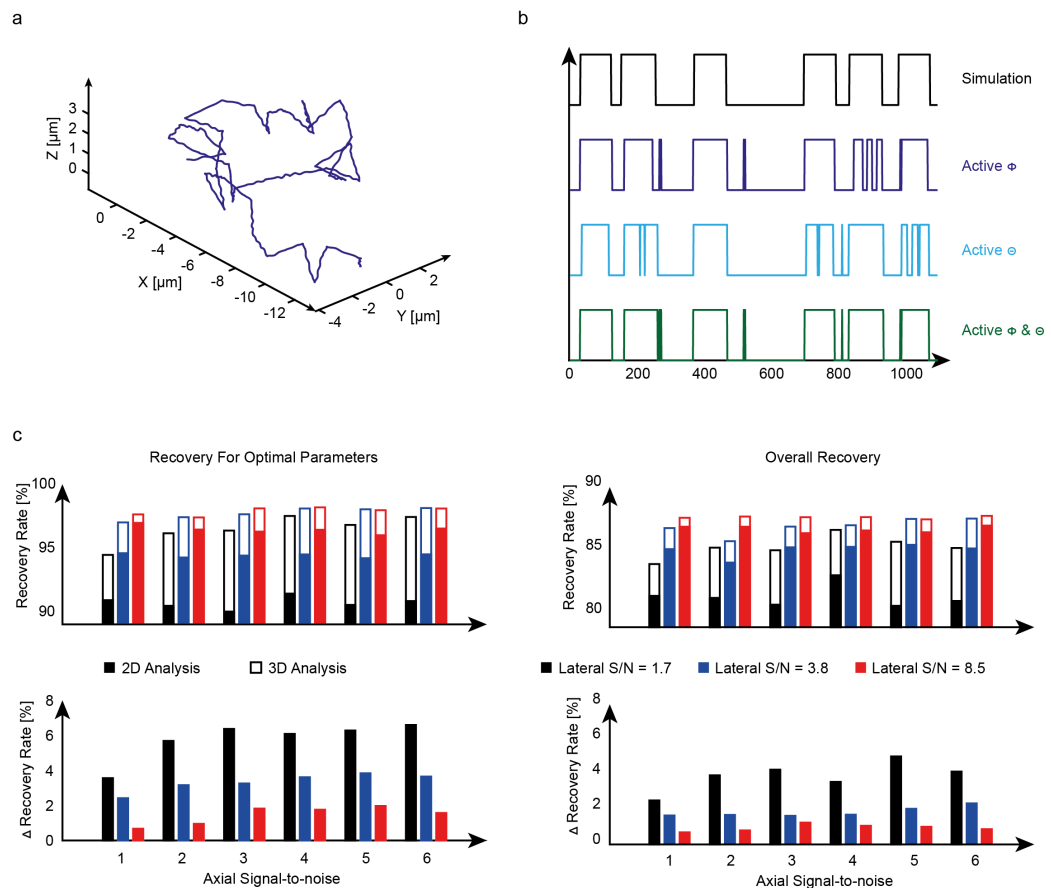


Figure 5.4 | Simulated recovery rates for the 3D correlation analysis: a) Simulated trajectory again, moving unobstructed along the z-axis. Trajectory contains 11945 data points and 40 active and passive phases. b) Binary pattern showing active (1) and passive (0) phases along the trajectory. The generated binary patterns for the angle ϕ (dark blue) and θ (light blue) are individually not able to recover all active states from the simulated data (black). The combination of ϕ and θ achieves a nearly perfect reconstruction of the simulated data (green). c) Recovery rates for optimal parameters (left panels), mean recovery rates of all examined parameter combinations (right panels) for varying lateral S/N ratios. Filled bars represent recovery rates for the 2D algorithm, empty bars rates for the 3D algorithm. Bottom panels show the recovery gain by using the combination of ϕ and θ .

5.4 Correlation Parameter Determination For Mitochondrial Trafficking

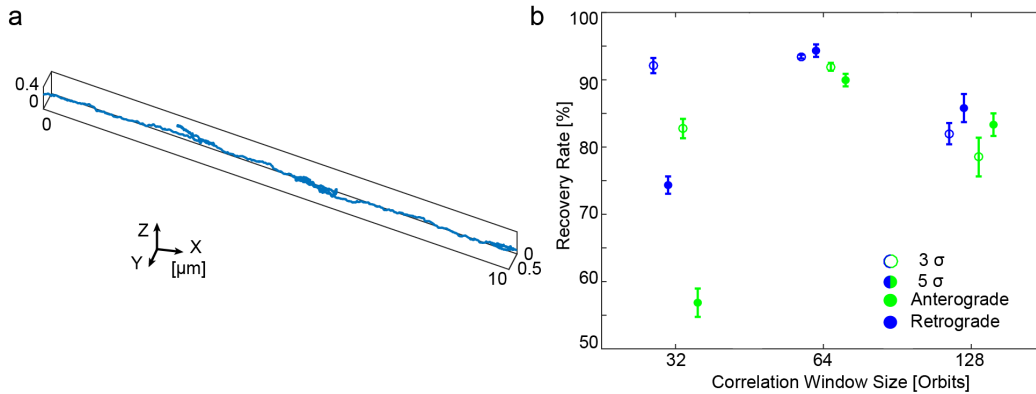


Figure 5.5 | Parameter determination for the analysis of mitochondrial transport: a) Simulated trajectory containing 8921 data points of mitochondrial transport in a Rohon-beard sensory neuron. See chapter 7 for details. b) Recovery rates of several combinations of correlation window size and correlation thresholds. Standard deviations of five individual simulations per data point are shown.

The presented correlation analysis was used to analyze mitochondrial trafficking in rohon-beard sensory neurons described in chapter 7. As the axonal structure of rohon-beard sensory neurons does not show a prominent elongation along the z-axis, only the 2-dimensional correlation approach was applied to extract active and passive phases of motion. The optimal parameters were determined through several steps. First, the experimental trajectory data was analyzed using a correlation window size of 128 points and a threshold value of 3σ . This analysis revealed the parameters, which were used to simulate a trajectory showing the same behavior as the obtained data:

- S/N ratio
- Distributions from the duration of the 5 motion types present in both antero- and retrograde transport
- Transport Velocities for slow and fast motion
- Transition probabilities between active-passive-active transitions

Fig. 5.5 a) shows the simulated trajectory of mitochondrial transport along the stem axon of a sensory neuron. Different combinations of parameters

were tested for their individual recovery rates in the antero- and retrograde direction (Fig. 5.5 b). The highest average recovery rate of 92.14% was obtained for the combination of 64 data points as correlation window size and 5σ as threshold value. As shown in Fig. 5.3, a correlation window size of 64 data points is the optimal parameter for low S/N ratios (1-1.5 for the experiments, see Fig. 7.6 c) for comparison). Due to the long pause length (comparable to the duration of active phases), which will increase the average correlation amplitude for the randomized data set, the threshold level of 5σ is the optimal compromise between detecting pauses and active phases.

5.5 Discussion & Outlook

The presented correlation approach for the analysis of single particle tracking experiments offers several advantages over the standard mean squared displacement approach. First, the analysis algorithm does not decrease the statistics for higher lagtimes τ and thus smaller analysis windows can be chosen without affecting the quality of data. This allows a more precise analysis of short-term events, which can be present in the trajectory data. Second, the correlation approach is insensitive to localization noise due to the inherent property of noise, which does not correlate. This allows for very high recovery rates of $\sim 90\%$ for the 2D and $\sim 95\%$ for the 3D approach for low S/N ratios (1-2, Fig. 5.3 & 5.4). Third, the correlation analysis does not require any fitting routines and calculates the correlation amplitude values using the Fast Fourier Transformation algorithm [73]. For large amounts of data, which are collected with modern single particle tracking microscopes, the calculation time becomes a significant factor and can be decreased using the correlation approach.

The presented algorithm is not able to discriminate between Brownian motion and pauses caused by particles temporarily attached to the cytoskeleton. Since the angle between two consecutive orbits does not offer any information about the magnitude of displacement per orbit, the algorithm cannot discriminate between localization noise due to photon statistics or Brownian motion. For specimens that exhibit these types of "motion", additional steps have to be implemented into the analysis, such as analyzing the orbit displacement histograms for passive phases or algorithms, which measure the traveled distance during a certain time interval.

The second drawback is the current need for simulations to determine the best parameters for the analysis. This time consuming process can be removed if the algorithm is expanded with an iterative routine, which optimizes the parameters without any user interaction. Optimization criteria for this process could include the displacement per orbit or travel distance of active transport, which will converge upon reaching the optimal settings for the analysis.

Chapter 6

Lysosome Trafficking In Monkey Kidney Cells (BSC-1)

6.1 Introduction

Intracellular transport of vesicles and organelles plays a critical role in maintaining cell health. Cellular cargo is transported along the microtubule network by motor proteins such as kinesin and dynein [74,75]. A mis-regulation of this highly controlled process can impair the intracellular transport and is linked to several diseases such as cystic fibrosis, diabetes, Alzheimer disease and many more [76,77]. The regulation of intracellular transport is achieved through different mechanisms such as motor protein clustering, scaffolding proteins and the cytoskeleton itself [78–83]. The least well-understood mechanism is the regulation of transport by the local cytoskeleton. This can be attributed to the experimental challenge of imaging a three dimensional structure on the nanometer scale and simultaneously recording the trajectory of cargo being transported along the cytoskeleton. Recent developments in the group of Prof. Lakadamyali at the ICFO Institute in Barcelona have led to the development of a correlative imaging approach combining astigmatism based single-particle tracking and three dimensional stochastic optical reconstruction microscopy (STORM) [84–86]. They showed that the pausing of endolysosomal vesicles on microtubules correlates with intersections with a spacing of less than 100nm [84]. Since pausing events in healthy cells are mostly temporary and vesicles are cleared from intersections in short time periods [84], molecular motors are able to circumvent such obstacles. However, the underlying mechanism remains unclear.

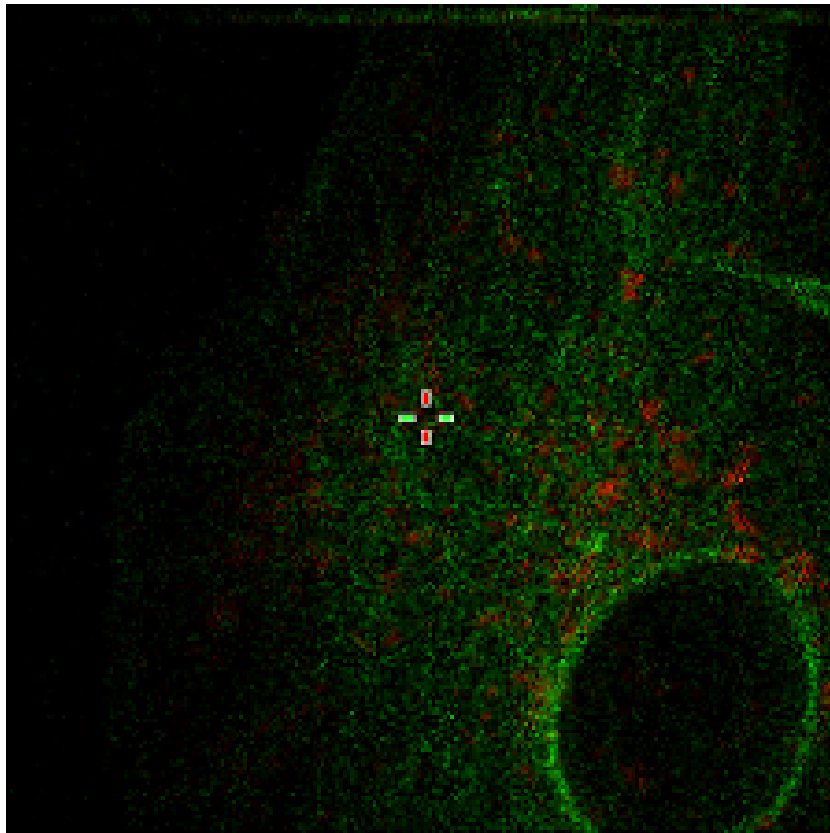


Figure 6.1 | Dual color image of a BSC-1 cell: The cell is stably expressing GFP-Tubulin (green) and Lamp2-mCherry (red). Confocal scan was acquired using 488 nm and 561 nm excitation and scanning a region of interest ($35\mu\text{m}^2$, 256×256 pixels) within two seconds.

To elucidate this mechanism, further experiments have been performed in collaboration with Ione Verdeni-Vilanova from the group of Prof. Lakadamyali. Ione Verdeni-Vilanova performed correlative imaging experiments and their analysis. Orbital Tracking experiments were carried out together and I analyzed the tracking data. The experiments were performed in a BSC-1 cell lines stably expressing GFP-Tubulin or GFP-Tubulin and Lamp2-mCherry (Fig. 6.1, for details see Materials and Methods, section 10.3). To investigate the behavior of cargo at microtubule intersections, several experimental conditions have to be met. First, the z resolution of the tracking approach has to be sufficient to resolve changes along the optical axis on the order of a few dozen nanometers. This requirement is exceeded by both the 3D orbital tracking and the correlative imaging approach. Second, the tracking experiment has to be able to track particles with an undefined and fluctu-

ating shape. Since the the astigmatism based tracking approach is not able to localize such particles, 260 nm or 450 nm microspheres were internalized into lysosomes and served as probes for lysosomal motion. To confirm that internalization of these microspheres does not influence their transport behavior, additional tracking experiments on lysosomes were performed using the orbital tracking approach, which is not affected by the particle shape. Third, the motion of the lysosome needs to be aligned with the underlying cytoskeleton, which currently can only be achieved by the correlative imaging approach. To ensure that the cytoskeleton is not fluctuating on the timescale of the tracking experiment and thus introducing a bias on the localization precision, real-time super-resolution measurements of the microtubule structure were performed using an alternative tracking mode of the orbital tracking microscope.

With the combination of these two experimental methods, several new insight regarding the transport behavior at intersections could be gained. To investigate if large particles can pass intersections through deformation, 450 nm microspheres were internalized into lysosomes. The comparison of the motion of these rigid objects with normal transport showed no significant changes, suggesting that membrane deformation does not improve the ability of vesicles to overcome sterical obstacles.

Further analysis of vesicle trajectories revealed two different types of motion, which could be detected in both tracking approaches. The first motion type is moving in a linear fashion along the microtubule network. The second motion type exhibits a helical motion around microtubule strands. The two motion types were classified as Mode I and Mode II motion. Mode I motion exhibited z-changes smaller than 40 nm, whereas Mode II motion showed off-axis motion along microtubules with an average change of 73 ± 42 nm along the z axis. Mode I and II motion showed no preferred direction of motion (anterograde vs. retrograde direction), happened on the same segments of microtubules and could be observed on tyrosinated and detyrosinated microtubules. These results support the idea that the transport does not depend on the underlying microtubule structure. When comparing the transport properties of the two Modes of motion, Mode I showed shorter run lengths than the part of microtubule on which they occurred. Run length of Mode II motion was comparable to segment size and significantly longer than Mode I motion ($1.0 \pm 0.5 \mu m$ vs. $0.3 \pm 0.4 \mu m$). Interruption by passive phases were slightly longer for Mode II motion (18 ± 23 s vs. 12 ± 13 s) but were more frequent for Mode I motion. These results suggest, that Mode II motion is a more efficient way to navigate the microtubule network.

The off-axis motion exhibited by Mode II motion enabled vesicles to overcome obstacles (such as other vesicles moving in the opposite direction, intersection) more efficiently. Lysosomes, which showed a passive phase prior to the crossing of an intersection were more likely to engage Mode II motion than particles that did not pause at intersections (59% vs. 32%). However, not all particles that paused at intersections showed no displacement in any direction, suggesting that vesicles can actively change the separation distance between microtubules.

The experiments, which were performed using the 3D orbital tracking technique are explained in details in the following sections.

6.2 Microtubule Tracking

In addition to single-particle tracking, 3D orbital tracking can be used to determine the 3D position of an elongated structure, e.g. microtubules, with nanoscale precision [66]. The active control of the tracking algorithm to move the laser focus along the one dimensional fiber requires further modification of the tracking algorithm. An easier solution to measure the structure of a one dimensional fiber, e.g. microtubules in the cytoskeleton, utilizes the process of photobleaching. As the tracking algorithm always tries to minimize the modulation of the signal in all three dimensions, the laser focus will move along the changing intensity signal. After starting the tracking algorithm, the orbit will bleach the fluorophores on the microtubule and the orbit will follow the path of the 3D elongated structure (Fig. 6.2 a,b). Depending on the fluorescence intensity along the microtubule, the orbital laser can occasionally reverse direction, which allows imaging of the same section of the microtubule over time (Fig. 6.2 c,d). The velocity of this movement is solely dependent on the laser intensity and photostability of the fluorophore and is not actively regulated by the algorithm.

To study the magnitude of microtubule fluctuations, which could decrease the localization precision of the correlative imaging approach, individual microtubules were tracked using the 3D orbital tracking microscope, effectively reconstructing their three dimensional shape (Fig. 6.2 e). The magnitude of fluctuations was derived from the fluctuation ratio, which is defined as the quotient between the standard deviation of a linearized trajectory and the countrate dependent localization precision of the respective axis. Untreated cells showed fluctuations on the order of 30 nm (localization precision: ~ 5 nm in xy, ~ 40 nm in z, indicated by fluctuation ratios of 4.26 ± 1.73 lateral and 1.59 ± 0.47 axial). Cells treated with a combination of 120 nM paclitaxel and 120nM nocodazole (used in the correlative imaging approach for stabilizing the cytoskeleton over the course of the experiment [84]) showed smaller fluctuations (fluctuation ratios 2.43 ± 0.51 lateral and 1.42 ± 0.14 axial, Fig. 6.2 f). These results confirm that the microtubule fluctuations in drug-treated BSC-1 cells are smaller than the localization precision of the correlative imaging approach (lateral localization precision 10 nm, axial localization precision 20 nm) and the derived distances between lysosome and microtubule represent accurate values.

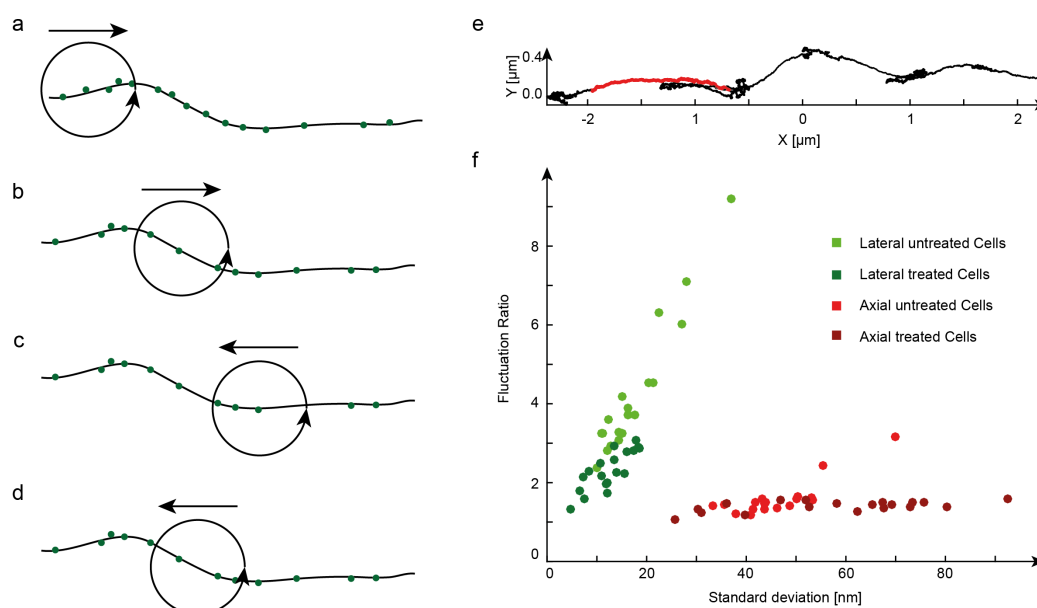


Figure 6.2 | Microtubule tracking: a-d) Schematic representation of a microtubule (black) labeled with GFP (green) and the laser orbit (black, not to scale). In the beginning, the tracking algorithm will be localized at one location until photobleaching causes a significant reduction of the local fluorescent signal and the algorithm starts to move along the microtubule (b). If the laser orbit reaches a location with a smaller fluorescent signal, the orbit stops (c) and after bleaching of more GFP molecules moves backwards (d). e) Microtubule trajectory acquired with 200 Hz containing 19000 data points. The trajectory consists of linear segments on which the tracking algorithm is propelled along the microtubule through photo-bleaching. Between -0.5 and $-1.5 \mu\text{m}$ along the x axis, the tracking algorithm changed direction and probed the same microtubule segment several times. The amplitudes of microtubule fluctuations were measured along linear segments, which were extracted manually from the trajectory (red). f) Fluctuation ratios measured along the z-axis and perpendicular to the microtubule strand. The fluctuation ratio is defined as the standard deviation of a smoothed trajectory divided by the countrate dependant localization precision of the respective axis. Values close to one indicate microtubule fluctuations smaller than the localization precision. The fluctuation ratios in lateral and axial direction for untreated cells (light green and red) show fluctuation ratios higher than one indicating microtubule fluctuations on the order of $\sim 30\text{nm}$. Upon treatment with a combination of 120 nM paclitaxel and 120 nM nocodazole, the fluctuations were decreased below the resolution precision of the tracking microscope.

6.3 Lysosome Tracking

To further confirm the two motion types we found using the correlative imaging approach, lysosome motion was measured using 3D orbital tracking. Since the orbital tracking approach is not influenced by the shape of the tracked particle, the tracking algorithm only utilizes the first and second harmonic frequencies from the orbit, whereas the shape of the particle is encoded in higher order frequencies, it was not necessary to internalize microspheres inside the lysosomes. To achieve coherent results, BSC-1 cells were treated with the same combination of paclitaxel and nocodazole. Fig. 6.3 a) shows the recorded trajectory data from several lysosomes inside a single BSC-1 cell. As the bleaching rate determines how long individual particles

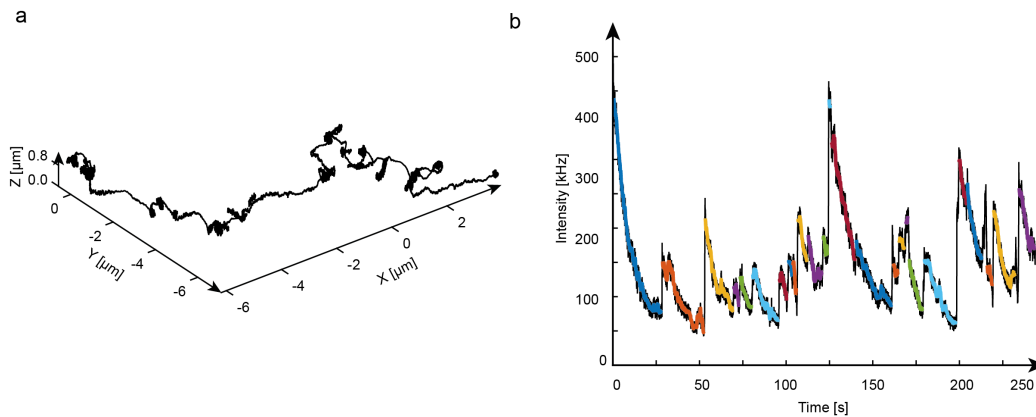


Figure 6.3 | Lysosome tracking: a) Due to the inability of the tracking algorithm to discriminate between particles, the recorded data contains the individual trajectories of several lysosomes. Data was acquired with 200 Hz over the course of 250 seconds. The trajectory can be separated using the recorded intensity data. By calculating the differential between subsequent steps, the mean intensity loss due to bleaching per orbit can be calculated (b). Bleaching steps exceeding a threshold value of the mean plus five σ are used to determine transition between particles (color coding represents individual particles). To remove localization artifacts during the transition process between particles, 0.5 seconds at the beginning and end of each trajectory were removed.

can be tracked, the same property can be used to split the trajectory data into subtrajectories, which only contain the localization data of single particles. First, the derivative of the intensity signal (Fig. 6.3 b) is calculated. Bleaching steps that exceed the average plus five times the standard deviation indicate a particle transition. To remove any localization bias, which

occurs during the transition between particles, 0.5 seconds are removed the beginning and end of each subtrajectory.

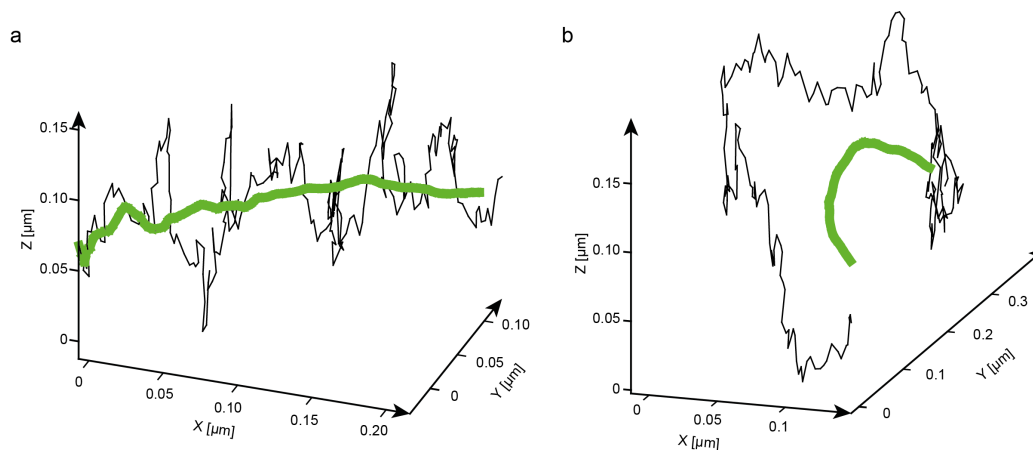


Figure 6.4 | Mode I & II motion: To discriminate between Mode I (a) & Mode II (b) motion, the raw trajectory data (black) was smoothed using a window size of two seconds, which efficiently removes the frequency components of the localization noise and the motion of the particle from the underlying cytoskeleton (green). In the case of Mode I motion (a), the filtered and raw trajectory data perfectly overlap. In reality, an offset due to the lysosome size exist between particle and microtubule position, which can not be derived from the data. In case of Mode II motion (b), the filtered trajectory data is located inside the helical shape of the raw trajectory data. The helical motion around the microtubule along with the changes in z direction is a clear indicator for Mode II motion.

Using the *a priori* knowledge of different motion types present in lysosomal transport, the 3D orbital tracking data was screened for similar movement behaviors. Although the trajectory data acquired with the orbital tracking method is a convolution of the cytoskeleton structure and the particle transport, it is still possible to approximate the shape of the underlying cytoskeleton. When converting the motion of particles into the spatial frequency domain, several different frequency regions contribute to the trajectory data. First, the count-rate dependent localization noise occurs around the frequency of localization. In the case of the orbital tracking approach, this frequency is centered around 200 Hz. The second component is the actual motion of the particle along the cytoskeleton. Mode I motion is moving linear along the microtubule and hence, it does not exhibit a dominant frequency component. Mode II motion is able to perform off-axis motion and rotates

the cargo in a helical pattern around the microtubule. With an average speed of $\sim 0.5 \mu\text{m}/\text{s}$ and an acquisition rate of 200 Hz, helical motion results in frequencies around ~ 1 Hz. The last component, the underlying cytoskeleton structure, can also be described with spatial frequencies. Microtubules show a persistence length on the order of several dozen microns [87]. Together with an acquisition rate of 200Hz and the average speed of cargo transported along the microtubule ($\sim 0.5\mu\text{m}/\text{s}$), the spatial frequencies of the cytoskeleton are located in regions smaller than 0.1 Hz. To extract the structure of the cytoskeleton from the raw trajectory data a lowpass filter is applied (in praxis the trajectory data is smoothed over a duration of 2 seconds), which removes the contributions of the localization noise and the particle motion from the trajectory data. By comparing the original trajectory with its lowpass filtered counterpart, the type of motion becomes apparent (Fig. 6.4 a,b).

In addition to the motion types present in cellular transport, the behavior of cargo at microtubule intersections is also of particular interest. Particle transitions between microtubules at intersections require the synchronized reshuffling of motors from the old to the new microtubule. Upon examination, transition events between microtubule (indicated by sharp bends in the trajectory data) show a significant displacement along the z-axis, which was observed in both tracking approaches.

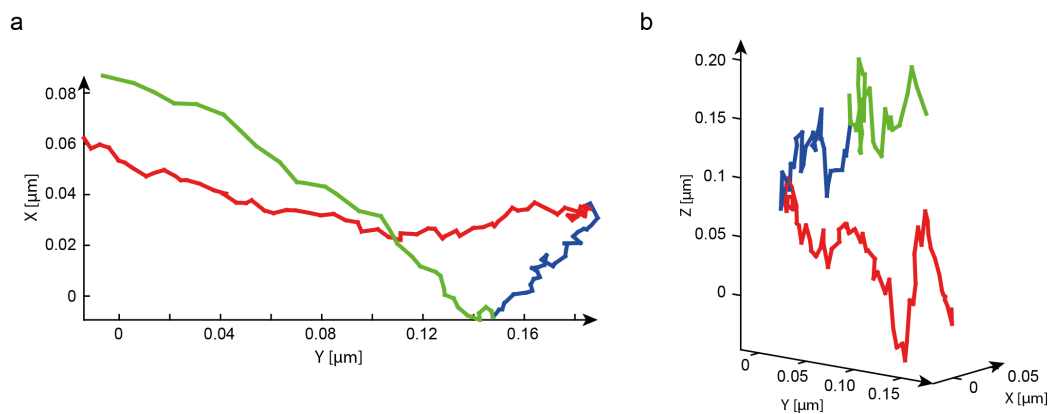


Figure 6.5 | Cargo behavior at microtubule intersections: a) An xy projection of a particle transported along three different microtubules (green, red and blue). b) A three dimensional projection of the trajectory shown in a). Significant z-changes occur whenever the particle transport switches between microtubules (red-blue: 67nm, blue-green: 52nm)

Figure 6.5 a) shows the xy projection of a particle transported along three different microtubule strands. During the transitions, z displacements of 67 and 52 nm occurred (Fig. 6.5 b). Similar results showing displacements of ~ 75 nm were obtained using the correlative imaging approach. The displacements along the z-axis of >40 nm are associated with Mode II motion.

6.4 Discussion & Outlook

The combination of 3D orbital tracking microscopy and correlative imaging provides new insights into cellular transport with nanometer precision. Two different types of motion, Mode I and Mode II could be identified. Mode I exhibits linear motion along microtubule filaments whereas Mode II exhibits off-axis motion, which results in a helical trajectory around the microtubule. The motor composition for Mode I and Mode II behavior and the underlying mechanism that determines the type of motion in the context of the local cellular structure remain unclear. It is known that certain motors are able to exhibit off-axis motion along microtubule filaments. These include dynein [88, 89] in the retrograde direction as well as kinesin-1 [90] and kinesin-2 [91] motors in the anterograde direction. However, it remains elusive if motors can react to the presence of obstacles along the track and further experiments have to be performed to determine the exact molecular mechanism responsible for switching between the types of motion.

Although the localization precision is comparable between the two tracking methods (~ 10 nm in xy, ~ 20 nm in z), 3D orbital tracking offers the ability to localize particle with higher acquisition rates (up to 200 Hz vs. 20 Hz) and is not biased through the particle shape. It is therefore possible to perform experiments without the internalization of microspheres, which potentially can alter the natural function of cellular transport. The cytoskeleton context, addressed by correlative imaging, requires a complicated and time consuming process with a low yield of trajectories. To increase the overall efficiency of the experiments, which correlate particle transport with the cytoskeleton, the 3D orbital tracking microscopy was further improved. The modifications of the tracking hard- and software presented in chapter 4 provide the technical foundation to perform dual-color 3D orbital tracking microscopy. With this approach, it will be possible to measure the localization of the particle in the context of the local cytoskeleton structure in real-time with a precision of a few dozen nanometers in all three dimensions. Preliminary experiments using the dual-color tracking approach were performed. In these experiments, the offset between the green and red channel of the trajectory data (Fig. 6.6 a) is biased through several effects. First, the laser foci for the green and red channel are slightly shifted with respect to each other. This shift can be removed by applying offset levels along the x,y and z axis. The second bias is introduced by the different widths of the green and red point spread functions and require different look-up tables for the green and red channels. The last bias is introduced by the microtubule shape. To account for the quasi infinite elongation the implemented look-up table has to be modified.

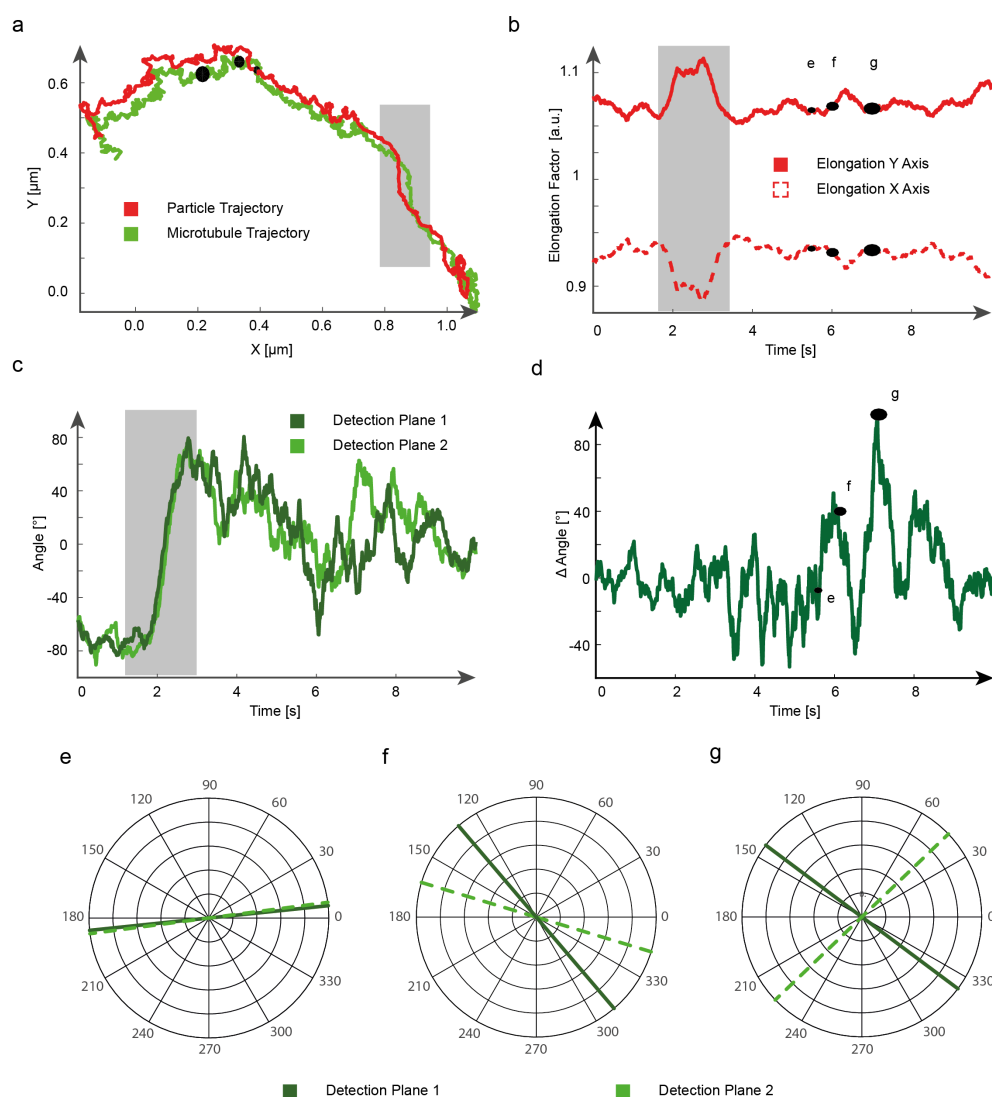


Figure 6.6 | Preliminary dual-color tracking results: a) Dual-color tracking data of the lysosome location (red) and microtubule structure (green). Data was acquired using alternating laser excitation to avoid spectral crosstalk between channels at a data acquisition rate of 100 Hz. The black dots with various sizes indicate time points in the vicinity of a microtubule intersection. b) Each graphs show the elongation of the particle along the x- and y-axis of the tracking coordinate system. The gray area marks an event, where the microtubule is bent and thus, the orientation of the particle and its elongation with respect to the x-axis changes. c) The phase of the second harmonic Fourier coefficients allows to calculate the orientation of the microtubule strand for each detection plane. For single microtubule strands, both angles overlap (d,e). When encountering an intersection, the difference between both angles strongly deviates from 0 (f,g).

The necessary modifications of the tracking software to account for these effects can be implemented in the near future. Despite the unknown offset between the data points in the lysosome and microtubule trajectory data, the preliminary data demonstrates the feasibility of dual-color tracking. Besides other questions, 3D orbital tracking will help to understand pausing events at intersections that show significant motion along the z-axis but could not be resolved properly due to the slower acquisition rates of the correlative imaging approach. The analysis of the second harmonic frequencies of the fluorescent signal recorded during one full orbit allows us to determine the elongation and orientation of the tracked particle in the lateral plane over the course of the experiment (Fig. 6.6 b)). Using the same principle, it is possible to determine the structure of the underlying cytoskeleton (Fig. 6.6 c-g)). The second harmonic amplitude and phase will be identical for both detection planes when a particle travels along a single microtubule. Upon encountering an intersection, the crossed microtubules will generate different signals in the detection planes. Since each microtubule will mostly contribute to one or the other detection plane, the orientation of both microtubules can be calculated providing additional context from the experimental data.

Recent optogenetic developments that introduced selective and reversible binding of motor proteins to cargo upon irradiation with ultra-violet light in the native cellular environment makes it possible to study the influence of motor proteins on the behavior of cargo [92]. The precise manipulation capabilities of the orbital tracking method will allow to us move away from bulk photo manipulation towards single particle manipulation experiments.

Chapter 7

Studying Mitochondrial Dynamics In Vertebrate Axons In Vivo

7.1 Introduction

The transport of mitochondria inside the stem axon and the peripheral arbor of nerve cells is a highly regulated process, which is essential to maintain cell health and to support growth of neuronal connections [93,94]. The highly dynamic molecular machinery, involving motor and adaptor proteins, provides a mechanism by which the cell efficiently supplies its branches with metabolites, substrates and energy [95]. After their assembly, mitochondria are transported anterograde along the stem axon into the peripheral arbor through kinesin motors along a set of polarized microtubule strands. Degraded mitochondria are transported in retrograde direction back to the cell nucleus for recycling by cytoplasmic dynein [96]. Recent studies showed that in addition to microtubule based motors, Myosin Type V plays a critical but unknown role in mitochondrial transport in both directions [96,97]. A disturbance in this transport system can manifest itself in neurodegenerative diseases [98]. Several cell culture and invertebrate studies have revealed several key players of this transport system [74,99], but until now their spatiotemporal distribution and interactions remains unclear, especially in vertebrate systems [100].

To address this particular question, a recent study established the use of zebrafish embryos with fluorescently tagged mitochondria as a vertebrate model system [101]. Zebrafish larvae offer several particular advantages over

other systems. They allow visualizing structures in their natural environment, without the necessity of performing surgery and drugs and genes can be delivered easily into the nervous system. Plucińska *et al.* showed that transport in the zebrafish nervous system closely resembles transport in mammalian systems and thus is a valid model to study basic cellular biology [101].

Although mitochondrial dynamics have been studied extensively with a variety of biological, genetical and optical methods, the spatiotemporal distribution of mitochondria and the synchronization of the regulative processes still remain unknown [100]. By combining an advanced genetic model system (genetically modified zebrafish embryos) with an advanced single-particle tracking system it is possible to measure the transport of single mitochondria with unprecedented precision and over longer distance than previously possible in single-particle tracking experiments. This approach allows us to create a spatiotemporal baseline model for the transport processes of mitochondria in neurons. By comparing this model with other systems expressing factors involved in neurodegenerative diseases (e.g. hyperphosphorylated tau proteins [102]), it will be possible to examine their individual effect on axonal transport.

The first scope of this project was to determine if 3D orbital tracking microscopy is suitable to study mitochondrial transport in living zebrafish embryos. This involves the selection of appropriate fluorescent proteins for the simultaneous orbital tracking and wide-field measurements, the development and application of a suitable analysis algorithms and to confirm the acquired results with previous studies.

In the second part of this project, mitochondrial transport along the stem axon was analyzed to study and classify different movement types, which are responsible for transport and to derive a transition pattern for describing the relationship between individual motion states during transport.

The last scope of this project was to determine whether the pausing behavior of individual mitochondria is influenced through local biases on the stem axon, for example other cargo, which is hindering the transport.

Preparation, labeling and drug treatment of zebrafish embryos were developed and performed by Dr. Gabriela Plucińska and Rachel Thong in the Group of Prof. Thomas Misgeld, Technical University Munich.

7.2 Results

7.2.1 3D Orbital Tracking Microscopy In Live Zebrafish Embryos

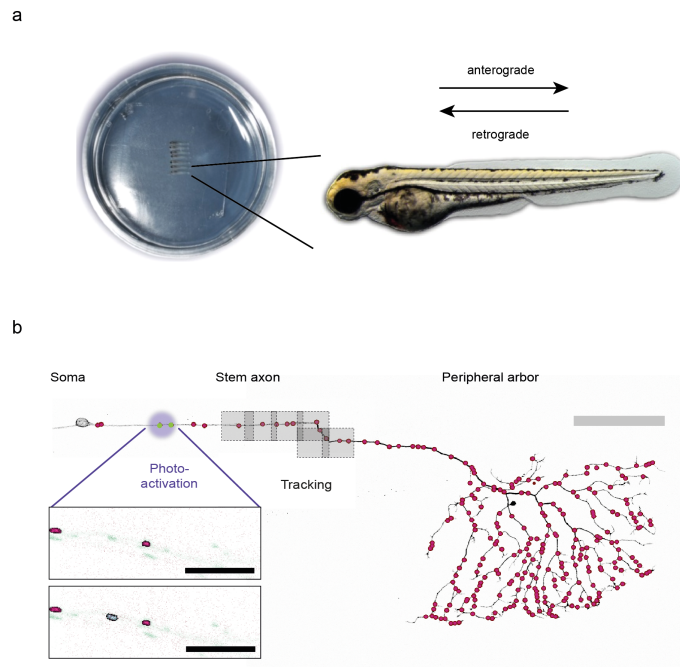


Figure 7.1 | Experimental Setup: a) Zebrafish embryos embedded in low melting agarose and anesthetized using tricaine. b) Confocal reconstruction of a Rohon-Beard sensory neuron, individual mitochondria are shown in red (scale bar $100 \mu m$). The imaging sites in the stem axon are shown in grey. Multiple boxes indicating camera field of views between long-range tracking events. Confocal images for a single TagRFP/PA-GFP labeled mitochondrion before and after photoactivation are shown (scale bar $5 \mu m$). Republished with permission of [101], permission conveyed through Copyright Clearance Center, Inc..

For tracking experiments, zebrafish embryos were fluorescently labelled with mitoTagRFP-T [21] (mitochondria for single-particle tracking) and memGFP [12] (axonal membrane for wide-field imaging) and embedded in a droplet of agarose for immobilization as described before in Plucińska *et al.* [101] (Fig. 7.1, see section 10.2 for materials and methods). The location of individual mitochondria was determined using a lateral xy scan and the tracking feedback was started by selecting a single mitochondrion in the stem axon.

Environmental data was recorded simultaneously to record the shape of the stem axon during the tracking process. Figure 7.2 shows wide-field images with the location of a single mitochondrion moving along the stem axon. When encountering the long-range tracking threshold the sample was moved on top of the microscope (after 10 and 30 seconds). Figure 7.3 shows the complete trajectory, which was acquired during the experiment and the corresponding countrate during the experiment. Due to photobleaching, which occurs when using fluorescent proteins, the average countrate of a single mitochondria drops over time. As the tracking feedback always tries to minimize the modulation in the orbit signal, it is inevitable that the laser focus will always reposition on top of the brightest particle in the vicinity of the orbit. This behavior creates two major problems. First, it is impossible to follow a single particle over longer distances and second, the tracking accuracy will be biased through the weaker fluorescent signals of other mitochondria in the vicinity of the orbit.

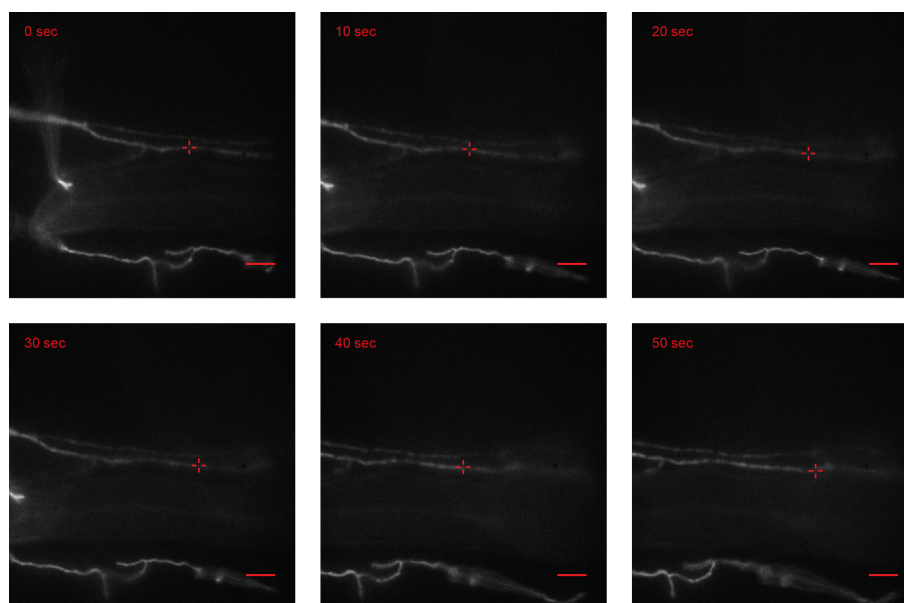


Figure 7.2 | Tracking mitochondrial motion in the context of the axonal structure: Wide-field images showing the movement of a single mitochondrion (red cross) along the stem axon (white), scale bar $5\mu m$. The stem axon is labeled with memGFP, the mitochondria with mitoTagRFP-T. The mitochondria position is added to the wide-field data using the coordinate transformation described in section 4.3.3. The zebrafish sample is repositioned during long-range events after 10 and 30 seconds.

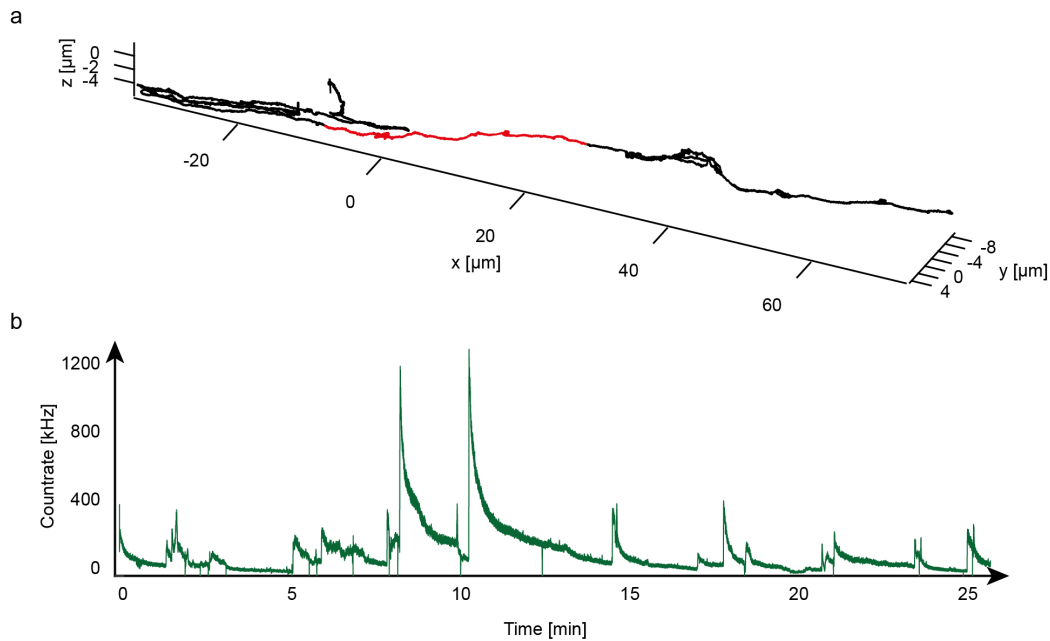


Figure 7.3 | Transport of multiple mitochondria inside the stem axon: a) The three dimensional trajectory data acquired during a 25 minute acquisition. The red points indicate the trajectory position from Fig. 7.2. b) Average counts per orbit for the trajectory shown in a). Sharp increases in intensity indicate points in time where the algorithm locked on to a brighter particle. Downward changes indicate long-range events, which results in a momentary loss of the particle and thus in a decreased count rate.

Photoactivation of individual mitochondria

To avoid these problems, the fluorescent labeling was changed to a photoactivatable green fluorescent protein, mitoPAGFP, for single-particle tracking [23]. In addition, the label for environmental observation was changed to mitoTagRFP-T to study inter-mitochondrial interactions. Prior to each trajectory, a single mitochondrion was photoactivated using 405nm light and successively tracked. During the experiment, the laser power was manually adjusted between 400 and 500 photons per orbit (40-50 kHz, 5ms orbit time + 1 dark orbit) to achieve an axial localization precision of $\sim 30\text{nm}$ (Fig. 4.14). This procedure enabled the unbiased tracking of individual mitochondria over distances of more than $100\mu\text{m}$ (Figure 7.4). Due to the axonal geometry and sample positioning, motion is carried out mainly in the xy-plane and thus each trajectory was analyzed using the two dimensional correlative analysis described in chapter 5. The analysis parameters

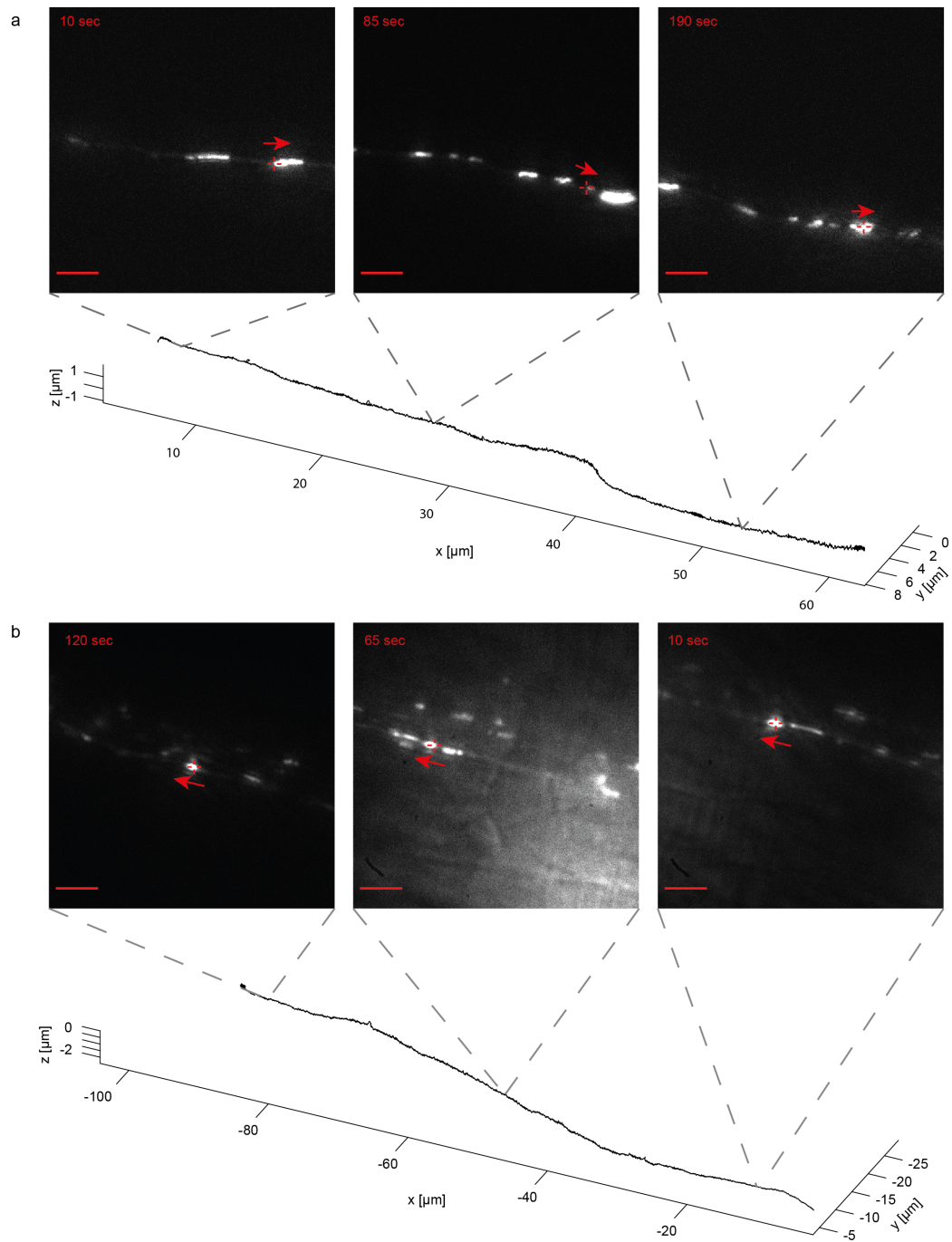


Figure 7.4 | Antero- and retrograde trajectories of mitochondrial motion inside the stem axon: Environmental data and 3D trajectories from a single photoactivated mitochondrion moving in the anterograde (a) and the retrograde (b) direction. Scale bar 5 μm . The direction of movement is indicated through the red arrows.

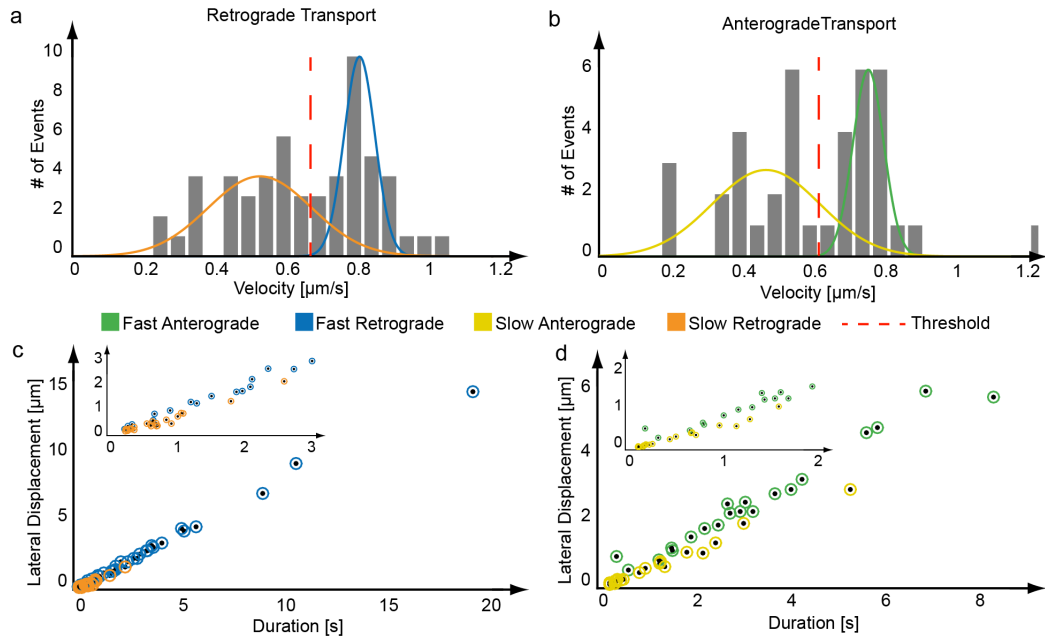


Figure 7.5 | Classification of antero- and retrograde motion into two individual motion states: Velocity histograms for an anterograde a) and retrograde b) moving mitochondrion. The velocity distribution in each direction was fit to a two-component Gaussian using a maximum likelihood approach. c,d) Based on the mean velocities of the fit, each active phase was assigned to either the fast or slow population.

of $\mu + 5\sigma$ as threshold level and 64 points as correlation window size were determined through simulations and showed a recovery rate of $> 90\%$. A maximum likelihood estimation using a two component Gaussian model was performed for individual trajectories to classify each active phase into a fast or slow state in the anterograde or retrograde direction (Fig. 7.5). The fast and slow movement states differ significantly in speed and processivity in the antero and retrograde direction (Fig. 7.6). Fast movement states carry out long-distance trafficking, while slow states are responsible for more confined movements over shorter distances and time-scales. The difference in the speed of the fast anterograde and retrograde motion states can be explained by the fact that mitochondria employ different motor proteins depending on the movement direction, namely kinesins (KIF1B α and KIF5) and cytoplasmic dynein [74,99]. In contrast to the fast movement states, the slow populations showed nearly identical properties in both directions and are discussed in more detail in section 7.2.2. The tracking of photoactivated mitochondria was performed together with Leo Hansbauer (F-Praktikant).

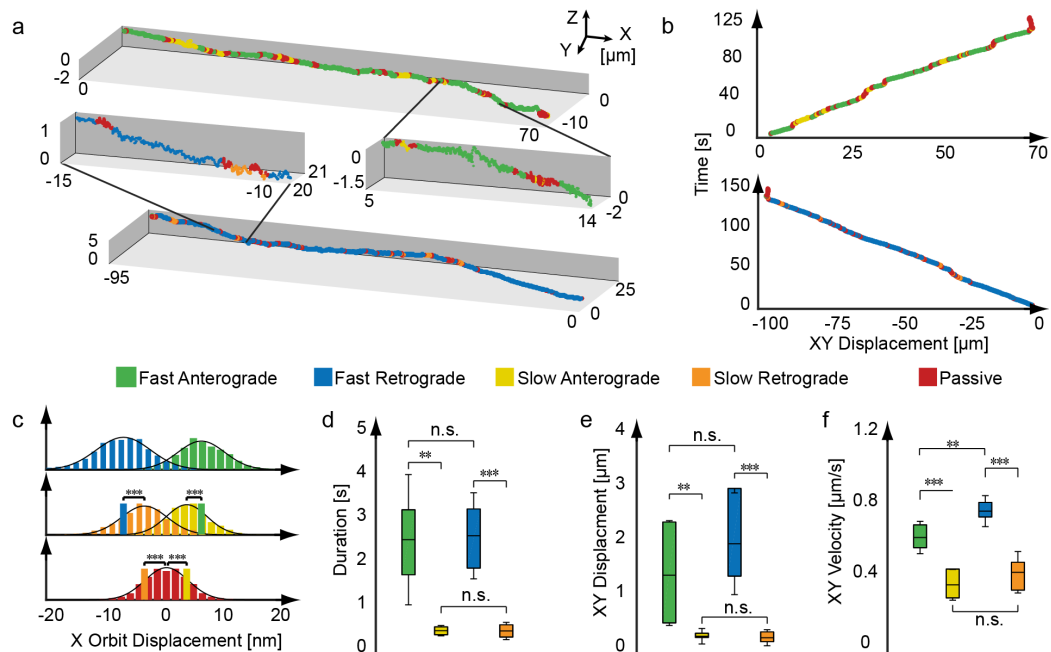


Figure 7.6 | Mitochondrial motion is driven by five individual motion types: a) Analyzed and color coded trajectories from Fig. 7.4). Color coding indicates phases of fast motion (green - anterograde; blue - retrograde), slow motion (yellow - anterograde; orange - retrograde) and passive phases (red). b) Kymographs of the trajectories shown in panel a). c) Orbit displacement along the x axis. The different phases in each direction (fast, slow and passive) show significant differences between the mean displacement values. d-f) Population properties determined from 43 mitochondrial trajectories. Box plots shows average, the 25 and 75 percentile, error bars indicate standard deviation, Asterix indicate significance levels determined by a two-sided t-test of *: $p < 0.01$, **: $p < 0.005$ and ***: $p < 0.001$. Numerical values can be found in table 7.2

The influence of mitochondria shape on the localization precision

To quantify the effect of the mitochondrion shape on the precision of the tracking algorithm, two effects have to be considered. First, the distance from the particle to the center of the orbit is calculated using the frequency spectrum of the acquired intensity orbit. As stated in chapter 4, only the first harmonic signal of the frequency spectrum is used to derive the position. The shape of the tracked particle is encoded in higher harmonics of the frequency spectrum, e.g. the second harmonic for an elliptic particle like mitochondria. Thus, for small particles, which are not larger than the area covered by the rotating point spread function (approx. 1-1.5 μm , depending on the orbit radius), the shape does not influence the precision of the tracking algorithm (Fig. 7.7 a)). The second effect influences the tracking precision if the major axis of an elongated particle is significantly larger than the orbit diameter. The first order harmonic represents the center of mass of the fluorescent signal in the area probed by the rotating orbit. For particles with a significant ellipticity (e.g. large mitochondria), the variation of the acquired intensity orbits does not change for a certain area in the center of the particle (Fig. 7.7 a), right panel). For such a particle, which undergoes a directional change, backwards motion will be underestimated. To determine the size threshold upon the tracking precision is impaired, stationary mitochondria of varying sizes were tracked. In addition the whole sample was externally moved in a sinusoidal pattern using a piezo stage. To quantify the loss in amplitude, which occurs at the peaks of the periodic signal, the acquired signal was fitted with the appropriate model and the recovered amplitude was plotted against mitochondria size (extracted from the simultaneous acquired wide-field data using the FWHM along the major and minor axis as size estimation). For mitochondria, which are smaller than $\sim 1.5\mu m$, the amplitude is fully recovered. Bigger mitochondria lead to a significant decrease of the recovered amplitude. Hence moving mitochondria are significantly smaller than stationary ones (Fig. 7.7, black triangles and circles), the shape and size of these particles do not decrease the localization precision of the microscope.

Shape experiments were performed together with Lisa Haddick (F-Praktikant).

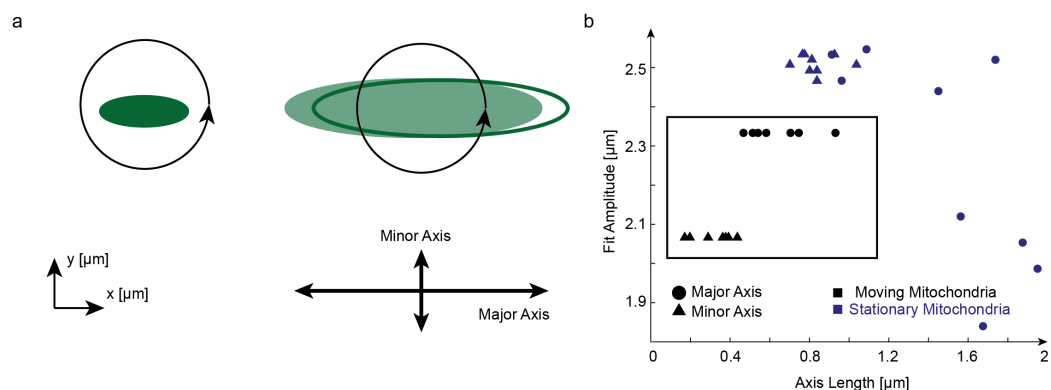


Figure 7.7 | Influence of mitochondrial shape on localization precision: a) Left Panel: Elliptical particles (green) smaller than the orbit diameter can be precisely located using the tracking algorithm. Since only the first order harmonics are used for localization, the particle shape does not influence the tracking precision. Right Panel: Elliptical particles, which are significantly larger than the orbit radius can reduce the tracking accuracy. Movement along the major axis of the particle can not be determined precisely due to no change in the intensity orbit (green and dashed particle). b) Stationary mitochondria were moved along their minor and major axis in a sinusoidal pattern with an external piezo stage (dark blue triangles and circles). For small mitochondria ($< 1.2\mu\text{m}$) the amplitude of the applied sine voltage could be recovered using the proper fit model. For mitochondria larger than the threshold level, tracking accuracy was significantly impaired. Moving mitochondria inside the stem axon are significantly smaller than the threshold level (black triangles and circles) and can be precisely tracked. Adapted from [103].

The influence of the zebrafish heartbeat on localization precision

Single-particle tracking experiments in live organisms have the inherent problem that the specimen is exhibiting motion through its heartbeat. The resulting pressure changes in the cardiovascular system can temporarily deform the tissue in which tracking is performed. The acquired trajectories from living zebrafish embryos showed small repetitive fluctuations perpendicular to the prominent axis of the stem axon. Since single-particle tracking experiments in zebrafish embryos are performed in the stem axons, which are located beside dorsal longitudinal anastomotic vessels (DLAV) [104], we had to test if the heartbeat significantly influences the acquired data. To quantify the effect of the heartbeat on the measurements, a fluctuation analysis was performed (Fig. 7.8). In a first step, low frequency components (the under-

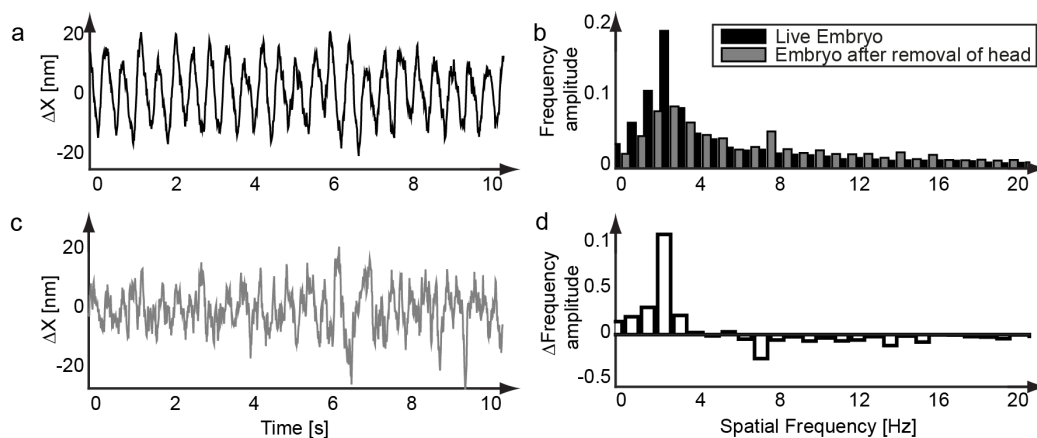


Figure 7.8 | Zebrafish heartbeat: a) Sinusoidal signal inside the trajectory data after the removal of low frequency components (underlying axonal structure). b) Frequency analysis of the trajectory shown in a) (black) shows a dominant peak with a Frequency of 2.38 Hz, which corresponds to the heartbeat of the zebrafish embryo. Surgical removal of the head removes the heartbeat contribution from the trajectory data (b, c). d) contribution of the heartbeat to the trajectory fluctuations.

lying axonal structure) are removed by subtracting a smoothed trajectory (50 points, 0.5 sec) from the raw trajectory data, which reveals a sinusoidal signal in the axis perpendicular to the DLAV's. A running Fourier analysis window was used to calculate the varying frequency components along the trajectory. The frequency analysis revealed an underlying signal of $\sim 2.38 Hz$ which corresponds to the heartbeat of the zebrafish embryo of 120-180 beats per minute. After surgically isolating the tail of the same zebrafish embryo shown in figure 7.8 a), the sinusoidal signal disappeared from the trajectory data. It is notable that the 3D orbital tracking system is capable of detecting sinusoidal amplitudes of $\sim 10 nm$ inside a living organism. However, the impact of the heartbeat on the analysis of mitochondrial transport is very small compared to the mitochondria travel distance and thus negligible as long as the tracked mitochondria is not located in the direct vicinity of the blood vessel. In these cases, the acquired data was discarded.

Experimental data validation

To validate our experimental approach, the obtained velocity values were compared to values reported previously when accounting for the lower temperature used in the single-particle tracking experiments. Due to their lower spatial and temporal resolution, Plucinska et al. were only able to discriminate a single motion type in the anterograde and retrograde direction [101]. The comparison between the wide-field analysis at $25^{\circ}C$ and $28^{\circ}C$ showed a 40% reduction of the lateral velocity for the reduced temperature. In addition, the velocity of the wide-field analysis represents the average speed of the fast and slow motion states interleaved with very short pauses, which can not be identified due to the poor time resolution of the wide-field analysis.

Population	Tracking Analysis $25^{\circ}C$	Wide-field analysis $25^{\circ}C$	Wide-field analysis [101] $28^{\circ}C$
Retrograde			
Fast	0.76 ± 0.08	0.55 ± 0.07	0.92 ± 0.02
Slow	0.42 ± 0.11		
Anterograde			
Fast	0.62 ± 0.09	0.45 ± 0.08	0.77 ± 0.01
Slow	0.36 ± 0.08		

Table 7.1 | Data validation: Velocity comparison between single particle tracking, wide-field measurement and previously published results. To be able to compare the experimental conditions, the same analysis algorithm as in reference [101] was used to analyze the simultaneously acquired wide-field image.

The shown experimental data verifies that 3D orbital tracking is applicable in live organisms. The use of a photoactivatable fluorescent protein allows tracking of individual mitochondria over distances of more than $100\mu m$ with a precision of less than 5nm and a temporal resolution of 100Hz. The simultaneously acquired environmental wide-field images verified the spatiotemporal mapping process. The shape analysis showed that, due to their small size, moving mitochondria do not impair the precision of the tracking microscope. Last, the fluctuation analysis revealed a very small and thus negligible impact of the heartbeat on the trajectory data as long as the tracked mitochondria is not in the direct vicinity of the blood vessel.

Property	Fast Anterograde	Slow Anterograde	Fast Retrograde	Slow Retrograde	Passive
Orbit Displacement [nm]	5.8 ± 5.0 n=83272	3.4 ± 3.7 n=27638	-7.1 ± 5.3 n=61217	-3.7 ± 4.4 n=21984	0.0 ± 3.9 n=1153949
Duration [s]	2.53 ± 1.48 n=331	0.46 ± 0.11 n=416	2.62 ± 0.98 n=220	0.45 ± 0.20 n=339	-
XY Displacement [μm]	1.47 ± 0.96 n=331	0.30 ± 0.15 n=416	2.07 ± 0.97 n=220	0.27 ± 0.15 n=339	-
XY Velocity [$\mu m/s$]	0.62 ± 0.09 n=331	0.36 ± 0.08 n=416	0.76 ± 0.08 n=220	0.42 ± 0.11 n=339	-

Significance Levels	Orbit Displacement	Duration	XY Displacement	XY Velocity
Fast anterograde vs. slow anterograde	2.8e-5	1.7e-3	3.9e-3	2.7e-6
Fast retrograde vs. slow retrograde	1.3e-7	5.1e-5	2.2e-4	1.0e-6
Fast anterograde vs. fast retrograde	-	0.88	0.18	1.6e-3
Slow anterograde vs. slow anterograde	0.49	0.92	0.67	0.14
Slow anterograde vs. passive	6.1e-7	-	-	-
Slow retrograde vs. passive	5.3e-7	-	-	-

Table 7.2 | Numerical values of motion parameters: Determined by the analysis of 43 individual trajectories from 16 zebrafish embryos. Values are given as the mean plus the standard deviation. Significance levels were determined by a two-sided t-test.

7.2.2 Characterization of Mitochondrial Motion

Nocodazole Treatment

The analysis of the trajectory data revealed a previously unknown motion state. Unlike the fast components, the slow movement phases showed similar properties (speed, duration and processivity) in antero- and retrograde direction (Fig. 7.6). To gain some mechanistic insight into the transport processes, a second round of experiments were performed. To test if the slow motion state engages motors that run on microtubule filaments, nocodazole (400nM) was added to the standard imaging buffer to disrupt microtubule growth.

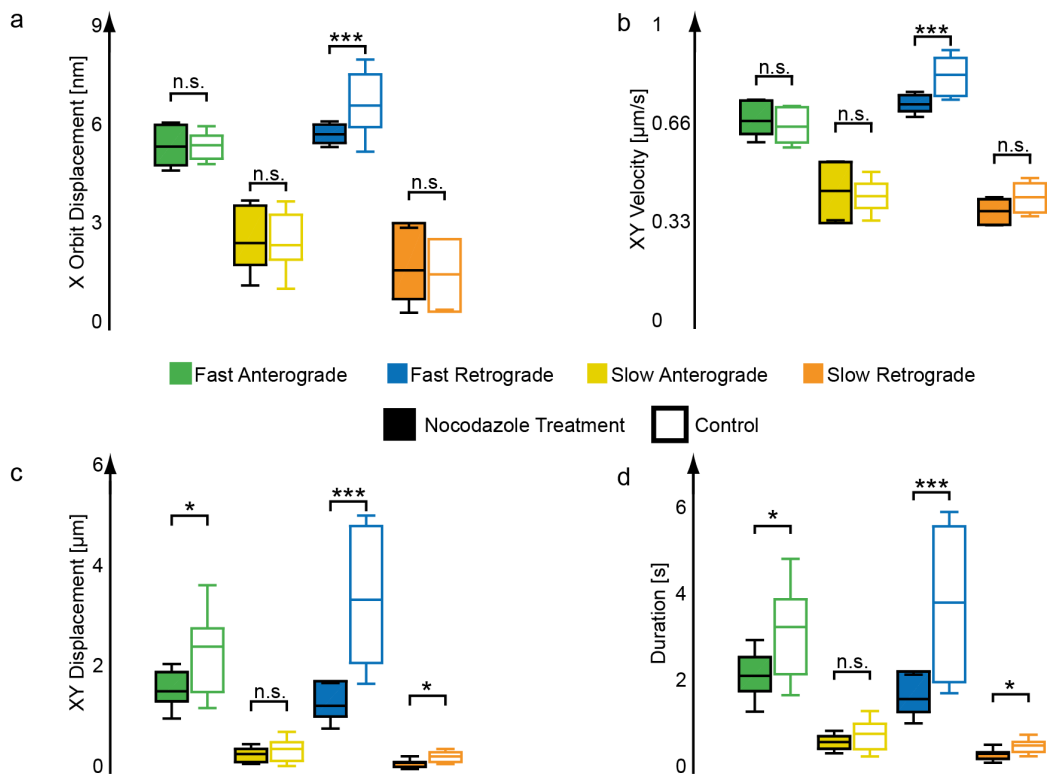


Figure 7.9 | Nocodazole treatment affects mitochondrial transport: Nocodazole treatment primarily affects fast movement states of mitochondrial transport. Box plots shows average, the 25 and 75 percentile, error bars indicate standard deviation, Asterix indicate significance levels determined by a two sided t-test of *: $p < 0.01$, **: $p < 0.005$ and ***: $p < 0.001$. Numerical values can be found in table 7.3 and 7.4.

The successful delivery of nocodazole into the rohon-beard sensory neurons was confirmed using fluorescently tagged tip binding protein as a control. The short incubation time of two hours prevented detrimental effects, which arise from long-term nocodazole treatment. Treatment with nocodazole primarily influenced the fast movement populations and only a small influence on the properties of the slow movement states was observed (Fig. 7.9). This suggests that the slow motion states engage other motors than the fast components, e.g. myosins walking on actin tracks, a mechanism that was suggested by other studies [96, 97].

Transition Pattern

In the recorded trajectories, mitochondria show a directed motion in antero- or retrograde direction but also exhibit short-term directional changes engaging the slow motion type. After a certain period of time the direction of motion is again reversed and the mitochondria continue in their original direction. Since this process requires a high level of regulation, the transitions between motion states and the transition time between them were analyzed (Fig. 7.10). A number of trends become apparent from this analysis. First, an analysis of the pause durations suggests two different pausing mechanisms: Pauses involving fast motion states (fast to fast or fast to slow transitions) show mono-exponential distributions with decay constants of 1.94 s and 1.97 s, whereas transitions between slow states show an increased decay constant of 3.2 s (Fig. 7.10). Pauses longer than 20 s were always (97%) associated with transitions, which involve a slow state. In addition, 56% of pauses longer than 10 s (n=97) and only 19% of shorter pauses (n=1137) were involved in a change of directionality. Secondly, there is a clear directionality of the trajectory determined by the direction of fast motion. We did not observe any transitions between fast anterograde and fast retrograde states within one track. Mitochondria traveling in the prominent direction of the trajectory, have a high probability to continue in the same direction (77% or higher depending on the mode of motion). Approximately half of the time, the mitochondria remain in the same motional state (i.e. direction and velocity) and directional changes between fast and slow motion were unlikely (5.9% of all pauses). The analysis of the transition probabilities and durations suggests that a number of mechanisms might influence the different state transitions along a mitochondrion's axonal trajectory and that these mechanisms are substantially more complex than anticipated from previous *in vitro* reports [105].

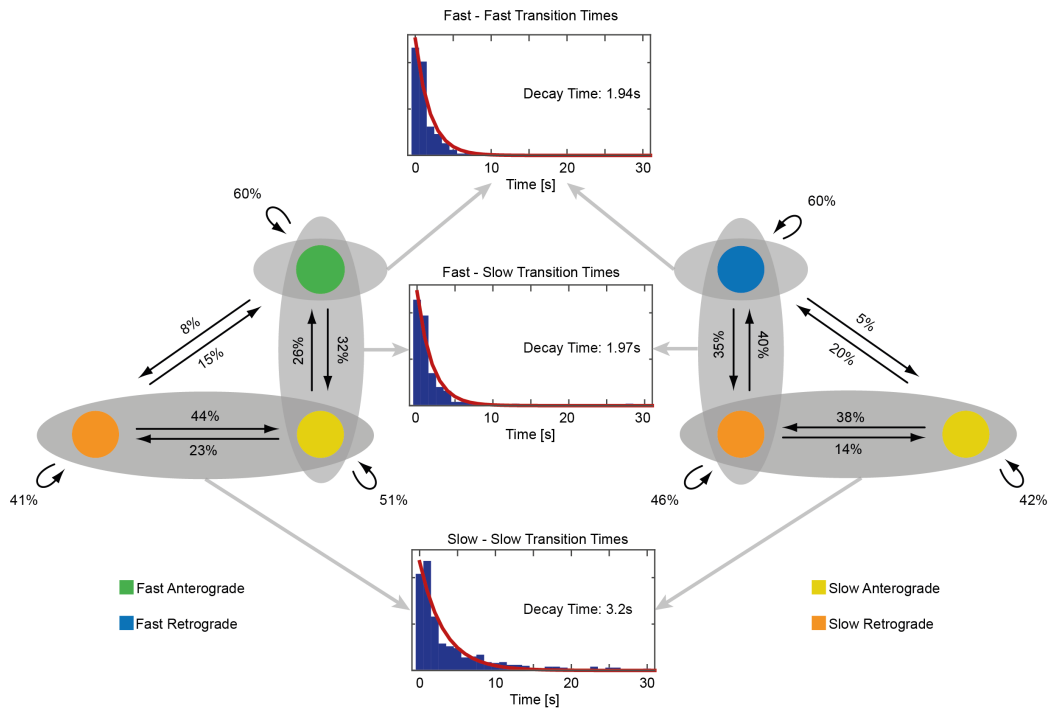


Figure 7.10 | Transition probabilities and pause durations: A transition probability diagram is shown for retrograde and anterograde moving mitochondria. The probability of transitions between different movement phases are given in the diagram (n=1234 transitions). Pauses between transitions involving the fast motion states show mono exponential decay constants of 1.94s (fast-fast transitions) and 1.97s (fast-slow transitions). Transitions between slow states show a decay constant of 3.2s. Directional transitions between the fast and slow are rare events and no statistical relevant results could be obtained.

	Fast Anterograde	Slow Anterograde	Fast Retrograde	Slow Retrograde
XY Velocity [$\mu m/s$]				
Nocodazole + 1% DMSO	0.65 ± 0.07 n=126	0.44 ± 0.09 n=122	0.71 ± 0.04 n=106	0.37 ± 0.04 n=78
1% DMSO	0.64 ± 0.07 n=143	0.42 ± 0.08 n=185	0.80 ± 0.08 n=84	0.42 ± 0.06 n=144
Significance	0.74	0.74	1e-5	0.09
Orbit Displacement [nm]				
Nocodazole + 1% DMSO	6.1 ± 0.5 n=26909	3.9 ± 0.9 n=8097	-6.3 ± 0.3 n=17804	-3.3 ± 0.9 n=3420
1% DMSO	6.1 ± 0.4 n=45355	3.9 ± 0.9 n=15897	-7.0 ± 1.0 n=27041	-3.2 ± 0.8 n=9298
Significance	0.46	0.45	1e-7	0.29

Table 7.3 | Numerical values of motion parameters from nocodazole treated embryos: XY velocity and orbit displacement for zebrafish embryos treated with Nocodazole (400nm + 1% DMSO) and the control (1% DMSO). Values are given as the mean plus the standard deviation. Significance levels were determined by a two sided t-test.

	Fast Anterograde	Slow Anterograde	Fast Retrograde	Slow Retrograde
Duration [s]				
Nocodazole + 1% DMSO	2.16 ± 0.80 n=126	0.69 ± 0.25 n=122	1.64 ± 0.54 n=106	0.43 ± 0.20 n=78
1% DMSO	3.25 ± 1.52 n=143	0.87 ± 0.51 n=185	3.79 ± 2.02 n=84	0.61 ± 0.24 n=144
Significance	8e-3	0.02	4e-6	6e-3
XY Displacement [μm]				
Nocodazole + 1% DMSO	1.43 ± 0.48 n=126	0.33 ± 0.17 n=122	1.17 ± 0.40 n=106	0.18 ± 0.11 n=78
1% DMSO	2.21 ± 1.07 n=143	0.41 ± 0.30 n=185	3.03 ± 1.47 n=84	0.29 ± 0.13 n=144
Significance	7e-3	0.06	5e-7	8e-3

Table 7.4 | Numerical values of motion parameters from nocodazole treated embryos: Duration and XY displacement for zebrafish embryos treated with Nocodazole (400nm + 1% DMSO) and the control (1% DMSO). Values are given as the mean plus the standard deviation. Significance levels were determined by a two sided t-test.

7.2.3 Pausing behavior of individual mitochondria

The transition pattern analysis revealed different pause behaviors, which are closely correlated to the movement types before and after the passive state. To distinguish whether the pausing behavior is an effect caused by the underlying microtubule track or other cargo, which is transported in parallel, the original experiment was modified. MitoPAGFP as the tracking label for mitochondria was exchanged with mitodendra2, a photo-convertible fluorescent protein that changes the excitation wavelength upon irradiation with ultraviolet and blue light from 490 to 553nm [24]. The label for wide-field imaging was kept the same, mitoTagRFP-t. This experimental approach allowed us to "erase" the fluorescent signal in the camera field of view by shifting the emission maxima using 405nm light from the tracking to the wide-field channel. New incoming mitochondria were tracked until leaving the field of view or resting for more than a minute at one location. By erasing the residual fluorescence in the field of view after every recorded trajectory, several different mitochondria could be tracked over the same stretch of axon.

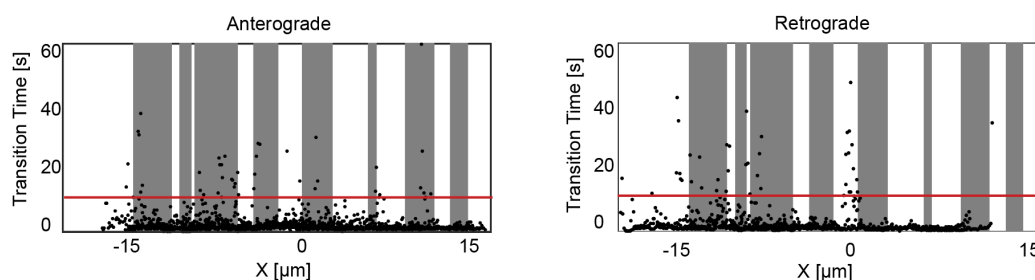


Figure 7.11 | Repetitive tracking of mitochondria over the same stretch of an axon: The transition time to transverse 100nm bins is plotted as a function of the position along the axon. The position and elongation of stationary mitochondria along the axons is indicated by the gray boxes. The red line indicates a threshold level to identify bins of slow movement.

Figure 7.11 shows the transition time from 16 trajectories acquired over the same stretch of an axon in the antero- and the retrograde direction. A small transition time depicts motion whereas a high transition times represent pauses. When plotting the transition time for several trajectories, a pattern emerged. For most of the axon, movement progress was relatively steady (transition times $< 10s$ to cross $1 \mu m$) while other regions showed distinct foci of slow progress. By extracting the positions of stationary mitochondria from the simultaneously acquired wide-field images, it became obvious that most of these foci coincide with the presence of stationary mitochondria. The appearance of other foci that are not associated with stationary mito-

chondria suggests that other factors such as the local geometry of the axon, the local milieu, local calcium hot spots [106] or substrate availability [107] significantly influence the motion along the neuron.

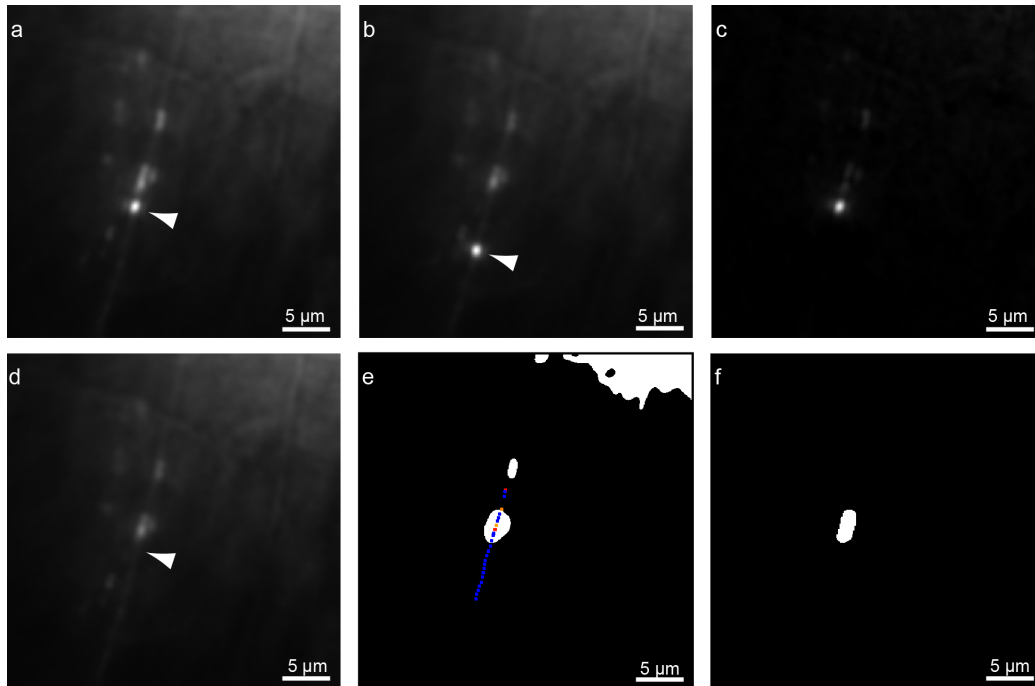


Figure 7.12 | Analysis of environmental data: a) Initial frame $I_{(x,y,t)}$ and b) the time shifted frame $I_{(x,y,t+10)}$ showing a single moving mitochondria (white arrows). c) remaining positive intensity values after subtracting a) from b). d) subtraction of frame c) from frame a) leads to an image containing only stationary components. e) Binary image of the average and smoothed images between long-range events. The corresponding particle trajectory used to filter out artifacts is indicated by colored data points. f) The final image used to calculate the position and elongation of stationary mitochondria along the particle trajectory.

To further analyze the pausing behavior of mitochondria, the simultaneously acquired wide-field images were analyzed to correlate the individual motion states with the position of other stationary mitochondria present on the axon. To extract the position and elongation of stationary mitochondria the dynamic components are removed from the video (Fig. 7.12) using the following equations:

$$\Delta I_{(x,y,t)} = I_{(x,y,t+10)} - I_{(x,y,t)}$$

$$\Delta I_{(x,y,t)} = \begin{cases} \Delta I_{(x,y,t)}, & \text{if } \Delta I_{(x,y,t)} < 0 \\ 0, & \text{if } \Delta I_{(x,y,t)} > 0 \end{cases} \quad (7.1)$$

$$I_{Stationary(x,y,t)} = I_{(x,y,t)} + \Delta I_{(x,y,t)}$$

where $I_{(x,y,t)}$ denotes the intensity values for each pixel (x,y) over time (t). The subtraction of $I_{(x,y,t)}$ from a time-shifted image $I_{(x,y,t+10)}$ creates an image containing the components of the video, which have moved between the timepoints t and t+10 (Fig. 7.12 c)). Positive values contain the dynamic components of image $I_{(x,y,t+10)}$ and negative values the dynamic components of frame $I_{(x,y,t)}$. By adding the negative value from $\Delta I_{(x,y,t)}$ to $I_{(x,y,t)}$, the dynamic components are removed from the original image (Fig. 7.12 d)). This procedure is repeated for all frames between two long-range tracking events. The resulting frames are averaged, smoothed by 5 points and the image is converted to a binary image using a threshold of the average intensity value plus 5σ . To remove artifacts such as cells and other axons in the vicinity of the tracked mitochondria, values outside an area of 11x51 pixel around the particle trajectory are set to 0 (Fig. 7.12 e,f)).

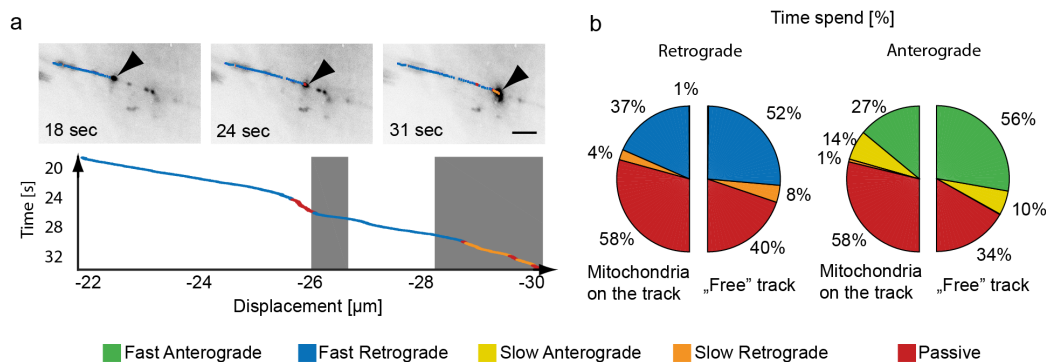


Figure 7.13 | Influence of stationary mitochondria: a) Mapping of the trajectory data of single mitochondrion (black arrow) onto the inverted wide-field images (scale bar $5\mu\text{m}$). The additional kymograph clearly shows the changing motion behavior of the moving particle upon reaching the vicinity of stationary mitochondria (grey areas). b) Pie charts indicating the fraction of time spent in each motion state related to the local presence or absence of a mitochondrion in the retrograde or the anterograde direction (n=16 trajectories, 9 fish).

Due to the rough alignment of the stem axon with the x axis of the tracking microscope, the location and elongation of stationary mitochondria is calculated using only the x dimension. By correlating the trajectory data with positions of other mitochondria, it became evident, these obstacles significantly influence motion along the axon (Fig. 7.13). Mitochondria moving along a "free" track spend the majority of time in fast movement states. Upon encountering a stationary mitochondria, the time spent in the passive state substantially increased in both directions (anterograde: 34% to 58%, retrograde: 40% to 58%). In addition, the fast anterograde transport is affected substantially (the ratio between time spent in the fast state vs. slow state decreased from 56% : 10% = 5.6 to 27% : 14% = 1.9). In contrast, the time spent in the fast motion state in retrograde direction was not reduced and even increased slightly (52% : 8% = 6.5 to 34% : 4% = 9.3). These results lead to two conclusions. First, stationary mitochondria act as significant roadblocks for moving mitochondria. Second, the kinesin driven fast motion state in anterograde direction is not able to overcome such roadblocks and thus the slow motion state is engaged. These findings are in line with previous *in vitro* observations that retrograde transport might be less sensitive towards obstacles [108] and the "shift to low gear" mechanism in anterograde direction is used to circumvent obstacles, which cannot be overcome by the driving forces of the kinesin motor.

7.3 Discussion & Outlook

The performed experiments showed for the first time that single particle tracking experiments with nanometer precision and ms temporal resolution can be performed in an *in vivo* system. The presented tracking microscope is capable of tracking individual mitochondria over distances of more than 100 μm using the newly developed modifications of the orbital tracking technique. In addition to the feedback mechanism responsible for nanometer localization, the long-range tracking modus re-centers the specimen on top of the microscope once a particle reaches a spatial threshold. This approach removes the limits of conventional microscopy, where a particle is lost when leaving the region of interest. In addition, the tracking precision over the whole trajectory is kept constant by keeping the object in an area unobstructed by optical aberrations, which decrease the tracking accuracy in regions far away from the origin.

To compensate for bleaching, time resolution can be traded in favor of prolonged imaging time by switching off the laser excitation of every other or for n-1 orbits, a feature coined "dark orbits". In biological specimens where the number of emitted photons is limited the microscope systems allows us to optimize the experimental design according to the area of interest. As moving mitochondria only have a very small displacement of a few nanometers in 10ms, the "dark orbit" feature allowed us to image single mitochondria for several minutes. By increasing the number of dark orbits, long term measurements on the timescale of an hour are possible.

We performed several controls to test whether the heartbeat of the zebrafish or the shape of mitochondria are affecting the recorded trajectories, several control measurements were performed. With a careful analysis, the heartbeat of the zebrafish could be detected on the axis perpendicular to the dorsal longitudinal anastamotic vessels. Depending on the distance to the cardiovascular system, the heartbeat showed varying contributions to the trajectory data. However, as the displacement due to the heartbeat is small compared to the travel distance (nm vs. μm) we can ignore it. Upon surgically removing the head and heart of the embryo, the heartbeat contribution disappeared from the trajectory data. It is notable that the tracking microscope is sensitive enough to detect the heartbeat through sinusoidal amplitudes of $\sim 10nm$, showing the superior stability and precision over conventional microscopes. To determine the effect of the mitochondria shape on the localization precision of the tracking algorithm, stationary mitochondria were externally moved with a piezo stage to simulate directional changes.

Mitochondria with a major axis shorter than $1.5\mu m$ showed no decrease in localization precision. Since moving mitochondria inside a stem axon have a mean length of $\sim 0.35\mu m$, the tracking algorithm has the same localization as for the round beads used to calibrate the microscope.

When comparing the obtained experimental results with a previous study [101], the superior spatial and temporal resolution provided a deeper insight into mitochondrial dynamics. A previously unknown motional state could be observed, which transports mitochondria over short distances and helps to circumvent obstacles, such as other mitochondria. Mechanistic experiments (using 400nm Nocodazole to depolymerize the microtubule system) showed that unlike the slow motion state, fast motion is primarily affected by impaired microtubules. One possible explanation is the involvement of myosin motors, which are present in the stem axon. Another possibility is a "tug of war" between concurrent motors, which significantly changes the motility of cargo. It is notable, that the 1% DMSO, which is present in the Zebrafish buffer (to enhance the uptake of nocodazole), has a more prominent but previously unknown effect than nocodazole and seems to stabilize the run length of the fast motion state in comparison to untreated embryos.

The huge number of data points and recorded trajectories allowed us to create a transition pattern between the five different motional states. Each mitochondria has a predefined polarity of motion, which is preserved until reaching the peripheral arbor of the axon. Some unknown mechanism reverses the polarity in the arbor to allow the transport of damaged and aged mitochondria back to the cell nucleus. Transitions between states with a preserved direction of motion are usually fast and happen on the timescale of a few seconds. Transitions that change the direction of motion require more time and are less probable. The complexity of the observed transport pattern leads to the conclusion, that a variety of unknown processes are involved.

To determine if mitochondria have a tendency to pause at specific locations in the stem axon, a repetitive tracking approach was used to measure the motion of several mitochondria over the same stretch of axon. The analysis of crossing times showed that most, but not all, of the long pauses could be associated with other stationary mitochondria present on the stretch of axon. This suggests that other factors such substrate availability or calcium signaling can cause longer pauses. Short pauses showed no particular pattern along the axon and could be caused by interruption in the microtubule track or collisions with other cargos. Following up on the association of long pauses with other mitochondria we further analyzed the types of motion active in

the vicinity of these obstacles. It became clear that mitochondria are a huge obstacle and efficiently slow down the motion of other mitochondria. Motion in anterograde direction is not efficient enough to overcome stationary objects without the help of the slow motion state. A factor that is in line with *in vitro* observation that kinesin motors are more susceptible to obstacles than dynein motors [108].

The presented results show that single particle tracking methods such as 3D Orbital Tracking offer new insights into interesting biological specimens. The acquired data from this project lays the foundation for further studies targeted towards the study of several processes within the highly complex mitochondrial motion. These involve the behavior at branching points, the further analysis of the slow motion states and their underlying transport mechanism and the polarization change of motion, which occurs in the peripheral arbor.

The possibility to photo-convert a single particle in its natural environment without altering the whole particle populations offers unprecedented spatiotemporal control over nanoparticles. The recent addition of a second tracking channel adds additional experimental options such as the simultaneous observation of a second fluorescent marker. Recent developments in the field of organelle targeted biosensors [109], optogenetic actuators of organelle physiology [110, 111], as well as motor [92] and track compositions [109, 112] allow the selective manipulation of cellular components. The precise manipulation abilities of the 3D orbital tracking microscope can be used to selectively control single moving organelles and will allow us to connect the type of motion with its physiological state. An aspect of organelle dynamics that, until now, could not be addressed by other approaches.

Chapter 8

Spinning Disk Confocal Microscope Upgrade

8.1 Spinning Disk Principle

A huge disadvantage of normal confocal microscopy (Section 2.2) is the need to mechanically scan the excitation volume laterally across the specimen to reconstruct images (Fig. 8.1a). By using piezo or galvano mirrors as scanning devices, the imaging time per scan can be estimated to be 1 Hz or even slower when using xy-piezos as stage scanning devices. This approach is even slower when acquiring a three dimensional image stack, which usually has acquisition rates of 0.05 to 0.1 Hz, depending on the number of lateral images. To increase the imaging speed and maintain the benefits of confocal microscopy, several confocal volumes can be imaged onto a camera by using a "Nipkow Disk" (Fig. 8.1b) [113]. This approach is called spinning disk confocal microscopy and was first implemented 1967 by Egger and Petran [114]. Their first design only used a pinhole pattern, which leads to a huge loss in excitation power. By adding a second coaxial plate containing a microlens array, which guides the excitation light through the pinholes, the transmission efficiency of the nipkow disk could be substantially improved [115]. After the laser light is focused by the objective onto the sample, the fluorescence from each confocal spot is guided back through the microlens array and directed out of the biplane disk. This makes it possible to image several dozens of confocal volumes simultaneously onto a camera. The imaging speed is then ultimately determined by the rotational frequency of the nipkow disk and can be increased to up to 1000 frames/s [116].

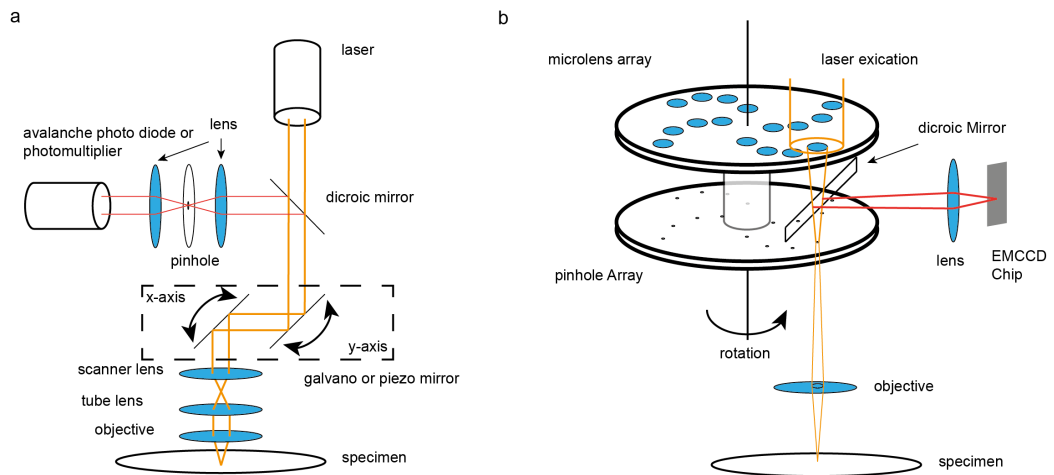


Figure 8.1 | Comparison between confocal and spinning disk confocal microscopy: a) Schematic of a confocal microscope. Image creation requires a raster scan over the whole sample. b) Schematic of a spinning disk confocal microscope. By using a rotating disk containing a pinhole array, multiple confocal volumes can be imaged simultaneously on an EMCCD chip (only a single excitation and emission pathway are shown).

8.2 Spinning Disk Upgrade Requirements

The upgrade of the commercial Spinning Disk confocal microscope (Andor Technology Ltd, Belfast) consisted of several new hardware components, such as a third EMCCD Camera and multiple laser lines (445, 514, 594 and 685 nm). The increased number of components required the development of a new microscope automation software, which in parallel should remove the constraints involved when using the commercial Andor IQ software: Camera triggering had to be performed using the master - slave configuration, which lead to different exposure times between master and slave cameras. In addition, laser exposure was not synchronized with the exposure window of the camera chips, which lead to unnecessary sample bleaching during the time the image is read out. The development of the new camera software provides the following features:

- Control and synchronization of new and existing hardware
- Synchronized triggering options for all EMCCD cameras (internal, external, frame transfer, etc.)
- Synchronize laser excitation with the exposure time of the EMCCD cameras
- Support and synchronization of the perfect focus system present in the Nikon Te2000 microscope body along with the cameras, laser lines and the z-piezo system
- Implementation of a photoactivation mode, which can be used to photoconvert the sample area every n^{th} frame.

8.3 Spinning Disk Confocal Microscope

The customized Spinning Disk Confocal Microscope is based on a commercial solution acquired from Andor Technology, Belfast. A laser combiner unit (ALC 401) contains 4 laser heads (405nm - Coherent Cube, 488nm - Coherent Sapphire, 561nm - Cobolt Jive and 640nm - Coherent Cube), which are controlled through a DeVasSys microcontroller (Devasys Embedded System, Removal of Laser Interlock) and Serial commands through the COM ports 201-204. In addition, the box contains a safety shutter (controlled through the DeVasSys microncontroller) and an acousto optical tunable filter crystal (operated by a control unit located in the Andor Precision Control Unit (PCU)). The 4 laser lines are coupled via dichroic mirrors (D1-D3) into a single mode fiber (Oz Optics) and the laser emission is transferred into the second laser combiner box.

The second laser combiner box contains four additional laser heads (445nm - Coherent Cube, 514nm - Coherent Cube, 594nm - Coherent Cube and 685nm - Coherent Cube), which are operated through a single control unit. All lasers are overlaid with dichroic mirrors (D4, zt 633 rdc; D5,zt 543 rdc; D6, zt488 rdp - AHF), combined with the ALC 401 laser lines (D7, 405/488/561/640 rpc - AHF) and guided into a second single mode fiber (OZ Optics). The emission power of each laser head is modulated through a combination of an analogue signal (0 to 5V) and a digital modulation (blinking).

Wavelength [nm]	Example Application / Fluorophore
405	Photoactivation TagBFP [117]
445	mTurquoise [118]
488	GFP [12]
514	Venus [20]
561	TagRFP-T [21]
594	mCherry [119]
640	PSmOrange [120] (after photoconversion)
685	iRFP [22]

Table 8.1 | Example fluorophores for spinning disk laser lines

The laser emission is coupled into the spinning disk unit (CSU-10, Yokogawa), containing the microlens and pinhole disks (Section 8.1). Due to the huge number of different laser lines, the dichroic mirror was replaced by a beam-splitter (70T/30R, AHF), which enables the user to select every

laser combination from both laser units. Once the laser lines and fluorescent emission is determined for one set of experiments, customized dichroics can be used to replace the normal beam-splitter. The laser emission is guided through a microscope body (Nikon) equipped with a perfect focus system and through the objective (Nikon) onto the sample, which rests on a z-piezo stage for image stack acquisition. The fluorescence is guided back and out of the CSU-10. Two 100mm lenses (Thorlabs) are used to translate the image plane to create space for three Andor Ixon EMCCD cameras. The emission is separated by two dichroic mirrors (D7 and D8) and additional emission filters remove remaining laser reflections from the beam path (E1-E3). The Nikon perfect focus unit (PFS) operates with an infrared LED at 770nm and thus, does not interfere with any of the laser lines or the respective fluorescence.

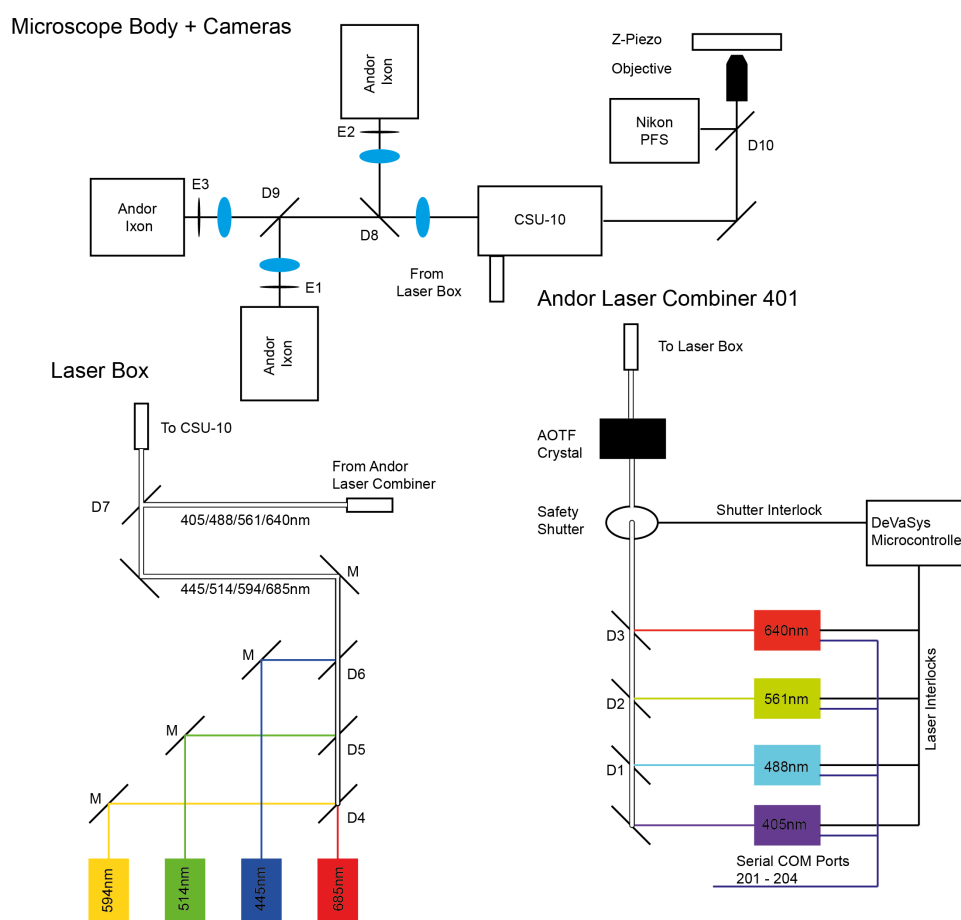


Figure 8.2 | Schematic of the spinning disk confocal microscope: Customized Andor Spinning Disk Confocal Microscope. In addition to the existing Andor Laser Combiner (ALC) 401 (providing 405, 488, 561 and 640 nm lasers), four more laser lines (445, 514, 594 and 685 nm) are introduced through a second laser box, which is connected through two single mode fibers with the ALC 401 and the spinning disk unit (CSU-10). All laser lines can be modulated through an acousto optical tunable filter or directly at the laser head. The microscope body is equipped with a Nikon perfect focus system and three Andor Ixon EMCCD cameras.

8.4 Hardware Connections

The spinning disk microscope is controlled by a combination of a host computer and a real-time embedded system containing a real-time computer and a field programmable gate array (cRIO 9074, National Instrument). To achieve full synchronization between all hardware components, several components have to be connected using a huge set of different cable types and signal standards. The connections can be separated into connections to the host and connections to the embedded system.

Host Connections

The host computer is used to process user interactions, the control of the real-time embedded system, the control of the microscope body and reads out the images acquired by the 3 Andor cameras. The cameras are attached to 3 Andor PCI cards inside the host computer to transfer the image data from each camera. Communication to the PFS system and the microscope body is achieved over a RS232 interface. Communication between the host and real-time computer is performed over a gigabit Ethernet connection.

Embedded Connections

The embedded real-time computer (cRIO 9074, National Instruments) triggers the Andor cameras via TTL pulses, operates the power of the laser lines through direct modulation at the laser heads (445, 514, 594 and 685 nm) or through an acousto optical tunable filter (405, 488, 561 and 640 nm) and moves the z-piezo. The embedded computer is equipped with two digital I/O modules (NI 9402) and three analogue output modules (2x NI 9263, 1x NI 9269).

Module (Slot)	Port	Connected to	Output Values
NI 9402 (1)	Digital Out 1	Camera 1	LVTTL
NI 9402 (1)	Digital Out 2	Camera 2	LVTTL
NI 9402 (1)	Digital Out 3	Camera 3	LVTTL
NI 9402 (1)	Digital Out 4	-	-
NI 9263 (2)	Analogue Out 1	Laser 405nm	0-5V
NI 9263 (2)	Analogue Out 2	Laser 488nm	0-5V
NI 9263 (2)	Analogue Out 3	Laser 561nm	0-5V
NI 9263 (2)	Analogue Out 4	Laser 640nm	0-5V
NI 9263 (3)	Analogue Out 1	Blanking AOTF	0 / 5V
NI 9263 (3)	Analogue Out 2	-	-
NI 9263 (3)	Analogue Out 3	-	-
NI 9263 (3)	Analogue Out 4	z-piezo	0-10V
NI 9402 (4)	Digital Out 1	Blanking 445nm	LVTTL
NI 9402 (4)	Digital Out 2	Blanking 514nm	LVTTL
NI 9402 (4)	Digital Out 3	Blanking 594nm	LVTTL
NI 9402 (4)	Digital Out 4	Blanking 685nm	LVTTL
NI 9269 (5)	Analogue Out 1	Laser 445nm	0-5V
NI 9269 (5)	Analogue Out 2	Laser 514nm	0-5V
NI 9269 (5)	Analogue Out 3	Laser 594nm	0-5V
NI 9269 (5)	Analogue Out 4	Laser 685nm	0-5V

Table 8.2 | Connection scheme and output values for each embedded module.

The embedded connections from slot 1 are connected via BNC cables directly to the trigger input of the Andor cameras. The connectors from slot 2 & 3 are connected via a 37 pin D-SUB female connector to the Andor precision control box (See table 8.3). Modules 4 & 5 are connected via BNC to LEMO adapters to the controller unit of the Coherent Cube laser heads (445nm, 514nm, 594nm, 685nm).

37 pin D-SUB female connector

Pin #	Description	Cable color
1	Blanking AOTF V_{CC}	black
2	z-piezo V_{CC}	white
3-11	-	-
12	Laser 640nm V_{CC}	brown
13	Laser 640nm Gnd	green/red
14	Laser 561nm V_{CC}	blue/red
15	Laser 561nm Gnd	violet
16	Laser 488nm V_{CC}	green
17	Laser 488nm Gnd	yellow
18	Laser 405nm V_{CC}	grey
19	Laser 405nm Gnd	pink
20	Blanking AOTF Gnd	blue
21	z-piezo Gnd	red
22-37	-	-

Table 8.3 | Pin connection of the 37 pin D-SUB connector attached to the Andor precision control unit.

8.5 Custom Spinning Disk Software

The custom software for the spinning disk software was written in LabVIEW 2015 (National Instruments). The software synchronizes the laser excitation with the exposure of the camera chips and the perfect focus system. This enables the fast, and z-drift free acquisition of image stacks.



Figure 8.3 | User interface of the Spinning Disk software: Top left: camera & laser trigger settings. Bottom left: laser power. Center left: Perfect Focus System control. Center right: trigger scheme of cameras and z-piezo. Right: z-piezo & image stack settings.

The software structure is based on three state machines (program structure that sequentially executes different functions upon an user interaction) and performs all function sequentially in each state machine (Figure 8.4). One state machine controls the Nikon perfect focus system (located on the host computer, Section: 8.5.2) and the second and third (located on the host computer and the field programmable gate array, Section: 8.5.3) operate the video acquisition.

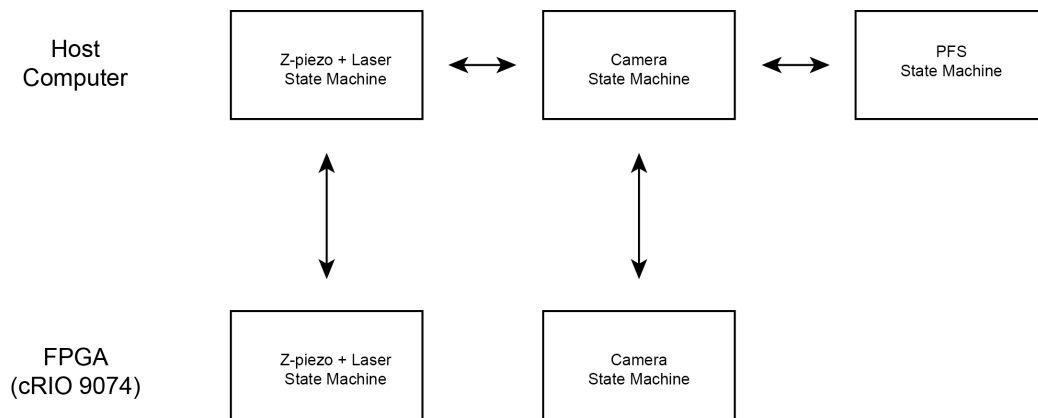


Figure 8.4 | Software Structure of the Spinning Disk program: Rectangular blocks represent state machines, black arrows indicate interstate machine communication on the host computer and between host computer and the FPGA.

8.5.1 Andor Laser Combiner 401

The initialization of the ALC 401 is a two step process. First, the DeVasys microcontroller needs to remove the interlock from all lasers and to open the shutter to allow the laser emission to leave the box. Second, all four laser heads need to be started via ASCII commands over the COM ports.

DeVaSys Controller

This is achieved by calling the following DeVasys dll functions, which set channels B6 and C7 of the DeVasys board to true. This opens the shutter and the interlocks of the laser heads.

Open Device Instance: Opens a handle to the DeVasys Board. Input parameters are the device name (USBI2cIo, String) and the device number (0, U8). Output parameter is the device handle (I32). A 0 at the error output denotes success.

Configure I/O Ports: Selects for all I/O ports of the DeVasys board the state (Input or Output). Input parameters are the device handle (I32) and the U32 representation of a binary array where 0 denotes an input channel configuration and 1 denotes an output channel configuration. The value to switch channel B6 and C7 as output is 294912. A 0 at the error output denotes success.

Write to Output Channels: Sets the output channels to on or off. Input parameters are the device handle (I32), the IO Ports, a U32 representation of a binary array where 0 = off and 1 = on and a second U32 representation of a binary array called channel mask. The channel mask defines, which channels can be changed. 0 = channel state is not overwritten, 1 = channel is overwritten. The default values to switch both channels to true is 540672 for both binary arrays. To switch off the lasers and close the shutter, the IO Ports input has to be set to 0. A 0 at the error output denotes success.

Close Device Instance: Closes the device instance to the DeVasys board. Input Parameter is the device handle (I32). A 0 at the error output denotes success.

Starting The Laser Heads

After the successful remove of the shutter lock, all four laser heads are started in parallel using the following start-up routines. Table 8.4 shows overview over the COM Ports used to communicate with the individual laser heads. Each laser is switched on through a state machine, that iterates through the necessary command - response sequence displayed in the following tables.

Laser Head	Coherent Cube	Coherent Sapphire	Cobolt Jive	Coherent Cube
Wavelength	405nm	488nm	561nm	640nm
Laser Type	diode	OPSL	DPSSL	diode
COM Port	201	202	203	204

Table 8.4 | Laser types, wavelengths and respective COM Ports inside the ALC 401: OPSL: optical pumped semiconductor laser, DPSSL: diode pumped solid state laser

Coherent Cube: Each "Set" command is executed ten times. If the corresponding request command (e.g. Set Prompt and Prompt) does not give the correct response after ten iterations, the state machine stops the execution and outputs an error message.

Step	Write to port	Correct Response	Success	Failure
Init	-	-	Prompt	-
Prompt	?>	>=0	Echo	Set Prompt
Set Prompt	>=0	-	Prompt	-
Echo	?E	E=0	TEC	Set Echo
Set Echo	E=0	-	Echo	-
TEC	?T	T=1	Laser	Set TEC
Set TEC	T=1	-	Set TEC	-
Laser	?L	L=1	Success	Set Laser
Set Laser	L=1	-	Set Laser	-
Success	-	-	-	-
Failure	-	-	-	-

Table 8.5 | Start Up ASCII sequence for the Coherent Cube laser: State Machine command - response sequence to switch on the Coherent Cube laser head.

Coherent Sapphire: Contrary to Coherent Cube laser head (Table 8.5), the command - response architecture of the Coherent Sapphire laser head does not allow an efficient check of the successful execution of each command. Thus, the state machine only checks whether or not the laser was switched on at the last step.

Step	Write to port	Next Step	Executions
Init	-	Set Prompt	-
Set Prompt	≥ 0	Set Echo	10
Set Echo	E=0	Set TEC	10
Set TEC	T=1	Set Laser	10
Set Laser	L=1	Laser	10
Laser	?P	Success or Failure	-
Success	-	-	-
Failure	-	-	-

Table 8.6 | Start Up ASCII sequence for the coherent sapphire laser: State Machine command - response sequence to switch on the Coherent Sapphire laser head.

Cobolt Jive: The Coherent Jive command - response sequence requires only one check, which is executed ten times until failure, similar to the Coherent Cube laser head.

Step	Write to port	Correct Response	Success	Failure
Init	-	-	Interlock	-
Interlock	ilk?	0	Laser	Failure
Laser	l?	1	Success	Set Laser
Set Laser	ll	-	Laser	-
Success	-	-	-	-
Failure	-	-	-	-

Table 8.7 | Start Up ASCII sequence for the Cobolt Jive laser: State Machine command - response sequence to switch on the Cobolt Jive laser head.

8.5.2 Nikon Perfect Focus System

The Nikon Perfect Focus System (PFS) is operated through an ActiveX COM wrapper module, which is provided with the "Nikon TE2000 SDK Server 1.1 Type Library". Two different sets of functions can be called through property or invokes nodes. Both functions use various data types as input and output values.

Property Node Commands:

Property nodes read out the current state of the PFS and output the variant data type, which has to be typecast to U32 bit integers.

Command	Output Values	Description
FaStatus	-1	Status Unknown
FaStatus	1	Autofocus switched off
FaStatus	2	Position over maximum?
FaStatus	3	Position under minimum?
FaStatus	4	Searching for Focus
FaStatus	5	Searching for Focus
FaStatus	10	Searching for Focus
FaStatus	50	Focus found
FaStatus	90	Undefined error
Position	-7 to 189250	Objective Position, 1 Unit = 0.5 μm
OffsetLensPosition	0 to 41600	Offset Lens Position, 1 Unit = 52.9nm
FocusAssistObjective	Objective dependant	If output value = 0, the PFS system is disabled
IsFocusMemorized	0 or 1	Checks if a focus position is memorized in the PFS controller.
IsOffsetMemorized	0 or 1	Checks if a offset lens position is memorized in the PFS controller.

Table 8.8 | List of Property Node PFS commands

Invoke Node Commands:

Invoke nodes execute commands which changes the state of the PFS controller and the microscope.

Command	Input	Output	Description
ControlFocus Assist	FaON	-	Activates the autofocus. Returns an error if the autofocus was already activated.
ControlFocus Assist	FaWait	-	Deactivates the autofocus. Returns an error if the autofocus was already deactivated.
ReadFocus Memory	-	-7 to 189250	Objective position stored in the PFS controller memory. Command only available after objective position data is stored.
ReadOffset Memory	-	0 to 41600	Offset lens position stored in the PFS controller memory. Command only available after offset lens position is stored.
MemorizeFocus Memory	-	-	Stores the current objective position into the PFS controller memory.

Table 8.9 | List of Invoke Node PFS commands

Spinning Disk Confocal Microscope Upgrade

Command	Input	Output	Description
MemorizeOffset Memory	-	-	Stores the current focus lens position into the PFS controller memory.
MoveAbsolute	-7 to 189250	-	Moves the objective to the given absolute position.
MoveAbsolute OffsetLens	0 to 41600	-	Moves the offset lens to the given absolute position.

Table 8.9 continued | List of Invoke Node PFS commands

Perfect Focus System state machine

The perfect focus system embedded into the Nikon Te2002 body consists of several parts. The emission of an infrared led (870nm) is guided over an offset lens and a dichroic mirror into the beam path. The back reflection between the sample and the cover slip surface is guided back through the objective and hits a position sensor. The objective position and therefore the focus position can be adjusted by the position of the offset set prior to the activation of the PFS. Upon activation, a closed feedback loop is constantly adjusting the height of the objective. To emulate the functionality of the manual PFS controller and to integrate an automatic operation, all functions of the PFS system were added to the Spinning Disk software through a state machine, depicted in Fig. 8.5.

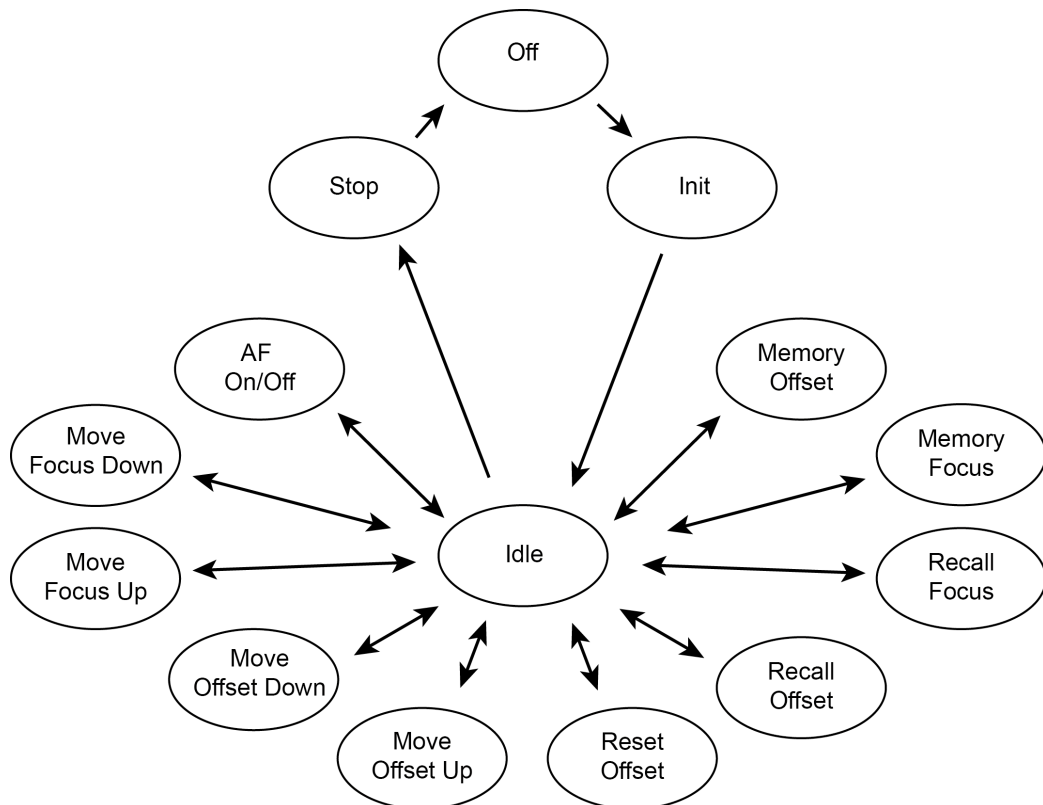


Figure 8.5 | Perfect focus system state machine: The description of each state is given in the following paragraphs.

Off Entry point during program startup. Upon activation of the "Enable PFS" button, the user is prompted to check if the PFS system is powered on. After this confirmation, the state machine switches to the "Init" state. If the PFS system is not powered on and the program proceeds to the "Init" state, the software freezes due to a bug in the Nikon SDK.

Init The program opens the ActiveX connection to the PFS and proceeds to the "Idle" state.

Idle Contains an event based state machine. The timeout case reads out the current status of the PFS controller via the property node commands (Table 8.8) and updates the user interface. Other event cases lead to their individual states.

AF On/Off Reads out a boolean LED on the user interface, which indicates if the focus search is active or not. Depending on the state of this variable, the focus search is enabled or disabled.

Move Focus Down // Move Focus Up Moves the objective to an absolute position given by the sum of the current position and the value on the user interface.

Move Offset Down // Move Offset Up Moves the offset lens to an absolute position given by the sum of the current position and the value on the user interface.

Reset Offset Moves the offset lens to the 0 position and saves the position into the PFS controller memory.

Recall Offset Moves the offset lens to the absolute position saved in the PFS controller memory.

Recall Focus Moves the objective to the absolute position saved in the PFS controller memory.

Memory Focus Saves the current absolute objective position into the PFS controller memory.

Memory Offset Saves the current absolute offset lens position into the PFS controller memory.

Stop Closes the ActiveX connection to the PFS.

8.5.3 Camera, Laser & Z-piezo State Machine

The last two state machines are distributed between the host computer and the field programmable gate array (FPGA) on the compact RIO system. The host part provides a user interface and saves timing data. The FPGA generates analogue and digital signals for the hardware control. Data transfer between Host and the compact RIO system is achieved by using a variable cluster (Table 8.10) and an enumeration constant containing all possible states of both state machines (Fig. 8.6, Idle, Record, Enable Camera & Stop).

Description	Variable Name	Data Type
Laser power 405nm laser	ALC 400 Channel 1 [V]	FXP 20,5
Laser power 488nm laser	ALC 400 Channel 2 [V]	FXP 20,5
Laser power 561nm laser	ALC 400 Channel 3 [V]	FXP 20,5
Laser power 640nm laser	ALC 400 Channel 4 [V]	FXP 20,5
Laser power 445nm laser	Custom Box Channel 1 [V]	FXP 20,5
Laser power 514nm laser	Custom Box Channel 2 [V]	FXP 20,5
Laser power 594nm laser	Custom Box Channel 3 [V]	FXP 20,5
Laser power 685nm laser	Custom Box Channel 4 [V]	FXP 20,5
Selects Laser for Camera 1	Laser Camera 1	Menu Ring
Selects Laser for Camera 2	Laser Camera 2	Menu Ring
Selects Laser for Camera 3	Laser Camera 3	Menu Ring
Photoactivation Laser	Laser Photoactivation	Menu Ring
z-Piezo Position	Z-Piezo Position [V]	FXP 20,5
Startpoint of the image stack	Z-Piezo Position Start Position Ramp [V]	FXP 20,5
Incremental distance	Z-Piezo Increment Ramp [V]	FXP 20,5
# of slices per image stack	Z-Stack increments	I32
# of z stacks	# of z stacks	I32
Exposure Time of the camera chip.	Exposure Time Camera [ms]	U32
Time to transfer the image to the readout area of the chip (and readout if Frame transfer is off)	Frame Transfer Time Camera [ms]	U32
Photoactivation time.	Photoactivation Time [ms]	U32

Table 8.10 | Communication variables between FPGA and Host Computer

Additional variables are used to read out the current Z Stack (U32), select the frame transfer mode (Enum) and to control the PFS system (Enum x 2).

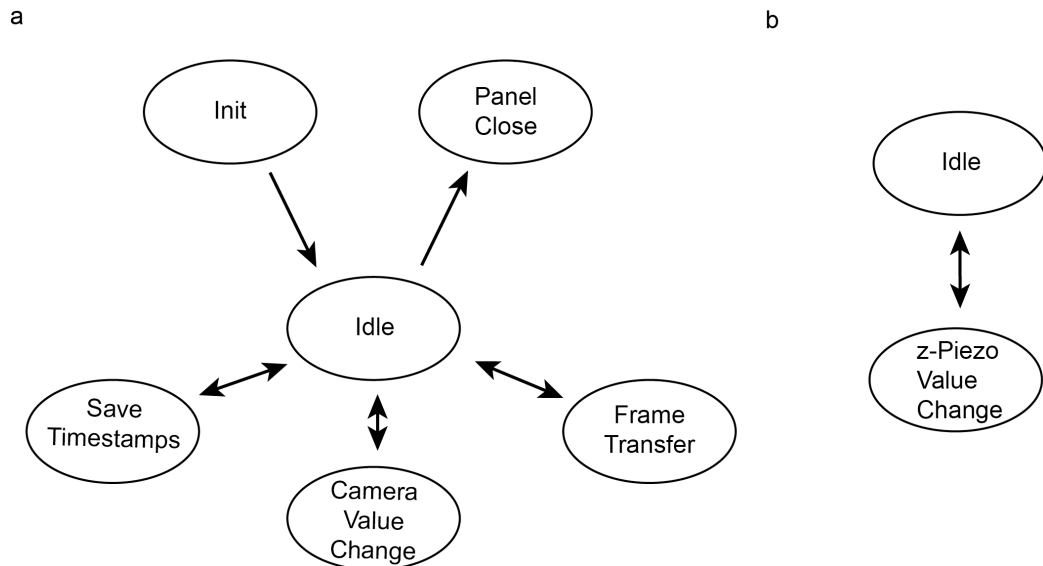


Figure 8.6 | State machines operating motion along the optical axis, camera and laser triggering: a) Camera state machine. b) z-Piezo + laser state machine.

Camera State Machine

Init Initializes the Andor laser combiner 401 (Section: 8.5.1) and then proceeds to the idle state.

Idle The idle state uses an event structure to wait for any user interaction from the front panel.

Frame Transfer Upon a change in the frame transfer mode of the camera, the user interface is updated to show the correct trigger scheme and settings for the camera acquisition software Andor Solis. The frame transfer time is set to 4ms (instead of the minimum of 2.7ms) and used to move the z-piezo to the new position.

Camera Value Change Upon a change of the camera control cluster on the user interface, different modes are triggered. If neither the "Record video" or "Enable Cameras" buttons were pressed, the trigger scheme on the

user interface gets updated using the new acquisition parameters. If "Enable Cameras" is pressed, all 3 cameras are triggered externally and the user is able to change the position of z-piezo and to adjust the laser power over the z-piezo and laser state machine (Fig. 8.6 b).

If the user presses the record button, the programmed recording scheme is executed. When the Nikon PFS is disabled, the image stack sequence runs continuously until the specified number of stacks is reached or the user cancels the sequence. Figure 8.7 shows the trigger scheme for the cameras and the laser with frame transfer enabled (a) or disabled (b) .

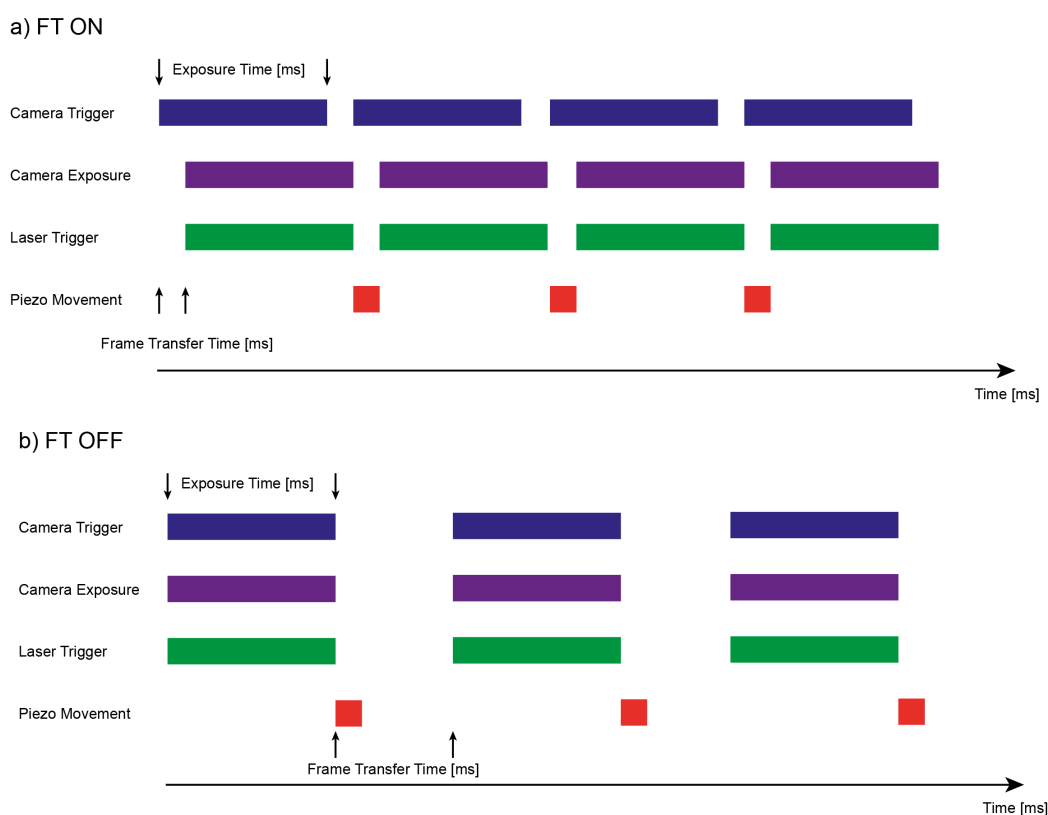


Figure 8.7 | Camera acquisition modes: a) Frame transfer enabled: leads to a quasi continuous exposure of the camera chip. The z-piezo movement falls into the frame transfer window to avoid imaging artifacts caused by the movement. b) Frame transfer disabled: Increases the frame transfer window by $\sim 35\text{ms}$ (depending on the camera model). Similar to case a), the piezo movement is placed inside the frame transfer window.

If the experiment is performed over long periods of time, it may become necessary to activate the Perfect Focus System to correct for z-drift in between

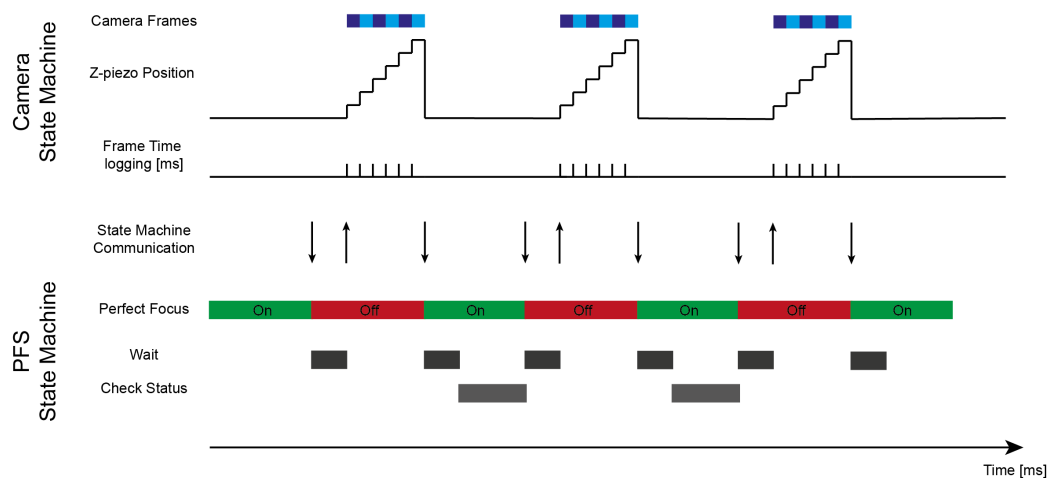


Figure 8.8 | Hardware synchronization: Synchronization between the camera, the piezo and the perfect focus system.

image stacks or if the sample temperature in the beginning of the experiment is lower than the target temperature of the sample heating stage. The software allows the user to activate the PFS every n^{th} image stack. This operation mode prevents unnecessary delays due to the lock-in time of the PFS module if the drift is small. Figure 8.8 shows the operation sequence and communication between the perfect focus state machine (Section: 8.5.2) and the camera state machine.

After the recording sequence has been started, the PFS is switched off and the program waits for 750ms (delay time until PFS is safely switched off). The Camera state machine starts the recording of the image stack by acknowledging an interrupt on the FPGA. Once the image stack is recorded, the FPGA finishes a loop and pauses at the same interrupt. The Camera state machine waits for the interrupt signal from the FPGA and switches the PFS on. After a waiting period of 750ms, the software checks the PFS status until the focus position has been reacquired and then deactivates the PFS. After another waiting period (750 ms), the next image stack is acquired. At the end of the image sequence, the PFS is switched on and the camera state machine returns to the idle state.

Save Timestamps Due to the deterministic operation mode of the FPGA, it is usually not necessary to acquire time stamps for each frame. However, the operation of the PFS is a non-deterministic process, which is biased through several delay times (e.g. lock-in time and communication overhead between host and PFS controller). Hence it is necessary to record the starting

Spinning Disk Confocal Microscope Upgrade

point of each frame. By pressing the "Save Timestamps" button, the user can save the frame time stamps from the previous acquired image stack.

Panel Close The panel close state is entered when exiting the program. The state closes the safety shutter from the ALC 401 and switches off all four laser modules.

8.6 Component List

Microscopy Body + Detection Path

Description	Component	Manufacturer
Microscope Body	TE 2000	Nikon
Perfect Focus System	T-PFC	Nikon
Microscope Controller	T-RCP	Nikon
Spinning Disk Unit	CSU-10	Yokogawa
Microscope Stage	ProScan2	Prior
Z-piezo stage & controller	NanoscanZ	Prior
EMCCD camera	Andor Ixon	Andor

Table 8.11 | Microscope body and detection path components

Laser Box

Description	Component	Manufacturer
Laser Head	Cube 445nm	Coherent
Laser Head	Cube 514nm	Coherent
Laser Head	Cube 594nm	Coherent
Laser Head	Cube 685nm	Coherent
Laser Control Box	Scientific Control	Coherent
Single mode fiber	QPMJ-3A3U-405/650-3/125-3-5-1	OZ Optics
Mirror	Silver Mirror	Thorlabs
Dichroic	zt 633 rdc	AHF
Dichroic	zt 543 rdc	AHF
Dichroic	zt488 rdp	AHF
Dichroic	405/488/561/640 rpc	AHF
Fast Collimator / Coupler	60FC-4-RGBV11-47	Schäfter & Kirchhoff

Table 8.12 | Laser Box Components

ALC 401

Description	Component	Manufacturer
Laser Head	Cube 405nm	Coherent
Laser Head	Sapphire 488nm	Coherent
Laser Head	Jive 561nm	Cobolt
Laser Head	Cube 640nm	Coherent
Microcontroller operating the ALC 401	USB-I2C/IO	DeVaSys
Single mode fiber	QPMJ-3AF3S-400-3/125-3AS-3-1	OZ Optics

Table 8.13 | Andor Laser Combiner 401

Hardware Control

Description	Component	Manufacturer
Real-time embedded system	cRIO 9074	National Instruments
Digital I/O Module	NI 9402	National Instruments
Analogue Output Module	NI 9263	National Instruments
Analogue Output Module	NI 9269	National Instruments
PCI interface cards for EMCCD cameras	Andor PCI Cards	Andor
Analogue Output PCI Card (Used with Andor IQ)	PCIM-DDA06/16	Measurement Computing

Table 8.14 | Hardware Control Components

Chapter 9

Conclusion & Summary

In this work, I presented the assembly and programming of a 3D orbital tracking microscope with nanometer localization precision and millisecond temporal resolution. The previously used tracking software to control a former version of the microscope only offered a limited amount of features and could not be further modified to add new functionalities (e.g. long range tracking, microscope synchronization etc.). In addition, the software was developed for a normal personal computer, which intrinsically is not able to perform the necessary calculations of the tracking algorithm with precise sub-millisecond timing. To overcome these problems, I developed a new tracking software. This self-written software is executed on a combination of a deterministic processing unit (a combination of a real-time CPU and a field programmable gate array, short FPGA) and allows the synchronized operation of all microscopy components on the microsecond timescale. The development of two new optional tracking features (long-range tracking and dark orbits) increased the available tracking area to the centimeter range and allows the tracking of dim particles by trading acquisition speed for a decreased photo-bleaching rate, thus significantly extending the trajectory length. A recent update of the tracking software included the option to operate the wide-field and tracking microscopes from the same user interface, providing a real-time visualization of the particle location in context of the environment and the ability to perform dual-color tracking experiments.

Currently, the real-time CPU of the deterministic processing unit is able to calculate the new particle location within a few hundred μs . This means that, for orbit times on the order of a few milliseconds, the real-time CPU is idle approximately 90% of time. This still available processing power of the high-end deterministic unit can be used to implement additional features into tracking software. One possibility could include real-time analysis

capabilities, which could detect temporal variances in the particle behavior (e.g. pauses, directionality or velocity changes) and modify the behavior of the tracking algorithm. For example the acquisition rate, the number of dark orbits or photo-activation events during the tracking process. Together with recent developments in optogenetic actuators, the orbital tracking approach will give access to a new type of experiment, which allows the manual or automatic modification of the local behavior inside a specimen with unprecedented spatiotemporal accuracy.

The development of a novel correlation based analysis approach added a fast and reliable tool to classify three-dimensional single-particle tracking data into segments of active transport and passive phases, where no or Brownian motion occurs. The performance analysis of the algorithm showed recovery rates of $> 90\%$ for the two dimensional and $> 95\%$ for the three dimensional analysis mode. Even for low "signal-to-noise" ratios (in this case defined as the displacement per orbit divided by the localization precision), the correlation approach is able to assign up to $> 80\%$ of all data points to the correct type of motion. Further analysis steps can be applied to discriminate between active motion, which can operate at different speeds and directions or to separate passive phases into localization noise and Brownian motion. In the current development step, the correlative analysis required simulations to determine the optimal analysis parameters. To remove the need for simulations and to further increase the usability of this analysis for various data sets, an iterative procedure can be added. The iterative process together with a set of optimization criteria can be used to calculate the optimal analysis parameters. Criteria for this process could include the displacement per orbit or travel distance of active transport, which will converge upon reaching the optimal settings for the analysis.

In the first application I presented, a combination of the orbital tracking method and a correlative imaging approach was able to generate new insights into lysosomal transport along microtubule intersections. Beside the localization of single lysosomes inside a BSC-1 cells, I showed that it is possible to measure the structure of individual microtubules by utilizing the photo-bleaching of GFP molecules along the microtubule strand. Although the combination of both methods provided new informations, several technical limits exist, which prevent a further examination of the underlying transport mechanism. The previously described technical improvements of the tracking microscope will give access to dual-color tracking experiments, which will allow a simultaneous measurement of the position of the particle of interest and to reconstruct the local three dimensional structure of the cytoskeleton

in real-time. The higher acquisition rates (compared to the correlative imaging method), the possibility to photo-manipulate individual particles and the ability to analyze particle shapes and microtubule orientation will allow one to investigate the influence of motors on transport mechanism inside living cells with high spatiotemporal precision.

The second set of experiments in this thesis is the first *in vivo* application of a feedback based three-dimensional single-particle tracking method. The operation modes of the tracking software, namely the long-range tracking and dark orbits enabled us to bridge the gap between motors stepping in the nano-domain, which propel organelles over distance of many hundred microns. Using photoactivation, we were able to follow individual mitochondria in the highly crowded stem axon of rohon-beard sensory neurons inside zebrafish-embryos. The exceptional spatiotemporal accuracy of the orbital tracking approach allowed us to identify two previously unknown types of motion and place them into the context of mitochondrial transport. The simultaneously acquired wide-field images enabled us to investigate the influence of obstacles (stationary mitochondria) on moving mitochondria. The acquired experimental data provides knowledge about the mitochondrial transport in healthy organisms and can be further used to study models for diseases like dementia or amyotrophic lateral sclerosis (ALS).

The informations obtained during the programming of the orbital tracking system showed the supremacy of operating microscope systems through a field programmable gate array. Using this knowledge, I developed a hard- and software upgrade for a commercial spinning disk confocal microscope system. The addition of a new EMCCD camera and four additional laser lines increased the flexibility of the system. It is now possible to excite fluorophores over the whole visible spectrum and to simultaneously acquire confocal images and z-stacks for three independent channels and can be further expanded by implementing options for alternating or arbitrary excitation patterns.

In summary, 3D orbital tracking is a highly-advanced single particle tracking technique that can be applied into *in vitro* systems, cells or ultimately in living organisms with nanometer precision and millisecond temporal resolution. The technical upgrades and applications I presented in this thesis provide the foundation for multidimensional (spatial, spectral and temporal) single-particle tracking experiments, which also offer the possibility to manipulate individual particles in a highly crowded environment.

Chapter 10

Materials and methods

10.1 3D Orbital Tracking Microscope

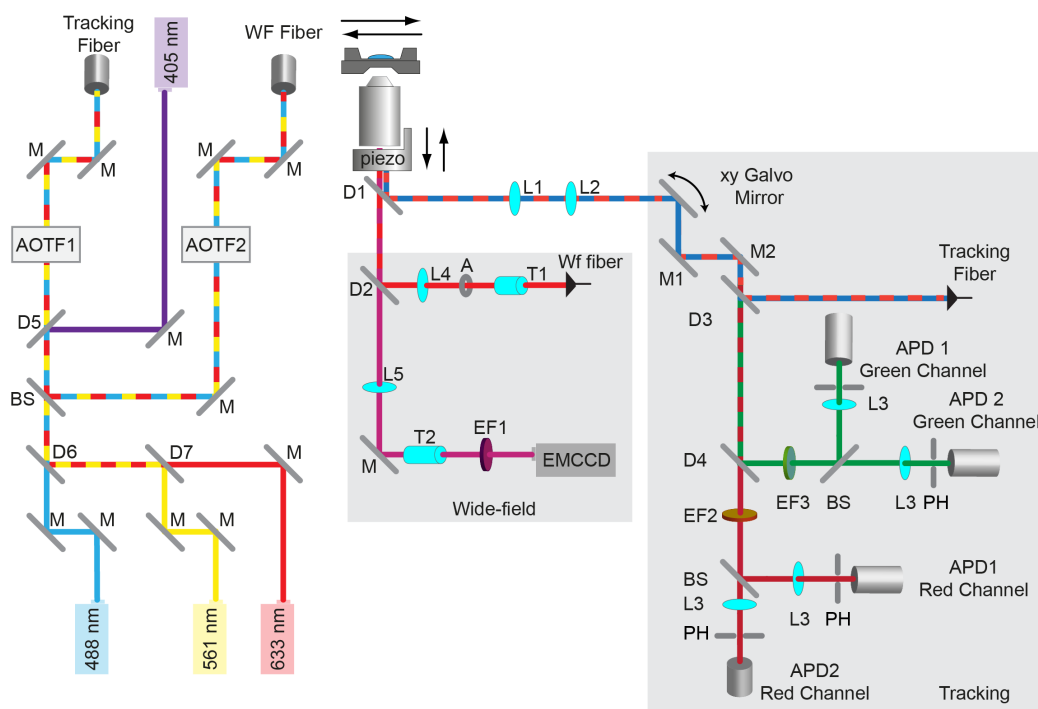


Figure 10.1 | 3D Orbital Tracking microscope schematic: D: Dichroic mirror, M: silver mirror, EF: emission filter, BS: 50/50 beam-splitter, PH: pinhole, L: lens, T: telescope, APD: avalanche photo diode

10.1.1 Microscope Body

Description	Component	Manufacturer
Microscope Body	Axiovert 200	Zeiss
Microscope state	Scan IM 120 x 100	Märzhäuser Wetzlar
Sample & objective heater	Tempcontrol 37-2	Pecon
Objective	Plan Apo VC 60x/1.20WI	Nikon
Z-objective piezo	Mipos 100PL Cap	Piezosystems Jena
XYZ piezo stage	P-527.3-CL	Physik Instrumente
Scan lens	AC254-80-A	Thorlabs
Tube lens	AC254-250-A	Thorlabs
Dichroic	Silver Mirror	AHF
Dichroic	Q550 SPXR	AHF
Dichroic	zt532rdc	AHF
Dichroic	50R/50T	AHF
Dichroic	70R/30T	AHF

Table 10.1 | Microscope Body Components: Optical elements contained in the Axiovert 200 microscope body, Fig. 10.1.

10.1.2 Widefield Path

Description	Component	Manufacturer
EMCCD Camera	Ixon Ultra	Andor
Single-mode fiber	QPMJ-A3A,3AF-488-3.5/125-3-5-1	Oz Optics
Collimator	60FC-4-RGBV11-47	Schäfter & Kirchhoff
Excitation Aperture	Square aperture	-
Lens 1 beam expander	AC254-050-A	Thorlabs
Lens 2 beam expander	AC254-150-A	Thorlabs
Focus lens (onto back aperture)	AC254-400-A	Thorlabs
Quad band dichroic	zt405/488/561/640rpc	AHF
Tube lens	200mm achromatic lens	Thorlabs
Emission aperture	Square aperture	-
Lens 1 image expander	AC254-050-A	Thorlabs
Lens 2 image expander	AC254-150-A	Thorlabs
Emission filter	525/40 Brightline HC	AHF
Emission filter	593/40 Brightline HC	AHF
Emission filter	695/100 ET Bandpass	AHF

Table 10.2 | Wide-field Microscope Components: Optical elements contained in the wide-field microscope, Fig. 10.1.

10.1.3 Confocal Path

Description	Component	Manufacturer
Single mode fiber	QPMJ-A3A,3A-405/650-3/125-3-5-1	Oz Optics
Collimator	60FC-4-RGBV11-47	Schäfter & Kirchhoff
Silver Mirror	PF10-03-P01	Thorlabs
Galvano mirrors	6310H	Cambridge Technologies
Telescope lens 1, f=80mm	AC254-080-A	Thorlabs
Telescope lens 2, f=250mm	AC254-250-A	Thorlabs
Quad band dichroic	zt405/488/561/640rpc	AHF
Dichroic mirror	H 560 LPXR superflat	AHF
Emission filter green	525/50 Brightline HC	AHF
Emission filter red	593/40 Brightline HC	AHF
Emission filter red	685/70 ET Bandpass	AHF
Beamsplitter	50R/50T Strahlenteiler VIS	AHF
"Pinhole" focus lens green	AC254-050-A	Thorlabs
"Pinhole" focus lens red	AC254-075-A	Thorlabs
Multimode fiber ("Pinhole")	M42L01	Thorlabs
Blue detectors	Count 100B	Laser Components
Red detectors	SPCM-CD 3017	Perkin Elmer

Table 10.3 | Confocal Microscope Components: Optical elements contained in the confocal microscope, Fig. 10.1.

10.1.4 Laser Box

Description	Component	Manufacturer
405nm Laser (100mW)	0405-06-01-0100-100	Cobolt
488nm Laser (20mW)	Sapphire	Coherent
561nm Laser (50mW)	MDPL 561-50	Cobolt
HeNe 633nm Laser	25-LHP-151-230	Melles Griot
Acousto optical tun- able filter	TF525-250-6-3-GH19A	Gooch & Housego
Fiber coupler	-	Schäfter & Kirchhoff
Dichroic mirror	600nm longpass	AHF
Dichroic mirror	545nm longpass	AHF
Dichroic mirror	500nm shortpass	AHF
Dichroic mirror	445nm longpass	AHF
Beamsplitter	70R/30T	AHF

Table 10.4 | Laser Box Components: Optical elements contained in the laser box, Fig. 10.1.

10.1.5 Electronics

Description	Component	Manufacturer
Real-time embedded system	cRIO 9082	National Instruments
Digital I/O module	NI 9402	National Instruments
Analogue output module	NI 9263	National Instruments
Objective piezo controller	NV 40/1 CL	Piezosystems Jena
Microstage controller	LStep	Lang
Piezostage controller	E802 / E801 / E500	Physik Instrumente
Galvo mirror controller	673 servo driver	Cambridge Technologies
Galvo mirror PSU	EA-PS 3032-10B	Elektro-Automatik
AOTF controller	MSD040-150-0.2ADM-A5H-8x1	Gooch & Housego

Table 10.5 | Electrical Components: Electrical components to control the microscope system, Fig. 10.1.

10.2 Zebrafish Experiments

Preparation, labeling and drug treatment of zebrafish embryos were developed and performed by Dr. Gabriela Plucińska and Rachel Thong in the Group of Prof. Thomas Misgeld, Technical University Munich.

Animals

For all tracking experiments a mutant zebrafish line (Roy) with impaired production of silver pigment [121] was crossed with a transgenic driver line *Isl2b:Gal4* (kept at a heterozygous background Roy +/-). This line contains a specific promoter that drives expression of the Gal4 transcription factor in zebrafish sensory neurons [122]. Fish were maintained, mated, and raised as previously described [123]. Embryos were kept in 0.3x Danieau's solution at 28.5°C and the development of each embryo was controlled using [124] as reference. No randomization or blinding in the selection of zebrafish embryos was used. All experiments with zebrafish larvae were performed in accordance with institutional and government regulations.

Labeling constructs, screening and mounting

Mitochondrially targeted responder constructs were generated by replacing CFP in the pECFPmito vector with the following fluorescent proteins: TagRFP-T (gift from Martin Meyer, UCL, London, UK), PAGFP (a kind gift from Jennifer Lippincott-Schwartz) or Dendra2-C (#FP821, Evrogen). Next, the *mitoTagRFP-T*, *mitoPAGFP* and *mitoDendra* fragments were cloned down-stream of a 14-mer UAS Gal4 binding sequence fused to the fish basal promoter E1b. To label microtubule plus end tips, PCS2 EB3-GFP was used (PCS2 EB3-GFP was a kind gift from Brian Link, Medical College of Wisconsin). The EB3-GFP fragment was cloned down-stream of a 14-mer UAS Gal4 binding sequence fused to a fish basal promoter E1b. To achieve mosaic labeling, UAS constructs were co-injected (each at a concentration of 10ng/μl) into fertilized eggs of the *Isl2b:Gal4* x Roy fish as described before [125]. At 24 hours post-fertilization (hpf), embryos were transferred to 1% N-phenylthiourea (PTU) to inhibit pigmentation. At 2dpf, chorion was manually removed and embryos were anesthetized using tricaine (at a final concentration of 0.75mM) and embedded in low melting agarose (0.7 – 0.8%, Sigma) for screening. Embryos showing a suitable expression pattern (*mitoTagRFP-T* expressed in isolated sensory neurons in the tail fin) were removed from agarose and allowed to recover in PTU solution overnight. On the next day, they were again anesthetized and mounted in

agarose for imaging as described previously [125]. PTU/Tricaine remained present throughout the experiment. When using photosensitive proteins such as PAGFP or Dendra 2, embryos were maintained in a dark environment and mounted under a dissection microscope with blue light excluding filters.

Drug treatment

To investigate which type of motional behavior is dependent on microtubules, experiments in the presence of a microtubule-destabilizing drug, nocodazole were performed. Two hours prior to imaging, the medium was replaced with PTU/Tricaine solution containing 1% DMSO and 400nM nocodazole. Control embryos were maintained in medium containing 1% DMSO only. To ensure that the concentration of nocodazole disrupts microtubule growth, the plus ends were labeled with EB3-GFP and microtubule tip dynamics were imaged before and after nocodazole treatment on an upright wide-field fluorescence microscope (Olympus BX51W1) equipped with a 40x/0.8NA water dipping objective (Nikon) and a cooled CCD camera (SensiCam, Pco Imaging). Five minutes movies were taken at a frame rate of 1Hz and revealed the presence of microtubule comets. Treatment with 400nM nocodazole as described above strongly reduced the EB3-GFP dynamics.

3D tracking and wide-field imaging

At 3dpf, selected larvae positive for mitoTagRFP-T were prepared for imaging. Larvae were mounted in low melting agarose in glass-bottom petri dishes. During the experiment, the temperature was maintained at 25° to decrease drift along the z-axis. Each fish was screened for the expression of mitoPAGFP prior to the experiment by photoconverting a small subset of mitochondria outside the region of interest. Once embryos positive for PAGFP were identified, individual mitochondria were activated with blue light using a xy scanning pattern (405nm, 80 μ W measured before the objective; 34.6 x 34.6 μ m², i.e. 256x256 pixels of 135x135nm² per pixel; 30 μ s pixel dwell time). Activated mitochondrion were tracked in the green channel (488nm excitation) with an acquisition speed of 100 Hz (a 5ms orbit + one 5ms dark orbit) and simultaneously observed via the wide-field microscope in the red channel (561nm excitation, 2 Hz). The count rate was stabilized manually at approximately 500 photons per orbit by adjusting the laser power during the experiment to achieve a constant localization precision of < 5 nm in xy and ~30 nm in z. The laser power ranged from < 1 μ W at the beginning of the measurement to up to 25 μ W (measured before the objective) at the end of an experiment. The feedback loop for the long-range tracking was ac-

tivated every time a mitochondrion traveled further than 10 μm away from the center of the tracking area. Mitochondria were tracked until the intensity counts fell beneath the background threshold level (adjusted individually for each fish). In total, 43 trajectories from 16 individual untreated zebrafish larvae, 37 trajectories from 13 larvae treated with 1% DMSO and 34 trajectories from 11 larvae treated with 1% DMSO and 400 nM Nocodazole were collected. Trajectories where the algorithm was switching between different mitochondria during the experiment were discarded.

Repetitive tracking

To investigate the propensity of mitochondria to pause at particular locations along an axon, the motion of several mitochondria along the same region of a neurite was measured. For these experiments, selected larvae positive for mitoDendra2 and mitoTagRFP-T were prepared for imaging at 3dpf as described above. A stretch of a neurite (approximately 35 μm) was repeatedly irradiated using a confocal scan and 405 nm excitation (80 μW measured before the objective; 34.6 x 34.6 μm^2 , i.e. 256x256 pixels of 135x135 nm^2 per pixel; 30 μs pixel dwell time) to convert mitoDendra2 from green to red. Any new mitochondria entering the photoconverted region were tracked (100 Hz, a 5ms orbit + one 5ms dark orbit) using 488nm excitation until they either left the field-of-view or were fully photoconverted from the 488nm excitation laser to red fluorescence and thus could no longer be tracked in the green channel. After each recorded trajectory, a 405 nm scan was repeated to erase any residual or reemerging fluorescence. Simultaneous wide-field observation was only possible for the first trajectory due to the high rates of mitoTagRFP-T bleaching caused by the UV laser. In total, we recorded 50 trajectories from 3 neurons (3 embryos).

10.3 Tracking in BSC-1 Cells

Cell Culture

The utilized cell line was stably transfected by the lab of Prof. Lakadamyali, ICFO Institute, Barcelona, Spain.

A double stably transfected cell line for GFP-Tubulin and LAMP2-mCherry (Lgp120NL-mCherry) was obtained by transfecting the plasmid pHyg-LGP120NL-mCherry on top of the stably transfected cell line BS-C-1 GFP-Tubulin. This plasmid was constructed using as backbone the hygromycin resistance pcDNA5/FRT/TO Vector. The cassette LAMP2-mCherry (LGP120NL-mCherry) was generated from plasmid LGP120NL-PA-GFP, modified by replacing the PA-GFP with mCherry cloned in frame using BamHI/XbaI restriction sites. This cassette was then amplified by PCR and cloned into the pcDNA5/FRT/TO vector using NheI/EcoRV restriction sites. The integrity of all these constructs was assessed by direct sequencing. BS-C-1 GFP-Tubulin stably transfected cell line was transfected with plasmid pHyg-LGPNL-mCherry and single clones were selected by adding Hygromycin B ($100 \mu\text{g}/\text{mL}$) to the cell culture medium. This double stably transfected cell line was maintained in culture using a complete growth medium (Minimum Essential Medium Eagle with Earle's salts with nonessential amino acids supplemented with 10% (v/v) FBS, 2 mM L-glutamine, 1 mM sodium pyruvate and penicillin-streptomycin to prevent bacterial contaminations). Cell cultures were incubated at 37°C with 5% carbon dioxide. In order to ensure the stability of both plasmids $500 \mu\text{g}/\text{mL}$ of Geneticin (G418 Sulfate) (Invitrogen 10131035) and $100 \mu\text{g}/\text{mL}$ Hygromycin B (Invitrogen 10687010) were added to the culture medium.

Lysosome & tubulin tracking

BSC-1 cells stably expressing GFP-tubulin and LAMP2-mCherry were prepared in 8 well slides (80000 cells, Labtek II, Thermo Scientific). During the measurements, cells were maintained in phenol red free complete growth medium containing 120 nM paclitaxel and 120 nM nocodazole solution added into the imaging medium as previously described. Orbital tracking was done at 25°C , 5 ms time resolution and a laser power of $< 10 \mu\text{W}$ (561 nm) before the objective for imaging of the LAMP2-mCherry endolysosome tracking and $< 10 \mu\text{W}$ (488 nm) before the objective for imaging of the GFP-tubulin microtubules.

Bibliography

- [1] R. Hooke, “Micrographia,”
- [2] E. Abbe, “Beiträge zur Theorie des Mikroskops und der mikroskopischen Wahrnehmung,” *Archiv für Mikroskopische Anatomie*, vol. 9, no. 1, p. 413, 1873.
- [3] J. Enderlein, “Tracking of fluorescent molecules diffusing within membranes,” *Applied Physics B*, vol. 71, no. 5, p. 773, 2000.
- [4] A. Einstein, “Zur quantentheorie der strahlung.,” vol. 18, p. 121.
- [5] J. P. Gordon, H. J. Zeiger, and C. H. Townes, “The Maser—New Type of Microwave Amplifier, Frequency Standard, and Spectrometer,” *Physical Review*, vol. 99, no. 4, p. 1264, 1955.
- [6] T. H. Maiman, “Stimulated Optical Radiation in Ruby,” *Nature*, vol. 187, no. 4736, p. 493, 1960.
- [7] A. JABŁOŃSKI, “Efficiency of Anti-Stokes Fluorescence in Dyes,” *Nature*, vol. 131, no. 3319, p. 839, 1933.
- [8] M. Born and R. Oppenheimer, “Zur Quantentheorie der Molekeln,” *Annalen der Physik*, vol. 389, no. 20, p. 457, 1927.
- [9] M. Kasha, “Characterization of electronic transitions in complex molecules,” *Discussions of the Faraday Society*, vol. 9, p. 14, 1950.
- [10] G. G. Stokes, “On the change of refrangibility of light.,” vol. 142, pp. 463–562.
- [11] M. Orm, A. B. Cubitt, K. Kallio, L. A. Gross, R. Y. Tsien, and S. J. Remington, “Crystal Structure of the *Aequorea victoria* Green Fluorescent Protein,” *Science*, vol. 273, no. 5280, p. 1392, 1996.

- [12] O. SHIMOMURA, F. H. JOHNSON, and Y. SAIGA, “Extraction, purification and properties of aequorin, a bioluminescent protein from the luminous hydromedusan, *Aequorea*.” *Journal of cellular and comparative physiology*, vol. 59, pp. 223–239, June 1962.
- [13] D. C. Prasher, V. K. Eckenrode, W. W. Ward, F. G. Prendergast, and M. J. Cormier, “Primary structure of the *Aequorea victoria* green-fluorescent protein,” *Gene*, vol. 111, no. 2, p. 229, 1992.
- [14] M. Chalfie, Y. Tu, G. Euskirchen, W. W. Ward, and D. C. Prasher, “Green fluorescent protein as a marker for gene expression.” *Green Fluorescent Protein*, vol. 263, pp. 802–805, Feb. 1994.
- [15] R. Heim, A. B. Cubitt, and R. Y. Tsien, “Improved green fluorescence,” *Nature*, vol. 373, pp. 663–664, Feb. 1995.
- [16] F. Yang, L. G. Moss, and G. N. Phillips, “The molecular structure of green fluorescent protein,” *Nature Biotechnology*, vol. 14, no. 10, p. 1246, 1996.
- [17] M. Orm, A. B. Cubitt, K. Kallio, L. A. Gross, R. Y. Tsien, and S. J. Remington, “Crystal Structure of the *Aequorea victoria* Green Fluorescent Protein,” *Science*, vol. 273, no. 5280, p. 1392, 1996.
- [18] W. Tomosugi, T. Matsuda, T. Tani, T. Nemoto, I. Kotera, K. Saito, K. Horikawa, and T. Nagai, “An ultramarine fluorescent protein with increased photostability and pH insensitivity,” *Nature Methods*, vol. 6, pp. 351–353, Apr. 2009.
- [19] T. T. Yang, L. Cheng, and S. R. Kain, “Optimized codon usage and chromophore mutations provide enhanced sensitivity with the green fluorescent protein,” *Nucleic Acids Research*, vol. 24, pp. 4592–4593, Nov. 1996.
- [20] T. Nagai, K. Ibata, E. S. Park, M. Kubota, K. Mikoshiba, and A. Miyawaki, “A variant of yellow fluorescent protein with fast and efficient maturation for cell-biological applications,” *Nature Biotechnology*, vol. 20, pp. 87–90, Dec. 2001.
- [21] N. C. Shaner, M. Z. Lin, M. R. McKeown, P. A. Steinbach, K. L. Hazelwood, M. W. Davidson, and R. Y. Tsien, “Improving the photostability of bright monomeric orange and red fluorescent proteins,” *Nature Methods*, vol. 5, pp. 545–551, May 2008.

- [22] D. Yu, M. A. Baird, J. R. Allen, E. S. Howe, M. P. Klassen, A. Reade, K. Makhijani, Y. Song, S. Liu, Z. Murthy, S.-Q. Zhang, O. D. Weiner, T. B. Kornberg, Y.-N. Jan, M. W. Davidson, and X. Shu, “A naturally monomeric infrared fluorescent protein for protein labeling in vivo.,” *Nature Methods*, vol. 12, pp. 763–765, June 2015.
- [23] G. H. Patterson and J. Lippincott-Schwartz, “A photoactivatable GFP for selective photolabeling of proteins and cells.,” *Science*, vol. 297, pp. 1873–1877, Sept. 2002.
- [24] N. G. Gurskaya, V. V. Verkhusha, A. S. Shcheglov, D. B. Staroverov, T. V. Chepurnykh, A. F. Fradkov, S. Lukyanov, and K. A. Lukyanov, “Engineering of a monomeric green-to-red photoactivatable fluorescent protein induced by blue light.,” *Nature Biotechnology*, vol. 24, pp. 461–465, Mar. 2006.
- [25] A. Köhler, *Ein neues Beleuchtungsverfahren für mikrophotographische Zwecke*. 1893.
- [26] M. Minsky, “Microscopy apparatus.”
- [27] G. B. Airy, *On the diffraction of an object-glass with circular aperture*, vol. 5. 1835.
- [28] Rayleigh, “XXXI. Investigations in optics, with special reference to the spectroscope ,” *Philosophical Magazine Series 5*, vol. 8, no. 49, p. 261, 1879.
- [29] M. J. Rust, M. Bates, and X. Zhuang, “Sub-diffraction-limit imaging by stochastic optical reconstruction microscopy (STORM),” *Nature Methods*, vol. 3, no. 10, p. 793, 2006.
- [30] T. Dertinger, R. Colyer, G. Iyer, S. Weiss, and J. Enderlein, “Fast, background-free, 3D super-resolution optical fluctuation imaging (SOFI).,” *Proceedings of the National Academy of Sciences*, vol. 106, pp. 22287–22292, Dec. 2009.
- [31] S. W. Hell and J. Wichmann, “Breaking the diffraction resolution limit by stimulated emission: stimulated-emission-depletion fluorescence microscopy.,” *Optics letters*, vol. 19, pp. 780–782, June 1994.
- [32] D. Magde, E. Elson, and W. W. Webb, “Thermodynamic Fluctuations in a Reacting System - Measurement by Fluorescence Correlation Spectroscopy,” *Physical Review Letters*, vol. 29, no. 11, p. 705, 1972.

- [33] Y. H. Foo, N. Naredi-Rainer, D. C. Lamb, S. Ahmed, and T. Wohland, “Factors Affecting the Quantification of Biomolecular Interactions by Fluorescence Cross-Correlation Spectroscopy,” *Biophysical Journal*, vol. 102, no. 5, p. 1174, 2012.
- [34] T. Förster, “Zwischenmolekulare Energiewanderung und Fluoreszenz,” *Annalen der Physik*, vol. 437, no. 1-2, p. 55, 1948.
- [35] A. Röhl, D. Wengler, T. Madl, S. Lagleder, F. Tippel, M. Herrmann, J. Hendrix, K. Richter, G. Hack, A. B. Schmid, H. Kessler, D. C. Lamb, and J. Buchner, “Hsp90 regulates the dynamics of its cochaperone Sti1 and the transfer of Hsp70 between modules,” *Nature Communications*, vol. 6, p. 6655, 2015.
- [36] J. G. White, W. B. Amos, and M. Fordham, “An evaluation of confocal versus conventional imaging of biological structures by fluorescence light microscopy,” *The Journal of Cell Biology*, vol. 105, pp. 41–48, July 1987.
- [37] Y. Wu, X. Wu, R. Lu, J. Zhang, L. Toro, and E. Stefani, “Resonant Scanning with Large Field of View Reduces Photobleaching and Enhances Fluorescence Yield in STED Microscopy,” *Scientific Reports*, vol. 5, p. 14766, Oct. 2015.
- [38] C. Zander, M. Sauer, K. H. Drexhage, D. S. Ko, A. Schulz, J. Wolfrum, L. Brand, C. Eggeling, and C. A. M. Seidel, “Detection and characterization of single molecules in aqueous solution,” *Applied Physics B: Lasers and Optics*, vol. 63, no. 5, p. 517, 1996.
- [39] E. Betzig and R. J. Chichester, “Single molecules observed by near-field scanning optical microscopy,” *Science*, vol. 262, no. 5138, p. 1422, 1993.
- [40] T. Funatsu, Y. Harada, M. Tokunaga, K. Saito, and T. Yanagida, “Imaging of single fluorescent molecules and individual ATP turnovers by single myosin molecules in aqueous solution,” *Nature*, vol. 374, no. 6522, pp. 555–559, 1995.
- [41] H. C. Berg, “How to track bacteria,” *Review of Scientific Instruments*, vol. 42, no. 6, p. 868, 1971.
- [42] J. Gelles, B. J. Schnapp, and M. P. Sheetz, “Tracking kinesin-driven movements with nanometre-scale precision,” *Nature*, vol. 331, no. 6155, p. 450, 1988.

- [43] G. M. Lee, A. Ishihara, and K. A. Jacobson, “Direct observation of brownian motion of lipids in a membrane.,” *Proceedings of the National Academy of Sciences*, vol. 88, pp. 6274–6278, July 1991.
- [44] T. Schmidt, G. J. Schütz, and W. Baumgartner, “Characterization of photophysics and mobility of single molecules in a fluid lipid membrane,” *The Journal of Physical Chemistry*, vol. 99, no. 49, p. 17662, 1995.
- [45] G. J. Schütz, G. Kada, V. P. Pastushenko, and H. Schindler, “Properties of lipid microdomains in a muscle cell membrane visualized by single molecule microscopy,” *The EMBO Journal*, vol. 19, pp. 892–901, Mar. 2000.
- [46] T. Fujiwara, K. Ritchie, H. Murakoshi, K. Jacobson, and A. Kusumi, “Phospholipids undergo hop diffusion in compartmentalized cell membrane.,” *The Journal of cell biology*, vol. 157, pp. 1071–1081, June 2002.
- [47] H. Geerts, M. De Brabander, R. Nuydens, S. Geuens, M. Moeremans, J. De Mey, and P. Hollenbeck, “Nanovid tracking: a new automatic method for the study of mobility in living cells based on colloidal gold and video microscopy.,” *Biophysical Journal*, vol. 52, pp. 775–782, Nov. 1987.
- [48] G. Seisenberger, “Real-Time Single-Molecule Imaging of the Infection Pathway of an Adeno-Associated Virus,” *Science*, vol. 294, no. 5548, p. 1929, 2001.
- [49] U. Kubitscheck, O. Kückmann, T. Kues, and R. Peters, “Imaging and tracking of single GFP molecules in solution,” *Biophysical Journal*, 2000.
- [50] A. Dupont, M. Gorelashvili, V. Schüller, F. Wehnekamp, D. Arcizet, Y. Katayama, D. C. Lamb, and D. Heinrich, “Three-dimensional single-particle tracking in live cells: news from the third dimension,” *New Journal of Physics*, vol. 15, no. 7, p. 075008, 2013.
- [51] H. P. Kao and A. S. Verkman, “Tracking of single fluorescent particles in three dimensions: use of cylindrical optics to encode particle position.,” *Biophysical Journal*, vol. 67, pp. 1291–1300, Sept. 1994.
- [52] S. R. P. Pavani, M. A. Thompson, J. S. Biteen, S. J. Lord, N. Liu, R. J. Twieg, R. Piestun, and W. E. Moerner, “Three-dimensional,

- single-molecule fluorescence imaging beyond the diffraction limit by using a double-helix point spread function.,” *Proceedings of the National Academy of Sciences*, vol. 106, pp. 2995–2999, Feb. 2009.
- [53] M. A. Thompson, M. D. Lew, M. Badieirostami, and W. E. Moerner, “Localizing and tracking single nanoscale emitters in three dimensions with high spatiotemporal resolution using a double-helix point spread function.,” *Nano Letters*, vol. 10, pp. 211–218, Dec. 2009.
- [54] M. Speidel, A. Jonáš, and E. L. Florin, “Three-dimensional tracking of fluorescent nanoparticles with subnanometer precision by use of off-focus imaging,” *Optics Letters*, vol. 28, no. 2, p. 69, 2003.
- [55] E. Toprak, H. Balci, B. H. Blehm, and P. R. Selvin, “Three-dimensional particle tracking via bifocal imaging.,” *Nano Letters*, vol. 7, pp. 2043–2045, June 2007.
- [56] J. Ortega-Arroyo and P. Kukura, “Interferometric scattering microscopy (iSCAT): new frontiers in ultrafast and ultrasensitive optical microscopy.,” *Physical Chemistry Chemical Physics*, vol. 14, pp. 15625–15636, Sept. 2012.
- [57] J. Andrecka, J. O. Arroyo, Y. Takagi, G. de Wit, A. Fineberg, L. MacKinnon, G. Young, J. R. Sellers, and P. Kukura, “Structural dynamics of myosin 5 during processive motion revealed by interferometric scattering microscopy.,” *eLife*, vol. 4, Mar. 2015.
- [58] I. M. Peters, B. G. de Grooth, J. M. Schins, C. G. Figdor, and J. Greve, “Three dimensional single-particle tracking with nanometer resolution,” *Review of Scientific Instruments*, vol. 69, no. 7, p. 2762, 1998.
- [59] G. A. Lessard, P. M. Goodwin, and J. H. Werner, “Three-dimensional tracking of individual quantum dots,” *Applied Physics Letters*, vol. 91, no. 22, p. 224106, 2007.
- [60] E. P. Perillo, Y.-L. Liu, K. Huynh, C. Liu, C.-K. Chou, M.-C. Hung, H.-C. Yeh, and A. K. Dunn, “Deep and high-resolution three-dimensional tracking of single particles using nonlinear and multiplexed illumination.,” *Nature Communications*, vol. 6, p. 7874, July 2015.
- [61] K. Welsher and H. Yang, “Multi-resolution 3D visualization of the early stages of cellular uptake of peptide-coated nanoparticles.,” *Nature Nanotechnology*, vol. 9, pp. 198–203, Feb. 2014.

- [62] K. Kis-Petikova and E. Gratton, “Distance measurement by circular scanning of the excitation beam in the two-photon microscope.,” *Microscopy research and technique*, vol. 63, pp. 34–49, Dec. 2003.
- [63] V. Levi, Q. Ruan, and E. Gratton, “3-D particle tracking in a two-photon microscope: application to the study of molecular dynamics in cells.,” *Biophysical Journal*, vol. 88, pp. 2919–28, Jan. 2005.
- [64] Y. Katayama, O. Burkacky, M. Meyer, C. Bräuchle, E. Gratton, and D. C. Lamb, “Real-Time Nanomicroscopy via Three-Dimensional Single-Particle Tracking,” *ChemPhysChem*, vol. 10, no. 14, p. 2458, 2009.
- [65] P. Annibale, A. Dvornikov, and E. Gratton, “Electrically tunable lens speeds up 3D orbital tracking.,” *Biomedical Optics Express*, vol. 6, pp. 2181–2190, May 2015.
- [66] L. Lanzano, M. A. Digman, P. Fwu, H. Giral, M. Levi, and E. Gratton, “Nanometer-scale imaging by the modulation tracking method.,” *Journal of Biophotonics*, vol. 4, pp. 415–424, Apr. 2011.
- [67] J. B. J. Fourier, *Théorie analytique de la chaleur*.
- [68] J. W. Cooley and J. W. Tukey, “An algorithm for the machine calculation of complex Fourier series,” *Mathematics of Computation*, vol. 19, no. 90, p. 297, 1965.
- [69] S. Kalinin, R. Kühnemuth, H. Vardanyan, and C. A. M. Seidel, “Note: A 4 ns hardware photon correlator based on a general-purpose field-programmable gate array development board implemented in a compact setup for fluorescence correlation spectroscopy,” *Review of Scientific Instruments*, vol. 83, no. 9, p. 096105, 2012.
- [70] R. Orendorff, “Camtiff library.”
- [71] A. Einstein, “Über die von der molekularkinetischen Theorie der Wärme geforderte Bewegung von in ruhenden Flüssigkeiten suspendierten Teilchen [AdP 17, 549 (1905)],” *Annalen der Physik*, vol. 14, no. S1, p. 182, 2005.
- [72] M. J. Saxton and K. Jacobson, “Single-particle tracking: applications to membrane dynamics.,” *Annual Review of Biophysics and Biomolecular Structure*, vol. 26, pp. 373–399, Jan. 1997.

- [73] A. Khintchine, “Korrelationstheorie der stationären stochastischen Prozesse,” *Mathematische Annalen*, vol. 109, no. 1, p. 604, 1934.
- [74] N. Hirokawa, “Kinesin and dynein superfamily proteins and the mechanism of organelle transport.,” *Science*, vol. 279, pp. 519–26, Feb. 1998.
- [75] R. D. Vale, “The Molecular Motor Toolbox for Intracellular Transport,” *Cell*, vol. 112, no. 4, p. 467, 2003.
- [76] M. Aridor and L. A. Hannan, “Traffic Jam: A Compendium of Human Diseases that Affect Intracellular Transport Processes,” *Traffic*, vol. 1, no. 11, p. 836, 2000.
- [77] M. Aridor and L. A. Hannan, “Traffic jams II: an update of diseases of intracellular transport.,” *Traffic*, vol. 3, pp. 781–790, Oct. 2002.
- [78] J. J. Nirschl, M. M. Magiera, J. E. Lazarus, C. Janke, and E. L. Holzbaur, “ α -Tubulin Tyrosination and CLIP-170 Phosphorylation Regulate the Initiation of Dynein-Driven Transport in Neurons,” *Cell Reports*, vol. 14, no. 11, p. 2637, 2016.
- [79] A. L. Zajac, Y. E. Goldman, E. L. Holzbaur, and E. M. Ostap, “Local Cytoskeletal and Organelle Interactions Impact Molecular-Motor-Driven Early Endosomal Trafficking,” *Current Biology*, vol. 23, no. 13, p. 1173, 2013.
- [80] K. Toropova, S. Zou, A. J. Roberts, W. B. Redwine, B. S. Goodman, S. L. Reck-Peterson, and A. E. Leschziner, “Lis1 regulates dynein by sterically blocking its mechanochemical cycle,” *eLife*, vol. 3, 2014.
- [81] M.-m. Fu and E. L. F. Holzbaur, “MAPK8IP1/JIP1 regulates the trafficking of autophagosomes in neurons,” *Autophagy*, vol. 10, no. 11, p. 2079, 2014.
- [82] M.-m. Fu, J. J. Nirschl, and E. L. F. Holzbaur, “LC3 binding to the scaffolding protein JIP1 regulates processive dynein-driven transport of autophagosomes.,” *Developmental Cell*, vol. 29, pp. 577–590, June 2014.
- [83] A. Rai, D. Pathak, S. Thakur, S. Singh, A. K. Dubey, and R. Mallik, “Dynein Clusters into Lipid Microdomains on Phagosomes to Drive Rapid Transport toward Lysosomes,” *Cell*, vol. 164, no. 4, p. 722, 2016.

- [84] Š. Bálint, I. V. Vilanova, Á. S. Álvarez, and M. Lakadamyali, “Correlative live-cell and superresolution microscopy reveals cargo transport dynamics at microtubule intersections.,” *Proceedings of the National Academy of Sciences*, vol. 110, pp. 3375–80, Feb. 2013.
- [85] J. Tam, G. A. Cordier, Š. Bálint, Á. S. Álvarez, J. S. Borbely, and M. Lakadamyali, “A Microfluidic Platform for Correlative Live-Cell and Super-Resolution Microscopy,” *PLoS ONE*, vol. 9, no. 12, p. e115512, 2014.
- [86] J. Tam, G. A. Cordier, J. S. Borbely, Á. S. Álvarez, and M. Lakadamyali, “Cross-Talk-Free Multi-Color STORM Imaging Using a Single Fluorophore,” *PLoS ONE*, vol. 9, no. 7, p. e101772, 2014.
- [87] C. P. Brangwynne, F. C. MacKintosh, and D. A. Weitz, “Force fluctuations and polymerization dynamics of intracellular microtubules,” *Proceedings of the National Academy of Sciences*, vol. 104, no. 41, p. 16128, 2007.
- [88] J. L. Ross, K. Wallace, H. Shuman, Y. E. Goldman, and E. L. Holzbaur, “Processive bidirectional motion of dynein–dynactin complexes in vitro,” *Nature Cell Biology*, vol. 8, no. 6, p. 562, 2006.
- [89] R. Mallik, D. Petrov, S. A. Lex, S. J. King, and S. P. Gross, “Building Complexity: An In Vitro Study of Cytoplasmic Dynein with In Vivo Implications,” *Current Biology*, vol. 15, no. 23, p. 2075, 2005.
- [90] R. Schneider, T. Korten, W. J. Walter, and S. Diez, “Kinesin-1 Motors Can Circumvent Permanent Roadblocks by Side-Shifting to Neighboring Protofilaments,” *Biophysical Journal*, vol. 108, no. 9, p. 2249, 2015.
- [91] M. Brunnbauer, R. Dombi, T.-H. Ho, M. Schliwa, M. Rief, and Z. Ökten, “Torque Generation of Kinesin Motors Is Governed by the Stability of the Neck Domain,” *Molecular Cell*, vol. 46, no. 2, p. 147, 2012.
- [92] P. van Bergeijk, M. Adrian, C. C. Hoogenraad, and L. C. Kapitein, “Optogenetic control of organelle transport and positioning.,” *Nature*, vol. 518, pp. 111–114, Jan. 2015.
- [93] A. L. Misko, Y. Sasaki, E. Tuck, J. Milbrandt, and R. H. Baloh, “Mito-fusin2 mutations disrupt axonal mitochondrial positioning and promote axon degeneration.,” *Journal of Neuroscience*, vol. 32, pp. 4145–4155, Mar. 2012.

- [94] Z.-H. Sheng and Q. Cai, “Mitochondrial transport in neurons: impact on synaptic homeostasis and neurodegeneration.,” *Nature Reviews Neuroscience*, vol. 13, pp. 77–93, Jan. 2012.
- [95] P. J. Hollenbeck and W. M. Saxton, “The axonal transport of mitochondria,” *Journal of cell science*, 2005.
- [96] W. M. Saxton and P. J. Hollenbeck, “The axonal transport of mitochondria.,” *Journal of Cell Science*, vol. 125, pp. 2095–2104, May 2012.
- [97] D. Pathak, K. J. Sepp, and P. J. Hollenbeck, “Evidence that myosin activity opposes microtubule-based axonal transport of mitochondria.,” *Journal of Neuroscience*, vol. 30, pp. 8984–8992, July 2010.
- [98] N. Hirokawa, S. Niwa, and Y. Tanaka, “Molecular motors in neurons: transport mechanisms and roles in brain function, development, and disease.,” *Neuron*, vol. 68, pp. 610–638, Nov. 2010.
- [99] N. Hirokawa, Y. Noda, Y. Tanaka, and S. Niwa, “Kinesin superfamily motor proteins and intracellular transport.,” *Nature Reviews Molecular Cell Biology*, vol. 10, pp. 682–96, Sept. 2009.
- [100] T. L. Schwarz, “Mitochondrial Trafficking in Neurons,” *Cold Spring Harbor Perspectives in Biology*, vol. 5, no. 6, p. a011304, 2013.
- [101] G. Plucińska, D. Paquet, A. Hruscha, L. Godinho, C. Haass, B. Schmid, and T. Misgeld, “In vivo imaging of disease-related mitochondrial dynamics in a vertebrate model system.,” *Journal of Neuroscience*, vol. 32, pp. 16203–12, Nov. 2012.
- [102] D. Paquet, R. Bhat, A. Sydow, E.-M. Mandelkow, S. Berg, S. Hellberg, J. Fälting, M. Distel, R. W. Köster, B. Schmid, and C. Haass, “A zebrafish model of tauopathy allows in vivo imaging of neuronal cell death and drug evaluation.,” *Journal of Clinical Investigation*, vol. 119, pp. 1382–1395, Apr. 2009.
- [103] L. Haddick, “Analysis of mitochondrial dynamics in sensory neurons of zebrafish embryos with 3d orbital tracking.”
- [104] S. Isogai, M. Horiguchi, and B. M. Weinstein, “The vascular anatomy of the developing zebrafish: an atlas of embryonic and early larval development.,” *Developmental Biology*, vol. 230, pp. 278–301, Feb. 2001.

- [105] K. Obashi and S. Okabe, “Regulation of mitochondrial dynamics and distribution by synapse position and neuronal activity in the axon.,” *European Journal of Neuroscience*, vol. 38, pp. 2350–2363, June 2013.
- [106] A. F. MacAskill and J. T. Kittler, “Control of mitochondrial transport and localization in neurons.,” *Trends in Cell Biology*, vol. 20, pp. 102–12, Dec. 2009.
- [107] G. Pekkurnaz, J. C. Trinidad, X. Wang, D. Kong, and T. L. Schwarz, “Glucose regulates mitochondrial motility via Milton modification by O-GlcNAc transferase.,” *Cell*, vol. 158, pp. 54–68, July 2014.
- [108] R. Mallik, B. C. Carter, S. A. Lex, S. J. King, and S. P. Gross, “Cytoplasmic dynein functions as a gear in response to load.,” *Nature*, vol. 427, pp. 649–652, Feb. 2004.
- [109] M. O. Breckwoldt, F. M. J. Pfister, P. M. Bradley, P. Marinković, P. R. Williams, M. S. Brill, B. Plomer, A. Schmalz, D. K. S. Clair, R. Naumann, O. Griesbeck, M. Schwarzländer, L. Godinho, F. M. Bareyre, T. P. Dick, M. Kerschensteiner, and T. Misgeld, “Multiparametric optical analysis of mitochondrial redox signals during neuronal physiology and pathology in vivo,” *Nature Medicine*, vol. 20, no. 5, p. 555, 2014.
- [110] B. R. Rost, F. Schneider, M. K. Grauel, C. Wozny, C. G. Bentz, A. Blessing, T. Rosenmund, T. J. Jentsch, D. Schmitz, P. Hegemann, and C. Rosenmund, “Optogenetic acidification of synaptic vesicles and lysosomes.,” *Nature Neuroscience*, vol. 18, pp. 1845–1852, Nov. 2015.
- [111] G. Ashrafi, J. S. Schlehe, M. J. LaVoie, and T. L. Schwarz, “Mitophagy of damaged mitochondria occurs locally in distal neuronal axons and requires PINK1 and Parkin.,” *The Journal of Cell Biology*, vol. 206, pp. 655–670, Aug. 2014.
- [112] M. Borowiak, W. Nahaboo, M. Reynders, K. Nekolla, P. Jalinot, J. Hasserodt, M. Rehberg, M. Delattre, S. Zahler, A. Vollmar, D. Trauner, and O. Thorn-Seshold, “Photoswitchable Inhibitors of Microtubule Dynamics Optically Control Mitosis and Cell Death.,” *Cell*, vol. 162, pp. 403–411, July 2015.
- [113] P. Nipkow, “Elektrisches teleskop.”
- [114] M. D. Egger and M. Petran, “New Reflected-Light Microscope for Viewing Unstained Brain and Ganglion Cells,” *Science*, vol. 157, no. 3786, p. 305, 1967.

- [115] T. Tanaami and K. Mikuriya, “Nipkow disk for confocal optical scanner,” May 5 1993. EP Patent App. EP19,920,114,750.
- [116] A. Ichihara, T. Tanaami, K. Isozaki, and Y. Sugiyama, *High-speed confocal fluorescence microscopy using a Nipkow scanner with microlenses for 3-D imaging of single fluorescent molecule in real time*, vol. 4. 1996.
- [117] O. M. Subach, I. S. Gundorov, M. Yoshimura, F. V. Subach, J. Zhang, D. Grünwald, E. A. Souslova, D. M. Chudakov, and V. V. Verkhusha, “Conversion of red fluorescent protein into a bright blue probe.,” *Chemistry & biology*, vol. 15, pp. 1116–1124, Oct. 2008.
- [118] J. Goedhart, L. van Weeren, M. A. Hink, N. O. E. Vischer, K. Jalink, and T. W. J. Gadella, “Bright cyan fluorescent protein variants identified by fluorescence lifetime screening,” *Nature Methods*, vol. 7, no. 2, p. 137, 2010.
- [119] N. C. Shaner, R. E. Campbell, P. A. Steinbach, B. N. G. Giepmans, A. E. Palmer, and R. Y. Tsien, “Improved monomeric red, orange and yellow fluorescent proteins derived from *Discosoma* sp. red fluorescent protein,” *Nature Biotechnology*, vol. 22, no. 12, p. 1567, 2004.
- [120] O. M. Subach, G. H. Patterson, L.-M. Ting, Y. Wang, J. S. Condeelis, and V. V. Verkhusha, “A photoswitchable orange-to-far-red fluorescent protein, PSmOrange,” *Nature Methods*, vol. 8, no. 9, p. 771, 2011.
- [121] J. Q. Ren, W. R. McCarthy, H. Zhang, A. R. Adolph, and L. Li, “Behavioral visual responses of wild-type and hypopigmented zebrafish.,” *Vision research*, vol. 42, pp. 293–299, Jan. 2002.
- [122] N. B. Fredj, S. Hammond, H. Otsuna, C.-B. Chien, J. Burrone, and M. P. Meyer, “Synaptic activity and activity-dependent competition regulates axon arbor maturation, growth arrest, and territory in the retinotectal projection.,” *Journal of Neuroscience*, vol. 30, pp. 10939–10951, Aug. 2010.
- [123] M. C. Mullins, M. Hammerschmidt, P. Haffter, and C. Nüsslein-Volhard, “Large-scale mutagenesis in the zebrafish: in search of genes controlling development in a vertebrate,” *Current Biology*, vol. 4, no. 3, p. 189, 1994.
- [124] C. B. Kimmel, W. W. Ballard, S. R. Kimmel, B. Ullmann, and T. F. Schilling, “Stages of embryonic development of the zebrafish,” *Developmental Dynamics*, vol. 203, no. 3, p. 253, 1995.

[125] L. Godinho, “Live Imaging of Zebrafish Development,” *Cold Spring Harbor Protocols*, vol. 2011, no. 7, p. pdb.top119, 2011.

List Of Abbreviations

- 3D Three dimensional
- STORM Stochastic optical reconstruction microscopy
- STED Stimulated emission depletion
- ALS Amyotrophic lateral sclerosis
- EMCCD electron multiplying charge-coupled device

- CCD Charge-coupled device
- CMOS Complementary metal-oxide-semiconductor
- FPGA Field programmable gate array

- DMSO Dimethyl sulfoxide
- GFP Green fluorescent protein
- RFP Red fluorescent protein
- PMT Photo multiplier tube
- APD Avalanche photo diode
- FCS Fluorescence correlation spectroscopy
- FRET Fluorescence resonance energy transfer

- SPT Single-particle tracking
- iScat interferometric scattering microscopy
- TSUNAMI interferometric scattering microscopy
- TCSPC Time correlated single photon counting
- AOBD Acousto optical beam deflector

- FIFO First-in first out
- DMA Direct memory access
- CPU Central processing unit
- TTL Transistor-transistor logic
- ASCII American standard code for information interchange

- MSD Mean squared displacement
- FFT Fast Fourier transformation
- iFFT Inverse fast Fourier transformation
- FWHM Full width at half maximum

- PCU Precision control unit
- ALC Andor laser combiner

Acknowledgments

First of all i would like to thank my supervisor Prof. Don C. Lamb for the chance to do my PhD in his group. Thank you for answering all my intelligent and not so intelligent questions. Thank you for not giving me trouble when pieces of equipment stopped working without me even touching them. I promise that every broken piece of equipment over the years has giving me knowledge about how not to do things (a very important lesson)! Thank you for providing huge amounts of research money, which allowed me to buy very expensive equipment that made my life easier and allowed me to travel to awesome conferences. Thank you for teaching us American culture (not so much to teach there, except Football - Go Packers!) And finally thank you for being my supervisor. It was a pleasure working for (or as you would say - with) you.

The second person to thank is Prof. Thomas Misgeld. Working with you on the zebrafish project was always a pleasure. Thank you for all the scientific discussions from the biological point of view and also for the very prolonged discussions about paper figures! Thank you also for being the second referee of my thesis.

The next person on this list is Prof. Christoph Bräuchle, whom i want to thank for his support regarding science, lab space, money and for being a referee in my PhD committee.

I want to thank Mrs. Steger and Dr. Moritz Ehrl for making the life of a PhD student endurable by helping with all sorts of the German bureaucracy, like purchasing items or most important holiday forms. A special thanks to Moritz for his never ending supply of amusing stories and sarcastic remarks!

I also want to thank my cooperation partners in the fish field: Gabi, Rachel and Doug, who provided a never ending stream of zebrafish embryos for

research. Thank you all for the nice work atmosphere and the several occasions where we became friends - I will miss working with you! Thanks to my cooperation partners in Barcelona, Prof. Melike Lakadamyli and Ione Verdeni-Vilanova. It was a pleasure working with you and the conference in Castelldefels was awesome!

I want to thank all my colleagues who worked with me over all the years. First of all i have to mention Niko. You took me into the group as an intern and told me how to survive a PhD. Although you left roughly two years after my start, we will be again colleagues at National Instruments and i am looking forward to that! The second person is Aurélie (see, i made this accent thingi), who was my supervisor during my master thesis. You introduced me to the orbital tracking setup and answered all of my stupid question in the beginning. Thanks aswell for inviting me to Grenoble to have a look at your new Group! I want to thank the coolest office - Giulia and Sushi - for the awesome time we had. I know i tortured you with my passion for fresh air and open windows even in winter, but we all could laugh about that most of the times. And in the end we just didn't care (official office hymn, Icona Pop - I Love It!). I also want to thank Giulia for the postdoc support you gave me during the initial phase of the zebrafish project. I want to thank Lena for being the most helpful, trustworthy and reliable person i know. I want to thank the STORM man Jens for being the person one can talk to. I want to thank Bässem for providing me with the latest games to play and several evenings of preparing against the zombie apocalypse. Thank you waldi for knowing things from the lab and the outer world no one would ever think of (Luftgurken?!). Maria, i want to thank you for the office time we shared and the insights into Iranian culture. And remember, that thing on your screen is still an elephant! Thank you Ganesh for the insights into Indian culture and the awesome spices you brought from home! One day you will be completely germanized and you will show up at 8 am sharp every day! I want to thank KirAnders for awesome evenings watching Game of Thrones and eating good food! I want to thank Nader for his constant high spirits (how are you doing that??) and for taking over the IT stuff. I want to thank Chen for introducing us to fancy food and stories from Singapore (bamboo sticks in the army really??). I want to thank Viola for introducing me into the cell culture world and for always providing huge amounts of salad for each barbecue! I want to thank Evelyn for the sarcasm we could share in the last year and for playing lasertag with us (Hihihi - i shot you). I have to thank the last woman standing in the AK Bräuchle - Ellen. Thanks for all the cakes, cookies, brownies and other sugary treats you brought along! I want to thank Adriano for PostDoc advise, excellent conversations and

the awesome beef you always brought along for barbecues :D... Also a big thanks to all the other unmentioned people that helped along the way! It was a pleasure.

I want to thank my interns Leo, Lisa, Annette, Simon and Frank for helping me with my work. I have to point out that Simon and Frank both will end up in the Fablab (2/5 is quite a good ratio or?). Frank, you have to take care of my baby from now on. Treat it well!

I have to thank my friends, especially Christian, Freddi and Manu for spending way too many nights and way too much money in our favorite club and several other bars in Munich and Leipzig. Getting away from university once in a while really helped along the way! Thank you Kai, for the time since school and for the weekly gaming sessions!

In the end i want to thank my family. First, i want to thank my mother Andrea. You forced me to write an application for the LMU and i could not be more grateful! Without you, i would never have moved to munich! I want to thank my father Dierk for always supporting me in the way you did! I want to thank my grand parents Hildegard and Helmut for always having an open ear for problems and advice how to solve them! I want to thank Burghardt for your needle sharp comments about the world itself that always make me laugh. I want to thank my brother Tobias for being more reasonable and my small brother Jonas for being more crazy. And last, i want to thank my little Sister Fiona, who (without knowing) always cheers me up.

